Czech Technical University in Prague

Faculty of Biomedical Engineering

Doctoral Thesis

March 2023

Tomas Pokorny

Czech Technical University in Prague
Faculty of Biomedical Engineering
Department of Biomedical Technology

MICROWAVE STROKE DETECTION AND CLASSIFICATION USING MACHINE LEARNING ALGORITHMS AND REALISTIC MODELS OF THE HUMAN HEAD

Doctoral Thesis

Tomáš Pokorný

Kladno, March 2023

Ph.D. Programme: Biomedical and Clinical Technology
Branch of study: Biomedical and Clinical Technology

Supervisor: prof. Dr.-Ing. Jan Vrba, M.Sc.
Supervisor-Specialist: doc. Ing. David Vrba, Ph.D.

DECLARATION

I hereby declare that I have completed this thesis with the topic "Microwave stroke detection and classification using machine learning algorithms and realistic models of the human head" independently, and that I have attached an exhaustive list of citations of the employed sources.

I do not have a compelling reason against the use of the thesis within the meaning of Section 60 of the Act No. 121/2000 Sb., on copyright, rights related to copyright and amending some laws (Copyright Act).

In Kladno …...…..……...……...

Ing. Tomas Pokorny

ACKNOWLEDGEMENTS

I would like to thank the entire Bio-Electromagnetism team for their support, advice, and help. Special thanks to my supervisor Prof. Dr.-Ing Jan Vrba, M.Sc. Thanks also to my family and the people on the faculty for the support they have shown me during this study and research.

The thesis was supported by grants SGS19/204/OHK4/3T/17; SGS17/204/OHK4/3T/17 and by instrumentation from OPVVV CZ.02.1.01/0.0/0.0/16_017/0002244.

ABSTRACT

Title of the Thesis: **Microwave stroke detection and classification using machine learning algorithms and realistic models of the human head.**

The goal of this work is to systematically test the capabilities of machine learning algorithms in microwave detection and classification using data with natural variability. This requires large datasets to train and test the algorithms, obtained in this study with 2D and 3D numerical simulations and measurements on phantoms. The corresponding parametrized numerical models contain 10 different anatomically and dielectrically realistic human head models with a stroke model of adjustable size, position, and type. Experimental measurements were performed on an anatomically and dielectrically realistic 3D human head phantom supplemented with a computer-controlled positioning system to set the position of the stroke model within the head phantom.

The support vector algorithm (SVM) proved to be the most effective for the given application. Algorithm performance was evaluated using a confusion matrix (classification accuracy, sensitivity, and specificity) and Cohen's kappa value. Cross-validation was also evaluated during training. Algorithm performance was increased by hyperparameter optimization and dimensionality reduction using PCA.

The results show the ability of the SVM algorithm to detect the presence of stroke and classify it into either ischemic or hemorrhagic subtype. Single-frequency data of 1 GHz is sufficient, datasets with both transmission and reflection coefficients expressed in real and imaginary parts show higher classification accuracy than datasets with only transmission coefficients or with coefficients expressed in modulus and phase. Datasets from subjects with smaller strokes are best suited for training accurate SVM predictors, and the algorithms show high generalizability. Nevertheless, the study suggests that accurate detection and classification of strokes for natural data variability remains a challenge. Misclassifications can endanger patients' lives when classifying into three classes, but the algorithm is highly accurate in classifying ischemic strokes and safely recommends thrombotic therapy initiation in around 70 % of affected patients. Further research is needed to improve the sensitivity of the algorithm and increase its clinical usefulness.

Keywords

Machine learning, SVM, brain stroke, microwave devices, phantoms, numerical model

ABSTRAKT

Název práce: **Mikrovlnná detekce a klasifikace cévních mozkových příhod pomocí algoritmů strojového učení a realistických modelů lidské hlavy.**

Cílem této práce je systematicky testovat možnosti algoritmů strojového učení v mikrovlnné detekci a klasifikaci CMP s důrazem na realistickou variabilitou testovacích dat. Za tímto účelem je nezbytné vytvořit velké soubory dat pro trénování a testování algoritmů. V této práci k tomu byly využity 2D a 3D numerické simulace a měření na fantomech. Odpovídající parametrizované numerické modely obsahují 10 různých anatomicky a dielektricky realistických modelů lidské hlavy s modelem CMP o nastavitelné velikosti, pozici a typu. Experimentální měření byla provedena na anatomicky a dielektricky věrném 3D fantomu lidské hlavy doplněném o počítačem řízený systém polohování modelu CMP.

Z algoritmů strojového učení se pro tuto aplikaci nejvíce osvědčil algoritmus podpůrného vektoru (SVM). Výkonnost algoritmu byla hodnocena pomocí konfuzní matice (přesnost klasifikace, senzitivita a specificita) a hodnoty Cohenovy kappy. Při trénování byla rovněž vyhodnocena křížová validace. Výkon algoritmu byl zvýšen optimalizací hyperparametrů a redukcí dimenzionality pomocí PCA.

Výsledky ukazují schopnost algoritmu SVM detekovat přítomnost CMP a klasifikovat ji buď na ischemický, nebo hemoragický podtyp. Jednofrekvenční data o frekvenci 1 GHz jsou dostatečná, datasety s přenosovými i odrazovými koeficienty vyjádřenými v reálné a imaginární části vykazují vyšší přesnost klasifikace než datasety s pouze přenosovými koeficienty nebo s koeficienty vyjádřenými v modulu a fázi. Datové sady od subjektů s menšími CMP jsou nejvhodnější pro trénování přesných prediktorů SVM a algoritmy vykazují vysokou schopnost generalizace. Studie nicméně naznačuje, že přesná detekce a klasifikace CMP pro přirozenou variabilitu dat zůstává výzvou. Při klasifikaci do tří tříd se objevovaly chybné klasifikace, které mohou ohrozit život pacientů, ale algoritmus byl přesný při klasifikaci ischemických CMP a bezpečně doporučuje zahájení trombotické léčby u přibližně 70 % postižených pacientů. Ke zlepšení citlivosti algoritmu a zvýšení jeho klinické užitečnosti je zapotřebí dalšího výzkumu.

KLÍČOVÁ SLOVA

Strojové učení, SVM, cévní mozková příhoda, mikrovlnné systémy, fantomy, numerický model.

CONTENT

List of symbols and abbreviations

WHO	World Health Organization
S-matrix	Scattering matrix
CSF	Cerebrospinal fluid
S-parameters	Scattering parameters
SVM	Support Vector Machine
CT	Computed tomography
EIT	Electrical impedance tomography
MRI	Magnetic resonance imaging
hStroke	Hemorrhagic stroke
iStroke	Ischemic stroke
MW	Microwave
EM	Electromagnetic
TSVD	Truncated Singular Value Decomposition
SVD	Singular Value Decomposition
ReIm	Real and imaginary part data format
MoPh	Module and phase format
PC	Principal component
DNNs	Deep Neural Networks.
FFT	Fast Fourier Transformation
TL	Transmission-line
Other class	Classification class including hStroke and noStroke class
TP	True Positive
FN	False Negative
FP	False Positive
TN	True Negative
CL-accuracy	Classification accuracy
Kappa	Cohen's kappa (κ)
CV-error	Cross-validation error
LR	Logistic Regression
DA	Discriminant Analysis
kNN	k-Nearest Neighbors
NB	Naive Bayes Classifier
CTr	Classification Tree
TrRe	Transmission and reflection coefficients of scattering matrix
Tr	Transmission coefficients (Tr) of scattering matrix

1. Introduction

Strokes affect 15 million people worldwide each year. Diagnosis of the type of stroke is crucial to initiating treatment. In approximately 85% of cases, thrombotic therapy could already be started in ambulances. Despite the major technological advances of recent decades, there is no prehospital diagnosis system. Without a diagnosis, it is impossible to start treatment without risking the patient's life. Patients must be transported to the hospital for diagnostics, which can delay the start of treatment by tens of minutes. Late start of treatment reduces the chance of recovery and increases the consequences of the disease. Microwave technologies may be a suitable basis for the development of a portable, reliable, rapid, and affordable prehospital stroke diagnosis system. [1]–[5]

This study focuses on the detection and classification of different types of strokes using recent, widely-used machine learning algorithms. The selection of suitable training data is a crucial aspect of machine learning, and requires careful consideration of the data collection, format, and dimensionality reduction procedures and data variability. The testing of microwave systems in controlled laboratory environments, the development of appropriate data processing protocols, and the evaluation of suitable algorithms are critical phases in the implementation of a reliable system for clinical use. [6], [7]

1.1 Stroke disease

A stroke is a life-threatening condition caused by a disorder of the cerebral blood circulation. There are two main types of strokes (see Figure 1), hemorrhagic (hStroke) and ischemic (iStroke). Although both share a very similar symptom, the treatment is completely different, so it is important to diagnose the type of stroke quickly and accurately. In untreated strokes, millions of brain cells die every minute, which can result in loss of memory, movement, or speech, and can lead to death [8]. According to the World Health Organization (WHO)[2], 15 million people worldwide suffer a stroke each year, of which 5.8 million dies, and almost the same number have permanent consequences. Stroke accounts for almost 10% of the total mortality of the population. Stroke is also the most common cause of death among young people and people of working age. In developed countries, the incidence of stroke is decreasing, mainly due to the treatment of blood pressure and the decreasing popularity of smoking. However, the overall stroke rate remains high due to the aging population. Stroke is one of the most

dangerous diseases and one of the leading causes of disability in adults. It also has a great socio-economic impact on society as a whole. [2], [9]

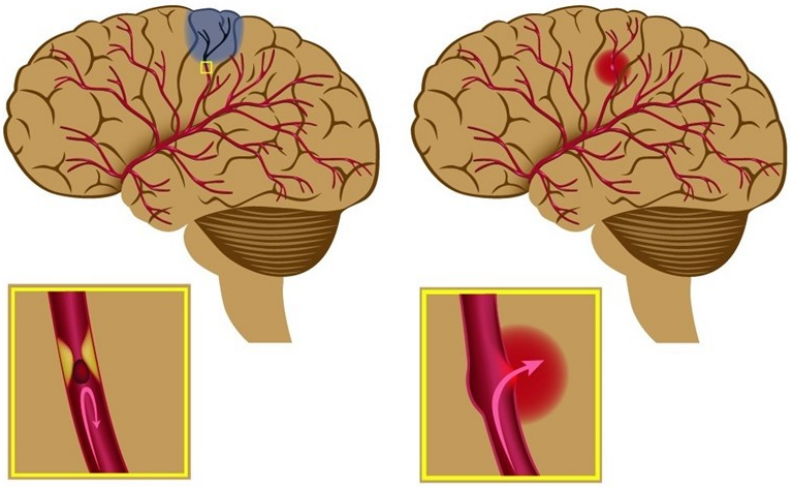

Figure 1. Ischemic stroke (left) and hemorrhagic stroke (right). Taken from [10].

A hemorrhagic stroke is caused by rupture of a cerebral vessel and bleeding into the brain. Bleeding can be intracerebral (occurring in 17% of cases), or intraventricular or subarachnoid (occurring in 3% of cases). Bleeding is stopped with endovascular surgery or neurosurgery. Hemorrhagic stroke is characterized by higher mortality than ischemic stroke. [9], [11]–[13]

In an **ischemic stroke**, a cerebral vessel closes with a blood clot, causing a reduction in blood flow and can result in necrosis of blood-deficient tissues. Approximately 85 % of strokes are ischemic [3], [14]. Approximately two million neurons die every minute, which will never be replaced by new ones [15]. Therefore, a quick diagnostic is essential. Ischemic stroke can be treated with thrombolytic therapy, which dissolves the clot and restores blood circulation, or surgical removal of the clot is possible. According to the American Stroke Association and clinical thrombolysis guidelines, the first 4.5 h after ischemic stroke is “the golden period” for receiving thrombolytic therapy [13], [16]. Currently, only 10% of patients with ischemic stroke have received thrombolytic treatment during "the golden period". A precise diagnosis of an ischemic stroke is essential because if thrombolytic therapy is used during a hemorrhagic stroke, it would dilute blood, increase bleeding into the brain, and endanger the patient's life [4], [17].

1.1.1 Stroke size and localization

Detailed knowledge of strokes is important for the construction of numerical models and phantoms, especially its location, size, and dielectric properties. In real life, stroke volume depends on many factors, such as the blood vessels of interest, the location of the stroke, and the diagnosis time (see, e.g., [15], [18], [19]), and it can acquire volumes from 0.03 to 250.02 cm^3 [19]. Motor and functional outcomes, including death or daily dependence on the help of other people, after stroke are significantly correlated with the location and size of the stroke [19]–[22].

The size and location of the **hemorrhagic stroke** were examined in [20] on 55 hemiplegic patients with magnetic resonance imaging (MRI) one month after the stroke. Five primary locations were identified depending on the dominant anatomic lesions. The size of a brain injury that results in poor motor and functional outcomes was found to vary depending on the injury's location: 75 cm^3 for the cortex, 4 cm^3 the corona radiata, 0.75 cm^3 for the internal capsule, 22 cm^3 for the putamen, and 12 cm^3 for the thalamus. In this study, it was also mentioned that brain images taken in the first 48 hours can seriously underestimate the size of the lesion, while those taken in the first 3 to 7 days can overestimate the size of the lesion. The initial increase in the size of the lesion and subsequent decrease as a result of activation of cytotoxic processes is also confirmed by study [23], in which this effect was investigated in rats.

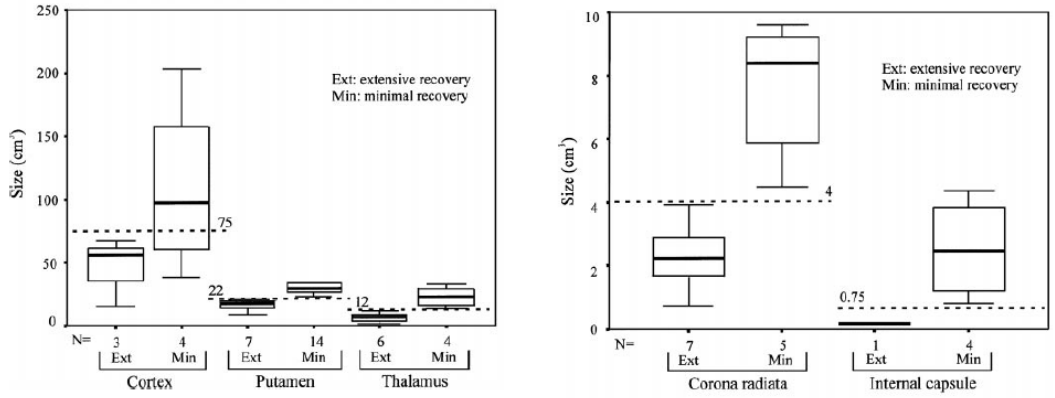

Figure 2. Location of the occurrence of hemorrhagic stroke and the median stroke volume in cm^3. The dashed line marks the boundary for patients with poor motor and functional outcomes. Taken from [20].

The study [24] provides detailed sizes and locations of the **ischemic stroke**. The location of the stroke was examined in 162 patients within 14 days after the onset of the stroke. The brain was divided into 8 parts for the right and left hemispheres. If we do not consider hemispheres, Figure 3 shows the numbers of strokes and their median size with the interquartile range. Although stroke on the left side is better distinguished by clinical signs than on the right side, the incidence of stroke on both hemispheres is approximately the same according to MRI scans [25]. The study confirms a smaller volume of nonhemorrhagic strokes at the time of admission than after a few days [26], which also mentions a reduction in stroke volume after a few months. Study [27] found that patients with diffusion abnormality greater than 72 mL had a poor motor and functional outcome, indicating severe deficits and a high risk of death or dependency, if not treated effectively. This conclusion is supported by studies [28], [29]. In a study [30] they found that the mean ischemic stroke volume in independent patients (not need help from another person) was 35.7 ± 29.7 mL compared to 88.3 ± 71.3 mL in dependent patients (need help from another person) and 166.5 ± 65.9 mL in dead patients. Patients with an **initial infarct volume of less than 80 mL have fewer consequences** than patients with a larger infarct volume [30].

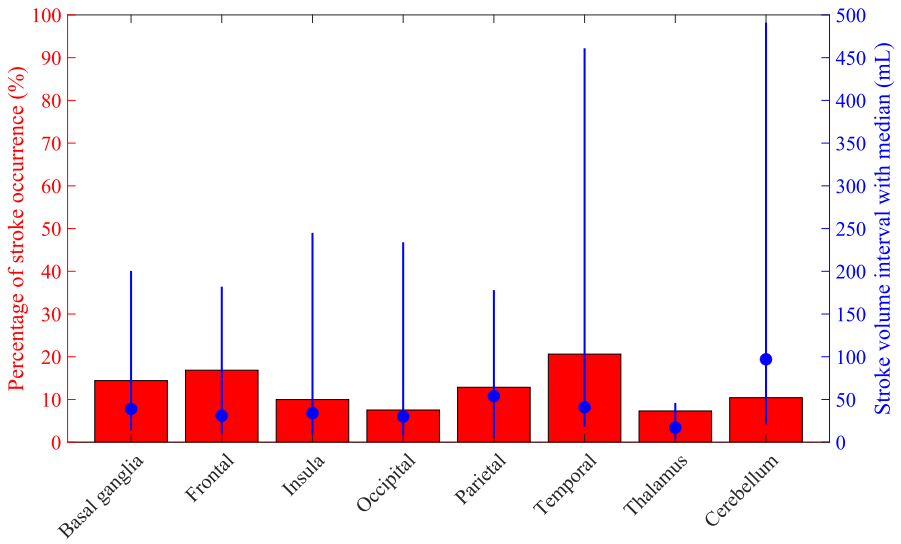

Figure 3. Analysis of the location of ischemic stroke occurrence and the median stroke volume in cm^3. The data taken from [24].

It is envisaged that the microwave system for stroke detection and classification will be used for early diagnosis, where the lesion is small and growing, so it is necessary to consider rather smaller sizes. The stroke has a variety of shapes, but they are mostly spherical or ellipsoidal [31]–[33]. The volumes of spherical strokes are shown in Table 1, where the spherical stroke sizes/volumes that we will consider in the study are in bold.

Table 1. Spherical stroke volumes

Stroke diameter (mm)	Stroke volume (mL)
10	0.52
15	1.77
20	4.19
25	8.18
30	14.13
35	22.44
40	33.49
45	47.69
50	65.72
55	87.07
60	113.04

1.1.2 Stroke dielectric parameters

For the microwave imaging of a stroke, it is essential to know the dielectric properties of the tissues in the human head. Several studies have been performed [34]–[36], and a database of tissue dielectric properties [37] has been created. A fundamental requirement for the feasibility of microwave imaging and stroke classification is a significant contrast in the dielectric properties compared to other brain tissues. [38]–[40]. In the study [41], it was shown that the values of the dielectric properties of blood are approximately 20 % higher than those of grey matter and about 60 % higher than those of white matter. The study [42] examined the dielectric properties of swine brain tissues in an acute ischemic stroke, which proved that an ischemic stroke causes changes in the dielectric properties of brain tissue immediately after its origin. The dielectric properties of tissue at the site of origin are reduced by 10% to 25% of the original value. The study also showed that after the blood supply was restored, the dielectric properties returned to

their initial values. It has been demonstrated in [43] that the brain of pigs has dielectric properties very similar the human brain. The above-mentioned contrast should make it possible to detect and determine the type of stroke at an early stage using the microwave system, or to monitor its development over time. The contrast of the dielectric parameters for head tissue and ischemic and hemorrhagic stroke is shown in Figure 4.

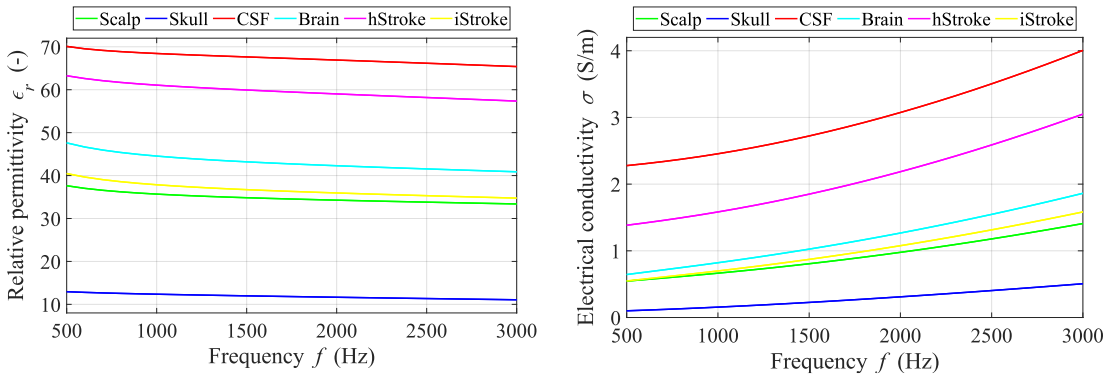

(a) (b)

Figure 4. Comparison of relative permittivity (a) and electrical conductivity (b) for head tissue and ischemic and hemorrhagic stroke. The graphs were determined using the frequency-dependent 4-pole Cole–Cole model with parameters obtained from database[37]. The dielectric properties of the brain were calculated as average values of white matter, gray matter, and cerebellum, and for the scalp, the average values of skin and fat were used. For ischemic strokes, a 15% reduction in the dielectric parameters of the brain was assumed, while the dielectric parameters of hemorrhagic strokes were set to be equivalent blood.

1.2 Stroke diagnostics

Computed tomography (CT) is now the gold standard for stroke diagnostics [44]. The main disadvantage of CT is that it is not well suited for field use. Although mobile CT units have been developed to examine stroke patients [41], it is not the usual equipment of ambulances. Furthermore, CT uses ionizing radiation, which cannot distinguish small affected areas, and the problem may be the diagnosis in the initial stage of stroke when the affected tissue does not appear abnormal. The handheld instrument using near-infrared spectroscopy, the Infrascanner [45], [46] was recently developed. The disadvantage of Infrascanner is the impossibility of detecting stroke deep inside the brain, due to the limited penetration depth of approximately 2.5 cm. Another possible stroke detection is electrical impedance tomography (EIT) [47], [48]. However, the skull has electrically insulating properties that limit current penetration and prevent high-quality deep imaging of the brain without the use of implanted electrodes [49]. The use of

ultrasound for stroke detection is in development [50], [51], and the device does not allow for portability. Magnetic resonance imaging (MRI) is often used for stroke diagnostics. MRI provides a high contrast of soft tissues, does not contain ionizing radiation, and thus allows an accurate determination of the location and type of stroke, even in small areas in the early stages of the disease. However, the diagnosis with an MRI is expensive, unsuitable for patients with claustrophobia or with implanted metal objects, and it is lengthy. Also, an MRI is not appropriate for use in the field, e.g. in ambulances, due to its size.

Microwave technology has great potential for stroke diagnosis, as microwave (MW) systems could be small, portable, and inexpensive and thus suitable for the prehospital diagnosis of a stroke. The MW system uses also low-power (< 20 mW) signals signals that are capable to penetrate the skull and brain [1]. When signal transmission between antennas on opposite sides of the head is used, strokes deep in the brain can be detected. Thanks to the above mentioned contrast between healthy and stroke-affected brain tissue, non-invasiveness and non-ionizing radiation, such a system will be precise, safe, and easy to use. The disadvantages of MW imaging may be lower resolution, or also susceptibility to electromagnetic interference. It should also be noted that lay public still has a fear of electromagnetic waves, as their effect on human health is not yet entirely clear. [6], [52], [53]

1.3 Microwave systems for stroke detection

At the forefront of microwave imaging system development for stroke detection and classification are various research groups and companies globally. The leading groups include Medfield Diagnostics in Sweden [48], and EMtensor in Austria [55]. Additionally, other groups in Australia [50] and Italy [56] are also contributing to the development of microwave stroke systems. Our research team at the Faculty of Biomedical Engineering, Czech Technical University in Prague is also actively engaged in developing a microwave imaging system for the detection and classification of strokes [57]–[60].

In general, two different approaches for microwave stroke detection can be found in the literature. The first method is based on visualization (image reconstruction) of the distribution of dielectric parameters in the region of interest [61]–[64]. Since the

propagation of microwaves through the human head involves not only attenuation but also phase shift and multiple reflections at the interface of regions with different dielectric properties, image reconstruction is a complex problem requiring a priori information from the imaged area and high computing power. The second method is based on machine learning algorithms (see section 1.4), which quickly detect and classify the type of stroke. This information is enough to start appropriate treatment. On the other hand, the approach based on machine learning algorithms typically requires a large set of training data.

Studies [1], [12], [65] have found that a frequencies close to 1 GHz are the most suitable for a microwave human head imaging. Frequencies around 1 GHz are a compromise between the attenuation of microwave signals and spatial resolution. The attenuation of electromagnetic (EM) waves in biological tissues and the spatial resolution increase with frequency. While we require the highest possible spatial resolution, attenuation reduces the signal-to-noise ratio. Considering typical dielectric properties, thicknesses, and order of the different tissues in the human head, there is a forbidden frequency band in the 1.5 to 4 GHz range in which the transmission coefficient is lower [66].

The research team of Prof. Serguei Semenov, EMTensor, Austria is developing a system based on **microwave tomography that provides structural and functional 3D imaging of the head**. This system can be integrated into ambulances. Only microwave measurements are to take place directly in the ambulance, the measured data are subsequently sent via the Internet for processing on a high-performance computing cluster. In addition to the above system, the company is developing an electromagnetic tomographic system for continuous monitoring of patients in the form of a cap or which will be integrated into a headrest in a car or chair. The first generation of the microwave tomography system [67], [68] was tested in volunteers and images of the real human brain were introduced. The second generation called 'BRIM G2' [69] [70] was tested on phantoms. The imaging antenna array consists of 177 rectangular ceramic filled waveguide antennas mounted on a stainless-steel hemispherical chamber. The antennas are evenly spaced in eight circles at different heights. The operating frequency is 1 GHz. The large number of antennas used in this system ensures that a large amount of information is obtained for imaging purposes. The disadvantages are the high cost and

the accuracy of the system. The authors are confident that microwave tomography can be applied to the real human head and detect and differentiate strokes. The algorithm was adapted to the phantom of the human head and showed worse results for measurements on volunteers. This is despite the fact that the tissues of the human head show a higher dielectric contrast than the phantom used. **A large data set obtained from anatomically and dielectrically realistic models of human heads showing natural variability is required.** The latest version of the EMTensor system called 'BRIM G3' is presented in [71]. The system consists of 192 integrated waveguide-based antennas arranged in six rings with 32 antennas per ring. The system was experimentally verified using a 3D head phantom filled with homogeneous liquid to emulate average brain tissues [72]. Images of two patients (one patient with hemorrhagic stroke and the other with ischemic stroke) were imaged with tomography in [71]. Promising results have been shown, suggesting the ability to detect and differentiate between different lesions. **However, the system is designed for monitoring patients at the bedside rather than for rapid field diagnostics in ambulance vehicles.**

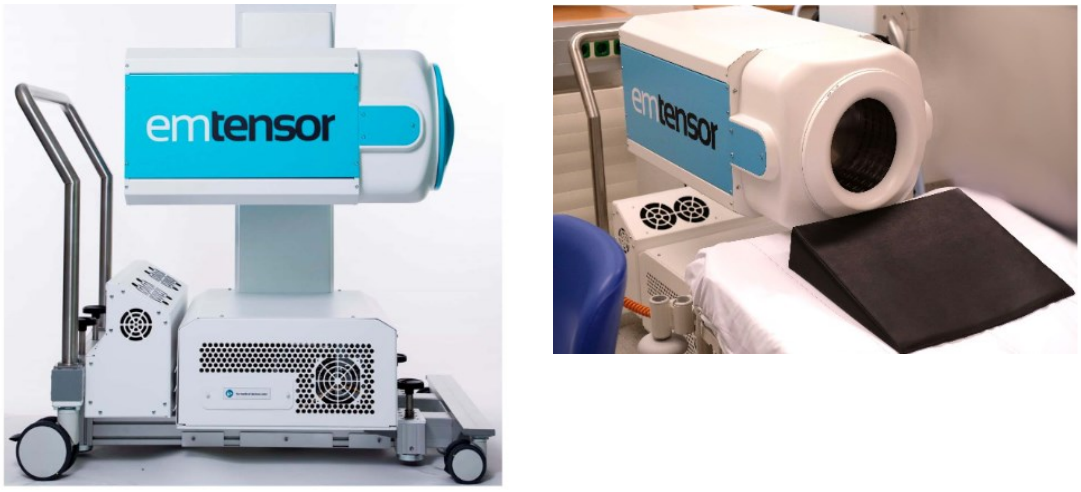

(a) (b)

Figure 5: The third generation EMTensor clinical prototype microwave imaging system (a) and (b) top unit in operational mode behind the patient's bed with the patient's support pillow. Taken from [71], [72]

The research team of prof. Amin Abbosh, The University of Queensland, Australia is developing a system based on the **radar approach and uses reconstruction algorithms to diagnose intracranial hematoma.** The system consisting of an antenna rotating around the head phantom was presented in [53], [73], [74]. Alternatively, fixed antenna systems [75], [76] and finally a 16 antenna array system have been introduced [77]. The system was tested on a 3D printed human head phantom with 3D printed internal molds filled with tissue-equivalent mixtures [78]. This phantom can be used for the experimental validation of microwave systems before their clinical evaluation. Measurements on one phantom do not bring a natural variability of measured data, therefore, a larger number of test objects will be needed. In [79], five different healthy volunteer head images are presented and confirm the imaging similarities between realistic healthy head phantoms and volunteer heads, as well as among different sizes and shapes of the heads. Yet, still, the interior portion of the head cannot be prominently layered, and thus improvements in hardware and the imaging algorithm are required.

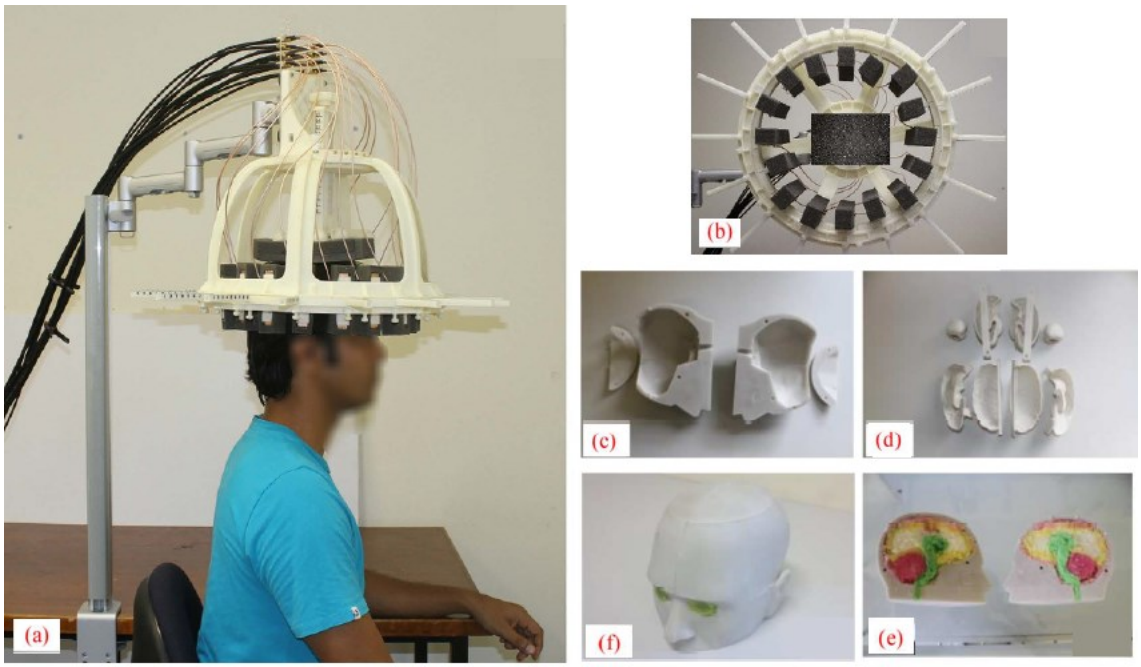

Figure 6: Microwave radar-based system (a) developed by a team of prof. Abbosh from Australia; (b) 3D printed head imaging crown depicting the orientations of the sensing antenna holders; (c),(d) various 3D printed parts; (e) the halves of the fabricated phantom; (f) the whole head phantom. Taken from [77].

The company EMVision Medical Devices, Sydney, Australia, introduced the first generation of a brain imaging system [80] probably based on previous developed the flexible electromagnetic cap described in [81], although this is not explicitly stated. The prototype of this mobile device consists of a helmet with an antenna array, which is shielded by a membrane that can be filled with matching medium. Data acquisition takes approximately 2 seconds for the frequency spectrum ranging from 0.5 to 2 GHz. Image reconstruction using several algorithms takes a few seconds to a few minutes. These algorithms use diverse processing approaches, including radar-based frequency domain [76] and time domain [82] signal analysis, signal asymmetry, tomography [62], and direct mapping. Study [83] used machine learning algorithm to recognize ischemic and hemorrhagic stroke from the image of the distribution of dielectric parameters obtained from Born iterative method. Currently, the brain imaging system is undergoing clinical testing at researches hospital and is not yet licensed for clinical use.

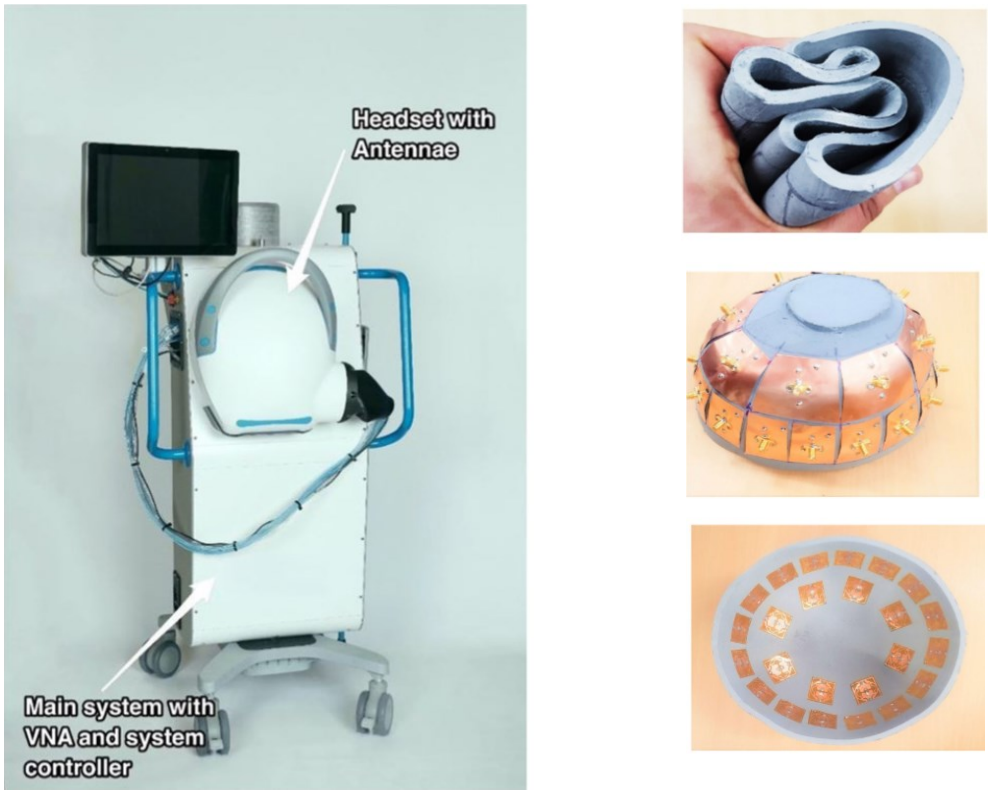

(a) (b)

Figure 7. (a) Clinical prototype electromagnetic head scanner, taken from [80]. (b) Flexible electromagnetic cap, taken from [81].

The research team of prof. Pastorino from University of Genoa, Italy presented a microwave system with 16 vertically polarized antennas placed around the head [84]. Bags filled with coupling medium are placed between the head and the antennas to reduce reflections from the air and skin and to increase the penetration of waves into the deep layers of the head. The operating frequency band is between 500 MHz and 2.5 GHz. The system was tested on a cylindrical liquid phantom and provided the first results of differential imaging of dielectric parameter changes in 2D. However, testing on more complex phantoms is needed. In the study [85], the authors proposed the use of machine learning algorithms to detect the presence and classify the stroke type with differential dielectric parameter imaging for displaying the location and size of the stroke. However, no results for the developed system were presented.

The research team of prof. Mikael Perrson, Chalmers University and Medfield Diagnostics, Sweden is developing an MW device which, however, is not meant for stroke imaging, but for its detection and classification (ischemic or hemorrhagic). Stroke classification is performed by measuring the whole scattering matrix (S-matrix) and processing the data using a **training-based machine learning algorithm,** using known data. Three generations of this microwave system have already been developed [86], [87]. The latest generation is called Strokefinder MD100 [6], [88]. This system consists of a system of 8 antennas operating at frequencies 0.1 – 1.95 GHz, a microwave unit, and a signal processing computer. This system fits completely in the case, without the need to send data over the Internet. The adaptation of the helmet to the shape of the patient's head is solved by bags with fluid in front of the antenna elements. The fluid fills the space between the antennas and the patient's head and provides an improvement in impedance matching. It is still an experimental device that has been tested in patients not under life-threatening conditions, i.e. even a few hours after the onset of a stroke. The results show that patients with hemorrhagic stroke can be accurately identified with 90% detection sensitivity, but the classification results of ischemic patients are not satisfactory [1]. This slows further development because the algorithm needs the most up-to-date patient data possible in order to achieve more accurate results. **Development could be accelerated by testing the system on a large data set.** Strokefinder was able to reliably distinguish whether the patient had a hemorrhagic stroke on several tests. However, it mistakenly

classified ischemic stroke several times into the category of a hemorrhagic stroke**. Further development and testing of algorithms is needed**.[54], [89]

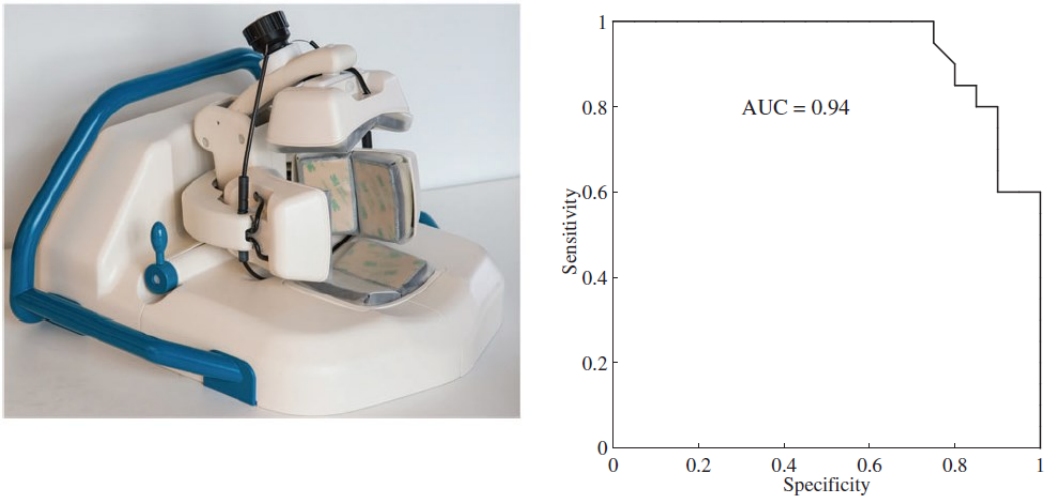

(a) (b)

Figure 8. Strokefinder MD100 developed by a team of prof. Perrson from Sweden (a) and receiver operating characteristic curve and area under the curve (AUC) value (b). Taken from [88].

The research teams of Prof. Francesca Vipiana, The University of Torino and Prof. Lorenzo Crocco, The Institute for the Electromagnetic Sensing of the Environment, National Research Council of Italy are designing a microwave imaging system for stroke monitoring. In [90] the first prototype of a microwave imaging system specifically designed for continuous monitoring of stroke patients immediately after stroke onset and diagnosis was demonstrated. In [56], [91] designed a helmet with 24 antennas to continuously **monitor brain stroke in the postacute stage**. Each of the 24 antennas is placed inside a dielectric 'brick', which works as the coupling medium to maximize field penetration within the head at frequencies 0.8 – 1.2 GHz [92]. Preliminary experiments with homogenous liquid phantom confirm the potential of the technology in imaging a spherical target that mimics a stroke of a radius equal to 1.25 cm [56]. The system was evaluated in [81] by numerical analysis with a 3D phantom. Numerical analysis showed that the system is capable of imaging ischemic and hemorrhagic strokes of 1 cm in size, which is related to the resolution of the MW imaging system at 1 GHz, which is approximately 1 cm. The experimental validation of the MW system was introduced in [93], where in the first scenario the head was represented by a 3D printed plastic container with a homogenous liquid phantom and in the second more complex

scenario the head was represented with calf brains in the plastic head phantom. The stroke was represented by a thin plastic container filled with a liquid mimicking hemorrhagic or ischemic tissue with a volume of around 50 cm^3. The truncated singular value decomposition (TSVD) algorithm can **locate the stroke position properly, but it misses part of the stroke size**. The MW system is used to monitor stroke in the postacute phase, where **stroke size is an important parameter to monitor**. For the clinic application of MW systems for stroke monitoring based on TSVD differential imaging, it is necessary to have a very good numerical model that will provide the device-specific mathematical operators needed to build an accurate and reliable imaging kernel [94]. Using the 24 antenna system mentioned above and the linear scaling operator, a method was presented to obtain data for training and testing classification algorithms [95]. The method is further described in the chapter on machine learning algorithms.

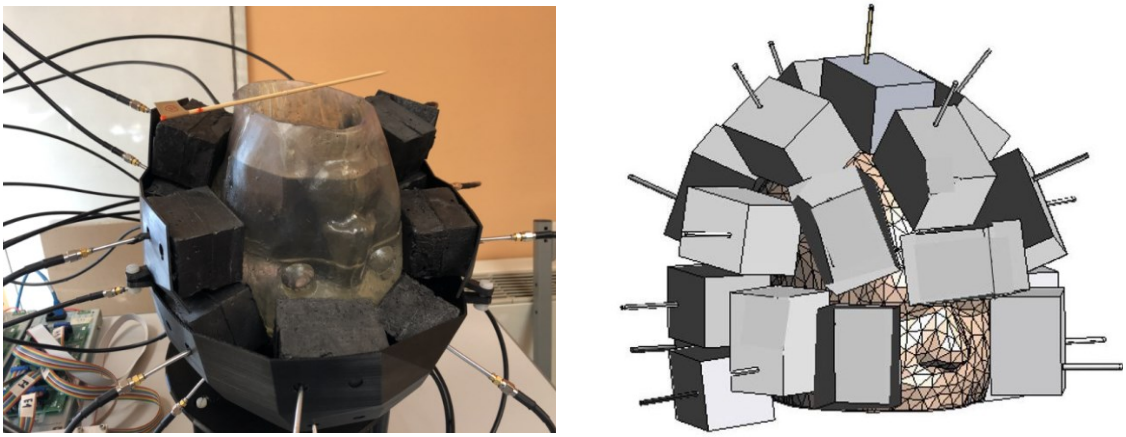

(a) (b)

Figure 9: A microwave system for brain stroke imaging. (a) prototype from [56] and (b) numerical model from [95].

1.4 Machine learning algorithms for stroke classification

Machine learning algorithms seem to be a promising method for use in medical diagnostics. In the context of stroke, machine learning algorithms are commonly used to identify stroke risk and forecast it based on patient information [96], [97]. In [97] used dataset with observation issues with 12 attributes relevant to brain stroke Random Forest, Support Vector Machine (SVM) and Decision Tree classifiers are applied. This is only the probability of stroke risk, which is not our goal. Another common application of machine learning algorithms is stroke classification on CT or MRI scans. In [98], [99] machine learning algorithms were used to classify CT scans of patients (image processing review in [100]) with ischemic and hemorrhagic stroke. Although machine learning algorithms help to classify the type of stroke, this is based on images taken in the hospital and is still not a prehospital diagnosis.

Microwave detection and classification based on machine learning algorithms is a new diagnostic option. For a quick prehospital diagnostic, it is enough to decide whether the patient is ill or not or to detect the type of disease. Such cases may be a stroke or cancer. Properly constructed machine learning algorithms can quickly recognize the presence of pathological tissues only according to the measured data. When using machine learning algorithms, we do not obtain an image of the examined area, but only information about the presence of pathology.

Machine learning algorithms for microwave stroke classification are mainly used by the research team of prof. Persson from Sweden. In [1], results of two clinical studies were presented with the conclusion, that that microwave-based measurements can differentiate hStroke from iStroke in acute stroke patients, as well as differentiate iStroke from healthy volunteers. Data from microwave broadband technology at frequencies 0.3 - 3.0 GHz were used for the machine learning algorithm based on singular value decomposition. On a very small amount of data was sensitivity 99.9 % to detect hStroke, the proportion of iStroke patients safely differentiated was approximately 30%, whereas at 90% hStroke sensitivity, 65% of iStroke patients could be differentiated. For more complex algorithms testing, it is necessary to obtain a larger amount of data. Another clinical study [88] investigated whether algorithms could distinguish patients with traumatic intracranial hematomas, chronic subdural hematomas, from a group of healthy

patients. At 100% sensitivity, the specificity was 75% - i.e. all hematomas were detected at the cost of 25% false positives. Clinical studies are time-consuming and costly, and the number of included patients should be kept at a minimum. On the other hand, machine learning methods usually require large amounts of training data to reach high accuracy. Therefore, it is necessary to investigate how the amount of training data relates to the performance and accuracy of the algorithm.

In [101], Candefjord et al. **created, using 2D numerical simulations, data corresponding to patients with intracranial bleeding (subdural hematoma)** of 4 sizes and 10 positions evenly spaced along the brain–cranium interface. One symmetrical head was scaled to 7 sizes. No realistic head models were used. To increase data variability, the thickness of the skull layer was varied, a small elliptical cerebrospinal fluid (CSF) region was added to the interior of the brain, and the head was rotated randomly between ±6°. A wide frequency band of 100 MHz to 3 GHz was used to create a dataset of 1500 observations (250 observations per bleeding size and 250 observations without bleeding). The authors do not mention any formatting of the data; feature selection or feature extraction techniques. When using the entire data set, the bleeding classification accuracy was 87-86% for the SVD-based classification algorithm. However, high classification accuracy required a relatively large training data set, and classification accuracy dropped when smaller subsets of data were used. The suitability of the data for training the algorithm was not investigated, but the training data were randomly drawn from a large dataset with approximately even distributions of bleeding sizes, head sizes, and helmet positions. Results in [101], [102] in addition to reliable detection, may have additional clinical value in estimating the size and location of the lesion. Both studies modelled the subdural hematoma in 2D, a crescent-shaped intracranial bleeding located between the skull bone and the brain. Subdural hematoma is different from intracerebral hemorrhage, which is the most common type of bleeding in stroke patients. Intracerebral bleeding is located within brain tissue and is commonly spherical and generally smaller in volume than a subdural hematoma. The authors also acknowledge that the 2D model is a significant simplification, and therefore it is unclear to what extent the results from such a model can be generalized to real measurements made in 3D. The development of a 3D model is therefore important, but running thousands of numerical simulations is a computationally intensive and time-consuming task.

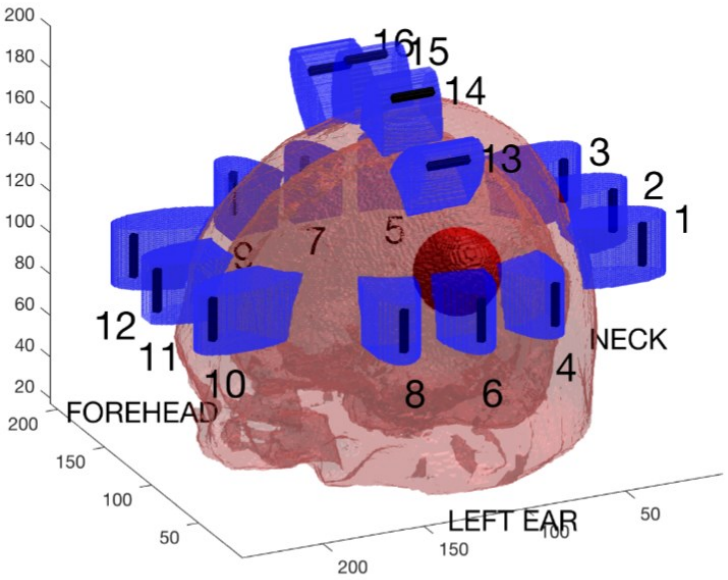

Figure 10: The 3D numerical model from [103] used for the investigation of how the machine learning algorithm distinguishes healthy individuals from subjects with intracranial bleeding.

This was followed by a 3D numerical study [103] where, Fhager et al. where a **3D human head model with intracranial bleeding was used**. It was investigated how a machine learning-based classification algorithm distinguishes healthy individuals from subjects with intracranial bleeding based on the number of subjects needed for training. A computational model, consisting of a realistic human head models of bleeding patients, as well as healthy subjects, was virtually inserted into an antenna array model. One single normal head model was used as the starting point, which in all simulation was randomly rescaled to resemble a natural variation of skull sizes[104]. The bleeding was placed randomly inside the brain with randomly varying volumes of 0-150 mL of spherical shape.Therefore, a large data set was generated with a total of 1000 subjects, where 500 were patients and 500 healthy models. The frequency range of 0.4-1.2 GHz was utilized in the simulation, and random white noise was added to the data to enhance the realism of the simulated microwave systems. The results are comparable to previous clinical studies [101]. There may be two reasons for the higher accuracy in the previous study. First, the variability in 2D geometry was less than in 3D; e.g., the bleeding geometry was more complex in 3D. Second, the bleeding in the 2D study was generally larger and not as deeply embedded as here. Therefore, the authors concluded that **large-scale clinical trials with several hundred patients are needed for practical and clinical verification of the technique**.

In [95] the authors from Torino, Italy, proposed an **alternative and efficient method to create the training dataset**, based on the distorted Born approximation. The method is using a linear scattering operator from the dielectric contrast space to the scattering parameters (S-parameters). Preliminary analyses with a homogeneous head model were recently presented in [105]–[107]. In [95] a dataset containing 10,000 samples from a 3D multi-tissue numerical head model was created in a relatively short time. Only one CAD model of the human head was used and scaled to obtain 10 models. The algorithms were tested on a large number of data obtained from the linear scattering operator, but the suitability of using the data for training was not evaluated. In our study, testing of the algorithm with multifrequency data was also performed although the results show that single frequency is sufficient.

Classification using SVM algorithm with inverse Fast Fourier Transformation (FFT) for the transformation of the S-matrix from the frequency domain to time domain was used in [82]. Data were obtained for 10 human head models without scale and only for ellipsoid stroke of 10 mm^3 to 35 mm^3 in random positions. A total of 100 stroke head models were built (50 for iStroke and 50 for hStroke). **The classification was only between the iStroke and hStroke classes, the healthy individuals class was not included**. Data variability was increased by adding noise, which also significantly reduced the classification success rate from 94% to 77%. Subsequently, the study was extended in [108] to Principal Component Analysis (PCA) to extract the electromagnetic signal directly and select the main component for classification. The classification results after PCA and SVM achieved 99% accuracy. **A low number of training and testing samples were introduced. The authors did not investigate the selection of appropriate training samples**.

In [109], a **transmission-line (TL) based method** was introduced that can identify the stroke type from the measured microwave signals S-parameters. The circular head under classification is surrounded by a two-antenna system that rotates and collects the S-parameters at several positions around the head. The classification was based on the correlation of the signals on a transmission line without the need for a training phase. The results show that significant differences can be observed for the computed correlation between the hStroke and iStroke cases**. However, the head was spherical in shape, which may significantly increase the correlation of the signals**. The authors themselves admit that an anatomically realistic phantom should be used to emulate real medical scenarios.

In studies [110], [111] **authors from China validated the diagnosis and monitoring of stroke types using a multichannel microwave-based stroke detection system in rabbits**. They conducted controlled experiments on an internal capsule cerebral hemorrhage model and a bilateral carotid artery ligation ischemia model in rabbits. A new Euclidean distance transform method, namely, the reflection signal Euclidean distance (RSED), is proposed to transform the microwave scattering parameters into a new parameter, thus improving the discrimination between the hemorrhagic and the ischemic stroke. The transformed data were processed through the dimensionality reduction by PCA and the SVM classification algorithm by PCA. These results demonstrate that the dimensionality reduction significantly improves diagnostic accuracy, because the accuracy without dimensionality reduction was between 50 and 70% and increases to 90–100% with dimensionality reduction. Since the head of a rabbit is significantly smaller than the head of an adult human (leading to a higher signal-to-noise ratio), a higher value of classification accuracy is to be expected. **These results are not transferable to human stroke detection and classification.**

In [112] the **authors from China presented a wideband microwave system and classification by SVM into two classes**. The system was verified in one simplified cylindrical glass container and a test tube with a diameter of 4 cm. The cylinder was filled with oil, and the tube is filled with water, which have high contrasts of dielectric parameters not corresponding to the reality of the human head. The position of the tube was changed randomly to obtain 120 independent measurement of S-parameters. From

the S-parameters, phases and amplitudes were calculated and dimensionaality were reduced by principal component analysis (PCA). SVM classification reaches 100%, but the **the variability of the data here is practically zero and the contrast of the classified data was far from resembling the real use of the system.**

In our team, in collaboration with colleagues from The University of Trento, Italy, several studies were presented dealing with the classification of stroke using a microwave system. Several measurements have previously been performed using the first version of an experimental microwave system and a water phantom [58]. The measured data were processed using the SVM algorithm in studies [113] and [59]. In the study [113], the SVM algorithm was used to classify the presence or absence of a stroke on a simplified water-based phantom of the head. A very high accuracy of stroke detection was achieved even with a limited amount of data used to train the algorithm. This study was extended in [59] by including the distinction between ischemic and hemorrhagic strokes. In the study [60], a multistep strategy for stroke detection, stroke type classification, and stroke position localization was presented. The study showed that stroke type classification is a more difficult task than stroke detection and requires an increase in training data for the SVM algorithm. Furthermore, the authors found that the support vector regression (SVR) is suitable for stroke localization. Using SVR improves the estimation of the x and y coordinates of the stroke location. **The algorithms were tested on data with low natural variability:** 10 antennas MW system with a liquid head phantom and a cylindrical stroke of size 40 mm in diameter [58].

1.5 Main goal and testing scenarios

The main goal of the dissertation thesis is **to systematically test the capabilities of machine learning algorithms in the microwave detection and classification of strokes** using realistic models of the human head. To achieve this goal, it is necessary to obtain large datasets of training and test data, which can be obtained synthetically through numerical simulations and experimentally via measurements. This requires the creation of numerical models and conducting extensive numerical simulations, as well as creating phantoms for experimental measurements and developing a methodology for measurement and data storage. To evaluate the performance of machine learning algorithms in microwave detection and classification of strokes, several test scenarios were defined. Since the numeric simulations for the 3D geometries and frequencies considered here are time- and computationally intensive, the largest data sets were created using numeric simulations in 2D.

We will investigate effects of reducing the number of training data or subjects, reducing the dimensionality of the data, selecting, and configuring the algorithm, and varying the frequency range depending on the use of algorithms for pre-hospital stroke diagnosis.

1.5.1 Datasets created via 2D numerical simulations.

Using 2D numerical simulations, due to their low computational demands, a large amount of data can be generated even in a relatively short time. By analyzing the results obtained via 2D simulations, it is possible to reduce the size of the training and test datasets for more computationally demanding 3D simulations and measurements.

The motivation behind the initial testing scenario was based on the fact that for data classification, the SVM algorithm identifies a linear or hyperplane boundary between different classes. The SVM algorithm locates the support vectors, which are the closest data points to the boundary, and uses them to construct the decision boundary. It is possible that small stroke sizes may form support vectors due to their lower variability in the data and, therefore, play a significant role in determining the decision boundary. Based on this observation, we proposed first testing scenario (**S1**) where we verify if **the most suitable training data are from subjects with small strokes**.

The S-matrix of the measurement system can be obtained for multiple frequency points. However, such measurements are more time consuming and require higher bandwidth of the antennas and the measurement hardware. For rapid stroke detection and classification of stroke type, a single frequency measurement might be sufficient. Based on this, we define the second testing scenario (**S2**) where we verify if **single-frequency and multi-frequency training data lead to the same classification accuracy.**

If the scenario S1 is confirmed, our next objective is to demonstrate the generalization capability of the SVM algorithm. We aim to find out whether the SVM algorithm trained on data from subjects with small strokes can also accurately classify medium and large strokes. This can be accomplished by using the same stroke positions for training and testing, but with the test data consisting of even larger stroke sizes. We propose the third testing scenario (**S3**) where we investigate if a **SVM algorithm trained on data from subjects with small strokes can accurately classify randomly sized strokes.**

Subsequently, we intend to evaluate the generalization capability of the SVM algorithm to classify strokes (of random sizes) at random positions, which represents a practical clinical scenario. Hence, we proposed to test (**S4**) if a **SVM trained on data from subjects with small strokes can accurately classify randomly sized strokes at random positions**.

The choice of the SVM algorithm is based on previous studies [59], [60], [114], where the algorithm's performance was evaluated using experiments with a single liquid head phantom. However, the presence of higher data variability may lead to a decrease in the efficiency of the SVM algorithm. As such, we have selected a total of 5 alternative algorithms based on learning by examples (LBE) that are implemented in MATLAB Statistics and Machine Learning Toolbox. These algorithms are Logistic Regression (LR), Discriminant Analysis (DA), k-Nearest Neighbors (kNN), Naive Bayes Classifier (NB), and Classification Tree (CT). The accuracy of the classification of these 5 algorithms and SVM will be evaluated and mutually compared in fifth scenario (**S5**) where we verify if a **SVM algorithm is suitable for stroke detection and classification.**

1.5.2 Datasets created via 3D numerical simulations

Key conclusions made by means of data obtained from 2D simulations must first be confirmed for 3D simulation results. The initial testing scenario for datasets obtained via 3D numeric simulations (**S6**) is used to verify whether a **SVM trained on a 3D data from subjects with small strokes can accurately classify randomly sized strokes.**

Classification accuracy could depend on the choice of suitable dataset format. S-parameters, as well as any other complex numbers, can be expressed in cartesian complex plane by real and imaginary parts or in polar complex plane by modules and phases (argument). Despite its importance, the format of training data is not given sufficient attention in the literature. To investigate the impact of data format on classification success rates, we propose testing scenario (**S7**) where we tested if a **SVM algorithm trained on data sets in real and imaginary part format will show higher classification accuracy than in module and phase format.**

The S-matrix consists of reflection coefficients located on its main diagonal and transmission coefficients located elsewhere. Based on the model verification results (see Appendix C), the reflection coefficients are less affected by the presence of stroke. Using the transmission parameters for algorithm training (leading to smaller dimensionality of the dataset), may result in a better trained model and higher classification accuracy. The seventh test scenario (**S7**) we test if a **SVM algorithm trained on transmission coefficients will show higher classification accuracy than trained on the entire S-matrix.**

The utilization of the SVM algorithm in pre-clinical settings, such as ambulance, necessitates an accurate classification of stroke type. As approximately 85% of strokes are ischemic [3], the SVM algorithm should have a higher success rate compared to statistical probability. The nineth test scenario **(S9)** we tested if **the accuracy of an SVM classification model trained on a 3D numerical dataset will exceed 85% when classifying randomly sized strokes at random positions**.

Considering that approximately 85% of strokes are ischemic [3] and that prompt initiation of treatment is critical in reducing the impact of the disease [15], it is essential to definitively diagnose ischemic strokes in order to initiate thrombotic therapy safely.

The tenth test scenario was proposed based on the recognition that accurate classification of ischemic strokes has the potential to positively impact a large number of patients by reducing the consequences of the disease [13]. In tenth test scenario (**S10**) we tested if **The SVM algorithm can reliably classify ischemic strokes, which would enable safe initiation of thrombotic therapy for a 3D numerical dataset.**

1.5.3 Experimental measurements

To validate the key conclusions arising from 2D and 3D numerical simulations, it is necessary to confirm them through experimental measurements. The first test scenario for the dataset obtained from experimental measurements on a liquid head phantom and a realistic head phantom **(S11)** we tested if **SVM trained on experimentally measured dataset consisting of small stroke sizes will be able to generalize and accurately classify larger stroke size.**

As with the 3D numerical simulations, we aim to verify the experimental measurements to determine if the SVM has higher success rates than the statistical probability of stroke, which indicates that 85% of strokes are ischemic [3]. Another test scenario (**S12**) we tested if **The accuracy of an SVM classification model trained on an experimentally measured dataset will exceed 85% when classifying randomly sized strokes at random positions.**

Finally, we will use the data from experimental measurements to test whether the SVM algorithm can provide information necessary to safety initiate thrombotic therapy in ischemic stroke patients. The final testing scenario (**S13**) we tested if the **SVM algorithm can reliably classify ischemic strokes.**

2. Methods

The numerical simulator COMSOL Multiphysics [115] was used to create synthetic training and test data in the form of transmission and reflection coefficients (called scattering parameters or, shortly, S-parameters). The experimental system was used to obtain experimental measured data, and this data was then compared with the results of numerical simulations to validate the results generated through the numerical simulations testing scenarios.

2.1 Numerical models

The chapter is based on the author's article published in a journal with impact factor [116] and [117].

First, a 3D CAD model of the experimental microwave system [58] was created. The microwave (MW) system consisting of 10 fixed antennas (described in [118]) surrounding a human head model. Next, the geometry of the 3D numerical model was prepared from a cross-section of the 3D CAD model, specifically at the 100 mm coordinates which correspond to the plane of the antenna elements. A mesh was utilized in which the maximum value of the side length was set to 1/8 of the transverse electromagnetic wavelength in the given environment and for the operating frequency equal to 2 GHz.

The geometries of the models of all 10 human heads used in 2D and 3D are based on head models from the IT'IS Foundation's "The Population Head Model V1.0" database [119]. In Materialize 3-matic software [120], the mesh of the models was modified so that it could be imported and used for FEM simulations in COMSOL Multiphysics. The models contain layers representing the scalp, skull, cerebrospinal fluid, and brain (white matter and grey matter). Based on the resulting models, molds were also created to produce anatomically and dielectrically realistic phantoms.

Realistic dielectric properties values were assigned to the individual domains of the human head models, which represents different biological tissues, as well as to produce individual phantom layers. These values were determined using the frequency-dependent 4-pole Cole–Cole model [121]. Specifically, for the skull, CSF, and hemorrhagic stroke represented by the blood, the 4-pole Cole–Cole model parameters were directly adopted

from the IT'IS material parameter database V3.0 [37]. For the brain dielectric properties, we used average values of white matter, gray matter and cerebellum and for the scalp average values of skin and fat. The ischemic stroke represent a 15% reduction in the dielectric parameters of the brain [42], while the dielectric parameters of hemorrhagic stroke were set to be equivalent to blood. Matching medium dielectric properties are given by the IEEE standard [111]. The dielectric properties of the individual domains at 1 GHz are shown in Table 2.

Table 2. Dielectric properties of the domain in the human head modes at 1 GHz [37].

Tissue Layer	ε_r **(−)**	σ **(S/m)**
Scalp †	35.68	0.66
Skull	12.34	0.16
CSF	68.44	2.46
Brain ‡	40.00	1.00
Ischemic stroke	34.00	0.85
Hemorrhagic stroke	61.07	1.58
Matching Medium *	40.00	1.00

† Average parameters of skin and fat. ‡ Average parameters of grey matter, white matter, and cerebellum.
* Matching medium dielectric properties are given by the IEEE standard [122].

The COMSOL Multiphysics simulations were controlled with in-house written MATLAB scripts. These scripts specifically set the operating frequency, stroke type, size and position, head models size scaling, and saved the resulting S-matrices together with the numerical model settings to a MATLAB structure matrix file.

2.2 2D numerical models and simulations

The chapter is based on the author's article published in a journal with impact factor [116] and [117].

The 2D geometry of the model was described in the Section 2.1. Absorption boundary conditions are set around the entire outer perimeter of the computational domain. The antenna elements used in this study are inspired by the slot antenna from [118]. An antenna 2D equivalent model consists of a rectangle representing a conductive cavity and a slot was used in simulations (see Figure 11). A slot segment was created on

the perimeter of the rectangle facing the displayed area and the boundary condition of the port (“User defined”, Ez) was assigned to it. The rest of the perimeter of the rectangle antenna was assigned a perfect electric conductor boundary condition. The sizes of the antenna segments representing the slots were changed to find the global minimum of a cost function using the genetic algorithm. We minimized the transmission parameter differences between the optimized 2D model and the reference experimental measurement for the entire 10-port system. The genetic algorithm minimizes the fitness function [123]:

$$fit = \sum_{n=1}^{n} \sum_{m=1}^{m} \frac{|(ref_{nm} - opt_{nm})^2|}{|ref_{nm}^2|}\ , \tag{1}$$

where n are rows and m are columns S-matrix, ref is reference (experimental measurement) S-matrix and opt S-matrix calculated from the optimalization 2D numerical model. The inner part of the antenna array was filled only with the matching medium. The maximum possible agreement between the transmission coefficients for 2D numerical simulation and experimental measurement was achieved. Antennas operate in the frequency range from 0.8 GHz to 2 GHz.

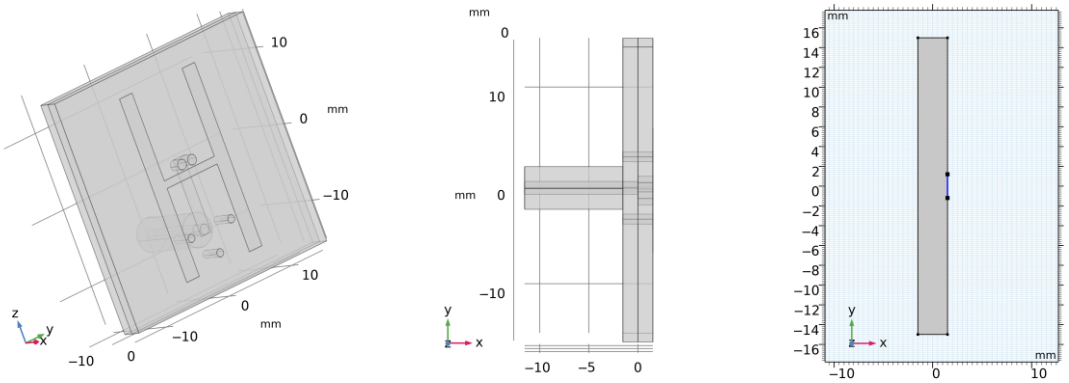

(a) (b) (c)

Figure 11. (a,b) is the 3D geometry of the slot antennas [118] and (c) is the final 2D antenna model, where segment representing the slot (marked in blue) was changed to achieve maximum agreement between calculated and measured transmission parameters of the laboratory system.

The 2D geometries of the models of all 10 human heads are depicted in Appendix A. The dielectric properties of individual domains representing different biological tissues vary with the frequency used and were calculated using the Cole model. Target values for a frequency of 1 GHz are listed in Table 2. The stroke locations are represented by a circle with diameters from 20 to 40 mm placed in different positions in the brain domain shown in Figure 12.

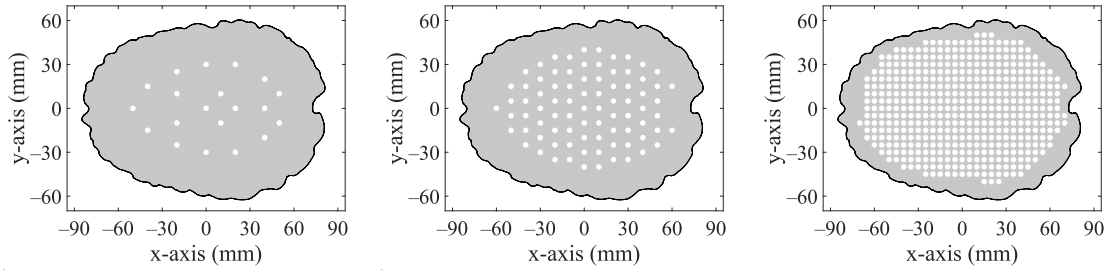

Figure 12. 20 positions (a), 83 positions (b), and 456 positions (c) in the brain where strokes of various sizes were placed.

The 2D numerical training and testing datasets were automatically generated using the reconfigurable 2D numerical model in COMSOL Multiphysics controlled with in-house written MATLAB scripts. According to studies [59], [124], the most suitable operating frequencies for MW imaging are around 1 GHz. Our datasets contain simulation results for 25 equidistant frequency points ranging from 0.8 to 2 GHz.

The head models were based on 10 different patient-specific geometries. To increase the variability of tested datasets, the geometries of the head models were scaled to 95–105% of their original size independently in the x and y directions. The scaling factors were determined for each data point using a uniform probability density random number generator. We used 2 types of strokes: Ischemic stroke (iStroke) caused by blockage of a blood vessel by a clot and hemorrhagic stroke (hStroke) caused by intracranial bleeding, also the scenario without stroke (noStroke) was used. Three datasets have been generated as summarized in the text below and Table 3.

Table 3. The parameters of the models in the datasets of 2D numerical simulations.

DataSet (−)	Stroke Type (−)	Stroke Sizes (mm)	Stroke Positions (−)	Head Models (−)	Head Scaled (%)	Frequency Points (−)
2D_1	hStroke iStroke noStroke	20, 25, 30, 35, 40	Fixed 20 + 83 + 456	10	95–105 †	25
2D_2	hStroke iStroke noStroke	20–40 †	Fixed 20	10	95–105 †	25
2D_3	hStroke iStroke noStroke	20–40 †	Random 20 †	10	95–105 †	25

† Uniform probability density random number generator.

DataSet 2D_1 includes 2D simulation results for subjects with five different stroke sizes (20, 25, 30, 35 and 40 mm in diameter) of both stroke types placed at 20 predefined positions within randomly chosen and scaled head models. In total, 1000 simulations were for each stroke type, and 1000 simulations of randomly scaled head models without stroke. Therefore, 3000 calculations of S–matrices were done for one frequency point. DataSet1 was subsequently supplemented with data generated in the same way for 83 and 456 different stroke positions.

DataSet 2D_2 includes the simulations results for subjects with ischemic and hemorrhagic strokes of random size (ranging from 20 to 40 mm in diameter determined using uniform probability density random number generator) placed at 20 predefined positions within randomly chosen and scaled head models. In total, 200 simulations were computed for each type of stroke and 200 simulations for randomly scaled head models without stroke.

DataSet 2D_3 includes the simulations results for subjects with ischemic and hemorrhagic strokes of random size (range from 20 to 40 mm and determined using uniform probability density random number generator) placed at random positions within randomly chosen and scaled head models. In total, 200 simulations were calculated for each type of stroke and 200 simulations for randomly scaled head models without stroke.

2.3 3D numerical models and simulations

The 3D geometry of the MW system was described in Section 2.1 The operating frequency 1 GHz was used in the 3D numerical simulations. The 3D geometries of the models of all 10 human heads are depicted in Appendix B. The dielectric properties of individual domains representing different biological tissues for a frequency of 1 GHz are listed in Table 2. The tetrahedral mesh was used to generate a mesh for each layer of the 3D model. The resulting meshes for one head model are depicted in Figure 13.

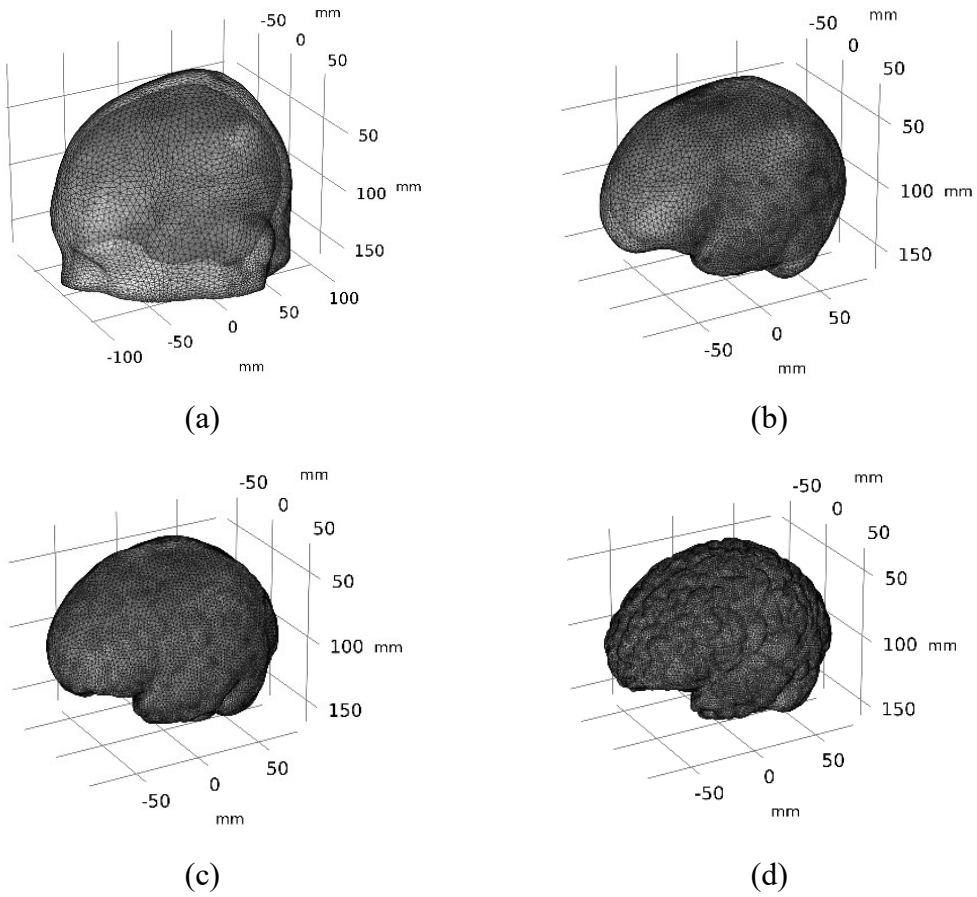

Figure 13. 3D numerical model of a human head models composed of (a) scalp, (b) skull, (c) CSF, and (d) brain.

The spherical model of the stroke was placed in the plane of the antennas. The stroke locations are placed in 7 and 20 different positions in the brain domain shown in Figure 14.

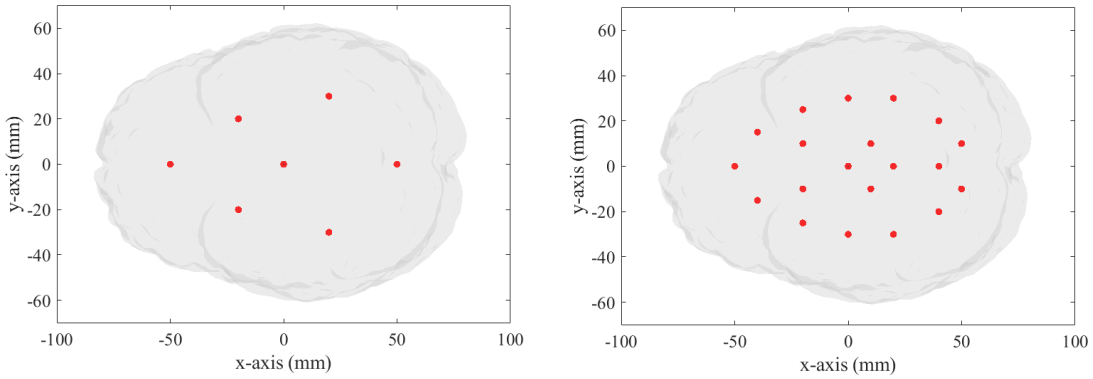

(a) (b)

Figure 14: Brain tissue model with red marked 7 positions (a) and 20 positions (b) where the spherical stroke model was virtually placed.

The 3D numerical training and test datasets were automatically generated using the reconfigurable 3D numerical model in COMSOL Multiphysics controlled with in-house written MATLAB scripts. These scripts set the head and stroke model parameters, operating frequency, and saved the resulting S-matrices. Three datasets have been generated. Datasets are summarized in the Table 4. To increase the data variability, noise was added to the iStroke and hStroke data. We used random white noise at level 85 dB, which corresponds to noise in experimental measurements described in the following chapter. Used 10 head models allow to generate only 10 noStroke S-matrices for training and test the algorithm. The number of noStroke data was extended by repeatedly inserting noise into 10 simulated S-matrices, which therefore corresponds to repeated measurements of patients.

Table 4. The parameters of the models in the datasets of 3D numerical simulations.

DataSet (-)	**Stroke type (-)**	**Stroke sizes (mm)**	**Stroke positions (-)**	**Head models (-)**	**Frequency points (-)**	**DataSet size (-)**
3D_1	hStroke iStroke noStroke	20,30,40	Fixed 7	10	1	210 210 70‡
3D_2	hStroke iStroke noStroke	20	Fixed 20	10	1	200 200 200‡
3D_3	hStroke iStroke noStroke	20 - 40†	Random 10†	10	1	100 100 100‡

†Uniform probability density random number generator. ‡ Data from one numerical simulation for each of the head models were extended by adding random noise at the 85 dB level.

2.4 Numerical models validation

This chapter is based on the author's article published in a journal with impact factor [116].

Validation of the numerical models was done in two steps. First, we directly compared the (synthetic) S-parameters obtained from simulations using 2D and 3D models (the geometries of these models are shown in Figure 24 and Figure 25). and measurements using the laboratory prototype of a MW system shown in Figure 15. For the 2D and 3D simulations and measurements, the inner part of the antenna array was filled only with the matching medium, which allowed us idealized comparisons of all these scenarios. Values of the magnitude differences were displayed for the 2D numerical model versus the 3D numerical model, and for the 3D numerical model versus the experimental measurements. Relative magnitudes differences are defined as:

$$\Delta M_{ij} = 20 \cdot \log_{10}\left(\left|\frac{S_{ij}^{A}}{S_{ij}^{B}}\right|\right), \tag{2}$$

where S_{ij}^{A} and S_{ij}^{B} denote the compared scattering parameters calculated or measured. Magnitudes differences of S-parameters are listed in Appendix C.

In the second step of the numerical models validation, we inserted the ischemic and hemorrhagic stroke inside the antenna array, specifically at the center and at position (−20, 30) and compared the magnitude differences in the 2D and 3D numerical models and the measurements.

2.5 Measurements

This chapter is based on the author's article published in a journal with impact factor [118] and conference papers [125].

2.5.1 Laboratory prototype of MW system

An experimental MW system was designed for measurements with head and stroke phantoms. The system (see Figure 15) [58] consists of a plastic 3D printed container/holder for the 10 antenna elements [118].

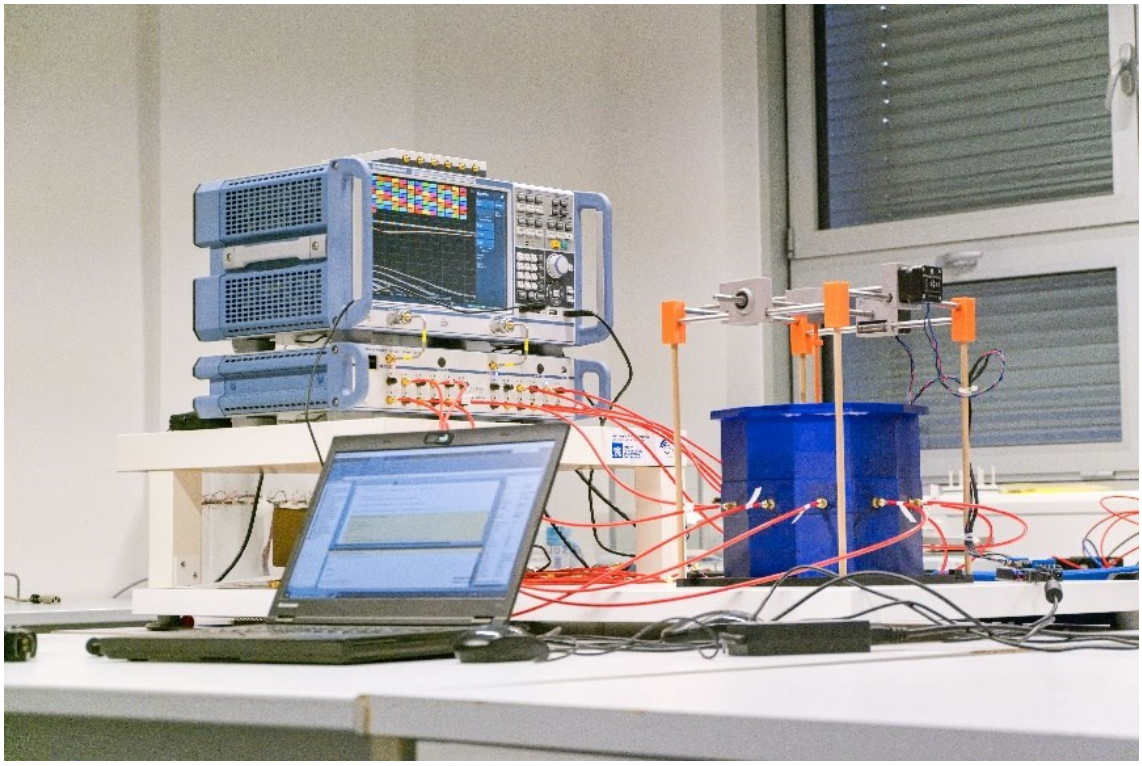

Figure 15. A laboratory prototype of a microwave imaging system with a computer-controlled stroke positioning system and measurement devices.

2.5.2 Human head and stroke phantoms

The chapter is based on the author's article published in a journal with impact factor [126].

To fabricate a multilayer solid head phantom, we designed phantom molds with anatomically realistic shapes [127]. Phantom molds were designed based on MRI-derived scans adopted from The Population Head Model V1.0 of IT'IS Foundation database [119]. We used 3D printing technology for the printing of molds suitable for filling with a

mixture of polyurethane and conductive powders [125]. The skin mold was divided into two parts because of the production of a phantom that can be better removed from the mold. The inner molds (bone, cerebrospinal fluid, and brain) were solid because it is necessary to ensure their mechanical strength for pressing into the outer mold. The brain mold represents the anatomy of white matter. The phantom was prepared using mixtures of polyurethan rubber, graphite powder, carbon black powder, and acetone (refer to Table 5 for material specification).

Table 5. Phantom materials to be used in the fabrication of the solid tissue layers of the human head phantom.

Material	**Model**	**Manufacturer**
Polyurethan rubber	VytaFlex^{TM} 20	Smooth-On, Inc (US)
Graphite powder	282863 – Graphite	Sigma – Aldrich (US)
Carbon Black powder	45527 Carbon black	Alfa Aesar (US)
Acetone	99.9% Acetone	Lach-Ner, s.r.o. (CZ)

The head phantom fabrication process is described in detail in [126] for 2.5D version. However, in this work the molds now represent the 3D anatomy of the head, so it is important to keep the depth of the inner mold, which is slowly pressed into the homogeneous mixture to create the layers. The depth of pressing is controlled by stops, which are located on all internal molds and fit exactly into the external mold of the scalp; see Figure 16. Another advantage of these stops is the precise maintenance of the position of the inner mold and thus the maintenance of a precise distance from the wall of the outer mold. The phantom of the human head with layers of skin, bone, and CSF forms a waterproof container where a liquid brain phantom can be placed. The phantom of the brain consists of distilled water, isopropanol, and salt and represents the proportional dielectric properties of the grey matter of the brain, the white matter of the brain, and the cerebellum.

Figure 16: 3D printed molds for manufacturing of the 3D solid head phantom. Precise positioning of the inner mold in the outer mold, due to stabilizing stops, which also follow the exact pressing depth of the inner mold.

Similar to the head phantom, we developed demountable molds to produce the stroke phantom. These molds enabled the accurate and reproducible manufacturing of the spherical stroke phantom with a diameter of 20 mm, 30 mm, and 40 mm. Phantoms with dielectric properties of ischemic stroke (iStroke) and hemorrhagic stroke (hStroke) was created. We created an ischemic stroke phantom to represent a 15% reduction in the dielectric parameters of the brain [42], while the dielectric parameters of hemorrhagic stroke were set to be equivalent to blood. Stroke phantom form a mixture of graphite powder, carbon black powder, and polyurethane rubber [126].

The Dielectric parameters of individual layers of human head phantom and stroke phantoms were measured using the SPEAG Dielectric Assessment Kit (DAK, Schmid & Partner Engineering AG, Switzerland) with the probe DAK-12 in the frequency range 0.5-3.0 GHz. The dielectric properties of each layer were compared with target dielectric properties (see Table 2) obtained from the IT'IS material parameter database V3.0 [37] at frequency 1 GHz.

2.5.3 Computer-controlled stroke positioning system

The computer-controlled stroke positioning system was developed to adjust the XY position of a stroke phantom inside the head phantom. Components for 3D printers were used to design a precise and reliable computer-controlled system for adjusting the position of a stroke phantom. Specifically, smoothed travel rods, stepper motors with a trapezoidal rod, ball bearings and linear bearings were used. Stepper motors are controlled using in-house written MATLAB scripts and the Arduino platform. Microwave measurements are also controlled from the MATLAB environment using a vector network analyzer.

The 3D printed parts were designed in the 3D Builder program. Corner parts were used to fix travel rods and standing legs, see Figure 17 (a). Stepper motor holders are used for stable mounting of the motors to the travel rods and contain space for linear bearing insertion, see Figure 17 (b). The bearing holders contain space for a linear bearing and a ball bearing which is used to stabilize the stepper motor and easily rotate the trapezoidal rod, see Figure 17 (c). The moving center part contains space for insertion of two trapezoidal screws and consists of a mechanism for holding a stroke phantom, see Figure 17 (d). The attachment of the stroke phantom is designed using a plastic rod that contains a semicircular cap, Figure 17 (e). The mechanism to secure the plastic rod is presented in Figure 17 (f) and works on the principle of rotating the rod by 180 degrees and inserting a stop part, which prevents the plastic rod from turning back and falling out, see Figure 18. The parts were printed on 3D printer Prusa I3 MK3s with polyethylene terephthalate glycol-modified PETG and glued with polyurethane glue. Wooden rods were used as standing legs. Due to the power consumption of the stepper motors an external 12V and 1A power supply was used.

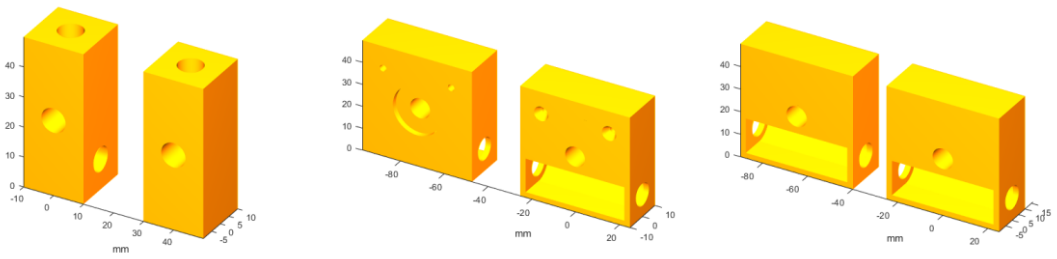

(a) (b) (c)

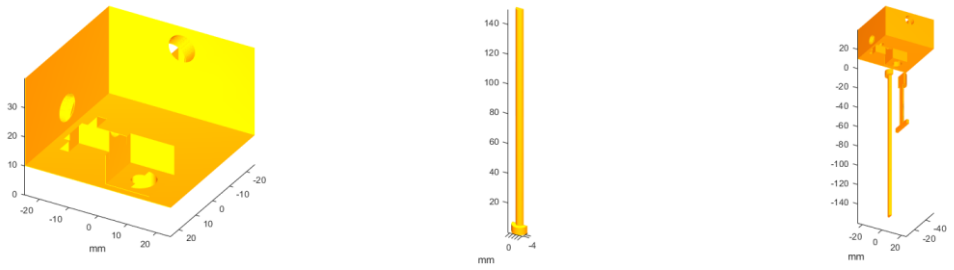

(d) (e) (f)

Figure 17. 3D printed parts. (a) Left and right corners for mounting the travel rod and the standing rod. (b) Stepper motor holders for mounting the linear bearings and stepper motor. (c) The bearing holders for mounting the linear bearing and fixing the trapezoidal rod by ball bearing. (d) Middle part with a stroke holder mechanism and space for the insertion of two trapezoidal screws. (e) Stroke holder stick. (f) Parts of the stroke holder mechanism.

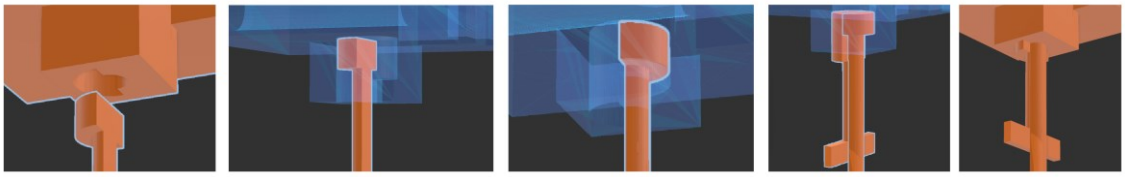

(a) (b) (c) (d) (e)

Figure 18. Stroke holder mechanism: (a) Middle part with the stroke holder mechanism and the stroke holder stick. (b) Stroke holder stick inserted into the mechanism. (c) Stroke holder stick rotated by 180 degrees. (d) Inserted stop part that fix the stroke holder stick. (e) assembled mechanism.

Arduino UNO with the L293D motor shield was used to control the stepper motors. The Arduino IO Package for MATLAB [128] was used. The source code (motor_v1.pde) has been uploaded to the Arduino board, which allows to receive commands from MATLAB. The rotation of the stepper motors with the trapezoidal rod causes a change in the position of the middle part. A MATLAB function was developed to control the stepper motor and move the middle part with the stroke holder mechanism to a defined position. Once the specified position is reached, the motors are turned off. This involves releasing the motors and interrupting the current flow. The center of the system is defined by the xy coordinates [0, 0]. Then, it is necessary to define positions for the movement of the middle part with the stroke phantom. The maximum range of motion in the liquid brain of human head phantom of the brain for the x axis was determined from -6 to 6 cm and the maximum range in the y axis was determined from -4.5 to 4.5 cm. However, it is necessary to consider the variability of the human head and the diameter of the stroke

phantom. The stroke phantom should not hit the walls of the phantom. If a 0.5 cm step is defined in the code for one cycle, the position of stroke phantom must be defined in multiples of 0.5 cm and finally multiplied by 2 to give an integer number for repetitions of cycles. The positions defined in this way can be used as input to the created function that controls the stepper motors. The control script of Computer-controlled stroke positioning system and 3D models are available for download at: printables.com/cs/model/75443/files.

Twenty different positions were selected along the xy-axis to position the spherical stroke phantom within the head phantom. Figure 19. depicts the xy-coordinates of the stroke phantom at each of these locations. It should be noted that the z-axis of the stroke phantom is aligned with the plane in the middle of the antennas.

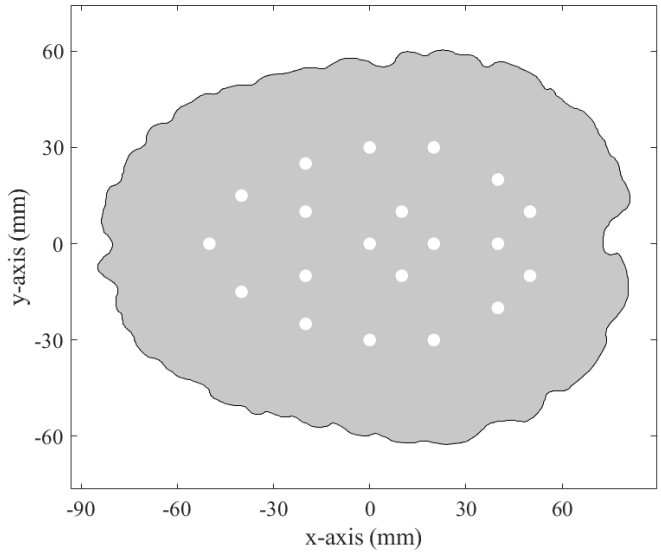

Figure 19: The 20 different x-y positions in the brain where the stroke phantom was placed using the computer-controlled stroke positioning system. The z-axis position of the phantom was set to the center of the antennas.

2.5.4 Training and testing datasets

Microwave measurements were conducted at a frequency of 1 GHz using an in-house written MATLAB script with a computer-controlled stroke positioning system and network analyzer ZNB8 equipped with a switching matrix ZN-Z84, both Rohde&Schwarz. A full-port calibration was performed before the measurement using the automatic calibration unit ZN-Z153 Rohde & Schwarz. The measurement script

initiated the movement of the stroke phantom to a predefined position and waited for the liquid level of the brain phantom to stabilize before initiating measurements of the S-parameters. The measured parameters were stored in a structured format, along with information about the position, size and type of the stroke phantom. Once the measurement was complete and the data saved, the stroke phantom was moved to the next predefined position, and the measurement process repeated. This automated process allowed for all 20 positions depicted in Figure 19 to be measured without any user intervention. Finally, the stroke phantom was returned to its initial coordinates. The measurement setup is shown in Figure 20.

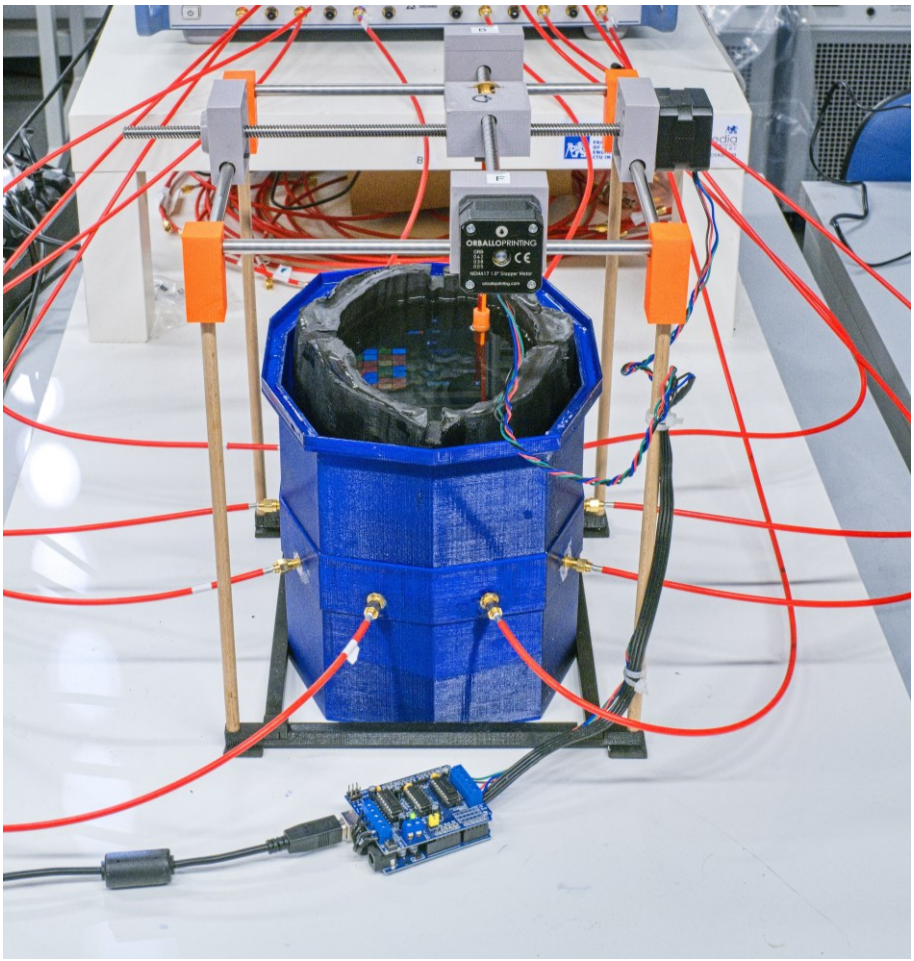

Figure 20. The measurement setup consists of an experimental microwave system, a multilayer head phantom, and a stroke phantom embedded in a computer-controlled stroke positioning system for motion along the x-y axis in a liquid head phantom.

Initially, measurements were performed on the experimental microwave system that was filled with a homogeneous liquid phantom. These measurements were conducted to evaluate the measurement noise and machine learning algorithm testing. Multiple measurements were taken between each stroke phantom measurement to obtain a larger dataset, which included a no-stroke scenario. As a result, two datasets were generated for the homogeneous liquid phantom, and they are presented in Table 6. Additionally, two datasets were generated for the realistic multilayer head phantom, and they are also summarized in Table 6.

Table 6: Phantom parameters in the DataSets of experimental measurements

DataSet (-)	Stroke type (-)	Stroke sizes (mm)	Stroke positions (-)	Head phantoms (-)	Frequency points (-)	DataSet size (-)
M_1	hStroke iStroke noStroke	20,30,40	Fixed 20	1 (liquid)	1	60 60 20
M_2	hStroke iStroke noStroke	20,30,40	Random 30†	1 (liquid)	1	90 90 20
M_3	hStroke iStroke noStroke	20,30,40	Fixed 20	1 (realistic)	1	60 60 20
M_4	hStroke iStroke noStroke	20,30,40	Random 30†	1 (realistic)	1	90 90 20

†Uniform probability density random number generator.

2.6 DataSets structure

A specialized custom file structure was designed in MATLAB to effectively store the large datasets generated from numerical simulations and experimental measurements. Example of dataset structure show Figure 21. Each row within the structure array contains data representing a different scenario. The columns of the structure array correspond to the various parameters and characteristics of the scenario. These parameters/characteristics are described in Appendix E:

MeasNo	StrokeType	StrokeSizeD	StrokePositionXYZ	PhantomType	ScalePhantomXYZ	ScaleDielParam	Freq	S_mat_Relm	Modul	Phase	AlgorData	Line_Relm	Line_ModulPhase
1	1	20	[-50,0,100]	310	[1,1,1]	1	1.0000e+09	10x10 complex...	10x10 doub...	10x10 doub...	1x110 double	1x110 double	1x110 double
2	1	20	[-20,20,100]	310	[1,1,1]	1	1.0000e+09	10x10 complex...	10x10 doub...	10x10 doub...	1x110 double	1x110 double	1x110 double
3	1	20	[-20,-20,100]	310	[1,1,1]	1	1.0000e+09	10x10 complex...	10x10 doub...	10x10 doub...	1x110 double	1x110 double	1x110 double
4	1	20	[0,0,100]	310	[1,1,1]	1	1.0000e+09	10x10 complex...	10x10 doub...	10x10 doub...	1x110 double	1x110 double	1x110 double

Figure 21. Example of dataset structure

2.7 Data analysis, format, and dimensionality reduction

Due to the "curse of dimensionality" [129], the required number of training samples to construct an accurate classifier increases exponentially as the dimensionality of the input data increases. Our objective is to reduce the number of necessary training samples.

2.7.1 Feature selection

The microwave system used in this study contains 10 antennas, as illustrated in Figure 22. The microwave measurement resulted in an S-matrix with dimensions of 10x10, corresponding to a total of 100 elements or 200 elements if considering both the real and imaginary components.

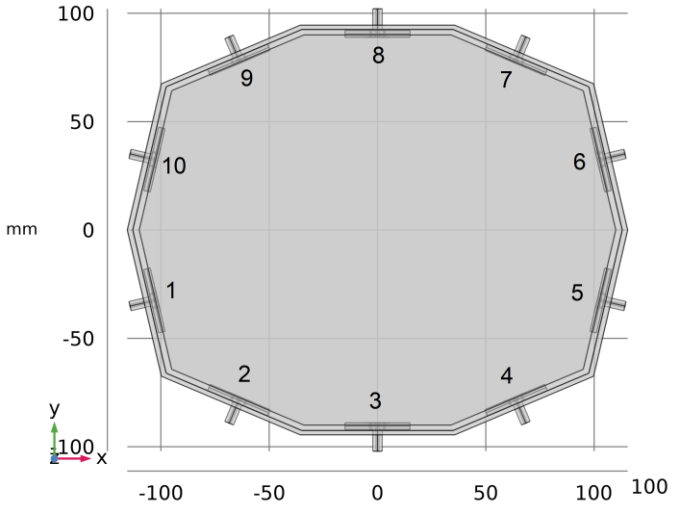

Figure 22. Antenna position numbers for the 10-antenna microwave system used in this study.

In the first step of dimensionality reduction, we employed the Lorentz principle of reciprocity ($S_{ij} = S_{ji}$) and only utilized only 55 independent elements of the S-matrix (elements on main diagonal and below). By dividing the complex values of these S-parameters into their real and imaginary components, we obtained a total of 110 observed features.

Two different formats of data were used to train and test the LBE algorithms. The first format of data consisted of the real and imaginary parts of the S-matrix elements, resulting in 110 features. The second format of data was modulus (in dB) and phase, again resulting in 110 observed features.

2.7.2 Principal component analysis

Principal component analysis (PCA) was used to further reduce the dimension for training and test data. Due to the further reduction of the dimension, the complexity of learning, the costs of the training phase and, above all, the number of required samples for accurate training of the algorithm are reduced. It is recommended to perform normalization of the data before applying PCA [130]. By normalizing the data, the features are formatted to be on a similar scale. This can result in a more robust representation of the data. The training and test data were preprocessed by centering and normalizing to the range of 0 to 1. Principal component coefficients were calculated for the training data using PCA, which was implemented through Singular Value Decomposition (SVD).

The optimal number of dimensions for the PCA-extracted features was selected based on the classification accuracy for various dimension sizes. The classification accuracy was assessed for a minimum of five dimensions, increasing by increments of five, up to the maximum number of dimensions.

2.7.3 Data variance and variability analysis

We analyzed the variance of the principal components in the 3D numerical data. A comparison was performed between the data represented in the real- and imaginary-part format (ReIm) and the data represented in the module and phase format (MoPh).

PCA represents the data in a new coordinate system. The first principal component (PC) describes the largest part of the variance of the original data, the second PC describes the largest part of the variance not contained in first PC and it is perpendicular to the first PC. The third PC describes the largest part of the variance not contained in first PC and second PC. Third PC is perpendicular to both the first and second PC. This orthogonal property allows us to visualize the first three components in 3D space, aiding in the exploration of relationships among the data. We created a 3D visualization of the first three principal components for dataset of 3D numerical data. In practice, algorithms may use additional PCs beyond the first three to capture more subtle patterns and enhance classification performance.

Additionally, for the 3D numerical dataset, we analyzed the variability of the data resulting from the insertion of ischemic and hemorrhagic stroke phantoms into the head phantom. We evaluated the relative magnitude differences between the S-matrices with and without strokes. Relative magnitudes differences are defined as:

$$\Delta M_{ij} = 20 \cdot \log_{10}\left(\left|\frac{S_{ij}^{A}}{S_{ij}^{B}}\right|\right), \tag{3}$$

whereS_{ij}^{A} and S_{ij}^{A} denote the scattering parameters in the presence or absence of a stroke, respectively, for each *i, j* antennas pair. Boxplots were used to display the variability of the calculated relative magnitude differences for stroke sizes of 20 mm, 30 mm, and 40 mm. The purpose of this analysis was to determine if the presence of a stroke in the head causes variability in the data, enabling the classification algorithm to accurately classify it into the iStroke, hStroke, and noStroke classes. The analysis was conducted for stroke diameters of 20, 30, and 40 mm. The relative magnitude differences, calculated using formula (3), were employed for the analysis.

2.8 Stroke classification

This chapter is based on the author's conference paper [114].

In general, there are various algorithms and machine learning techniques that can be used for stroke classification, including decision trees, random forests, support vector machines (SVMs), and deep learning methods such Deep Neural Networks (DNNs). DNNs require a large amount of training data to perform optimally. DNNs are therefore not suitable for the classification of strokes, as it is challenging to obtain a sufficient amount of training data for this task. Support Vector Machines (SVMs) were used in past for microwave stroke classification [82], [95], [110], [113]due to their strong performance in various classification tasks, including medical imaging analysis. In this study, we specifically focused on using SVMs [131], as they have been found to be the most appropriate method based on our previous research results reported in [59], [60], [113], [114].

2.8.1 Support Vector Machine algorithm

For the detection and classification of strokes, we employed a non-linear SVM with kernel functions [132]. Kernel functions map the data to higher dimensional space where the classes are easier to separate. For classification between ischemic, hemorrhagic and no stroke scenario we construct a three-class SVM classifier by combining multiple binary classifiers. The one vs all learning technique was used. The implementation of the algorithm used in this work is the one from MATLAB 2022a Statistics and Machine Learning Toolbox version 12.3. The aim was to classify the data into three different classes: iStroke, hStroke, and noStroke. Additionally, two-class SVM classifier was designed to differentiate ischemic stroke from other cases, including hemorrhagic stroke and a healthy head, which was labeled as the Other class. The aim was to verify whether the SVM classifier can provide safe information for initiating thrombotic therapy in ischemic stroke patients and avoid misclassification of hemorrhagic stroke patients as ischemic stroke patients. To this end, a cost matrix was created where the misclassification of a patient in the other class (i.e., primarily referring to hemorrhagic stroke patients) into the iStroke class was given a higher cost than the misclassification of a patient in the iStroke class into the Other class.

To train the multi-class algorithm, the *fitcecoc* function was used. This function takes as inputs the training data matrix (*TrainData*), the input matrix with the true classes (*TrainDataClass*), and the type of the classification algorithm (*Learner*). The training data matrix consisted of a pre-determined number of rows, with each row being filled with values that had been obtained after the adjustment of the S-matrix through normalization and dimensionality reduction using principal component analysis (PCA). The classification algorithm (*Learner*) was set up using the function *templateSVM*, which allowed for the definition of parameters such as kernel type, kernel scale, and box constraint. However, we optimized these parameters using hyperparameter optimization as defined in *fitcecoc* function. *Learner* allows for the definition of different machine learning algorithms, such as Logistics Regression (*templateKernel*), Discriminant Analysis (*templateDiscriminant*), Nearest Neighbors (*templateKNN*), Naïve Bayes classifier (*templateNaiveByes*), and Classification Tree (*templateTree*). This algorithm will be tested as well with hyperparameters optimization of his parameters.

For testing the learned classifier, a test data matrix (*TestData*) and a corresponding test data class matrix (*TestDataClass*) were created to assess the classification results. Additional information required for analysis, such as stroke size and position, phantom type and scale, used frequency, etc., was stored in a corresponding information matrix (*TestDataInfo*). This information matrix was utilized exclusively for the evaluation of classifications that were problematic. The selection of test and training data from datasets is performed using in-house written functions in MATLAB. The algorithm's performance testing is done using the *predict* function, where the input is the trained model and test data. The output of the function is the classification of data into classes.

2.8.2 Hyperparameters optimization

To enhance the algorithm's performance, we utilized the configuration of hyperparameters. However, the lack of information about their meaning and interconnection often makes it hard to select parameters correctly. Therefore, hyperparameter optimization tools were used. The optimization process was conducted using Bayesian optimization, which is a highly efficient global optimization method for machine learning models [133]. Bayesian optimization is more efficient in determining hyperparameters than the commonly used grid search or random search [134]. For each step of dimensionality reduction, 500 iterations of hyperparameter optimization were performed. The following parameters were optimized:

- **Kernel function:** The kernel function to map the input data into a higher-dimensional space, where it becomes easier to separate the data into classes. The choice of kernel function (e.g. linear, polynomial, radial basis function) can greatly affect the performance of the SVM model.
- **Penalty parameter** *C* (in MATLAB called **Box Constraint**): For large values of penalty parameter the SVM will prioritize classifying all the training data correctly which can lead to sacrificing the margin between the classes and overfitting - the resulting hyperplane may not generalize new data. For small values of penalty parameter, the SVM will prioritize maximizing the margin between the classes which can lead to misclassifying some training examples and underfitting - the resulting hyperplane may not

capture all the important patterns in the data. The goal of hyperparameter optimization is usually set to a value that balances the wide margin with the correct classification of most of the training data. Box Constraint takes values from 0.001 to 1000.

- **Gamma** (in MATLAB called **Kernel Scale**): This parameter controls the influence of individual training instances and create the shape of the decision boundary. A high gamma value results in a more complex decision boundary, providing a better fit for the training data. However, this may lead to overfitting, where the boundary fits the training data too closely and fails to generalize effectively to new data. On the other hand, a low gamma value provides a simpler decision boundary that may not perfectly fit the training data but is less susceptible to overfitting. Kernel scale takes values from 0.001 to 1000.

MATLAB 2022a Statistics and Machine Learning Toolbox version 12.3 is equipped with automatic hyperparameter optimization feature, which was used throughout this work. By using hyperparameter optimization the optimal values for these hyperparameters were determined for a given dataset, which should significantly improve the performance of the SVM model for stroke detection and classification.

2.8.3 Classification algorithm assessment

The use of a confusion matrix allows for the assessment of the performance of the classifier in terms of correctly and incorrectly classified samples, which can provide insight into which classes (stroke types) are problematic for the classification task. This information can be used to further optimize classifier setting and improve its performance.

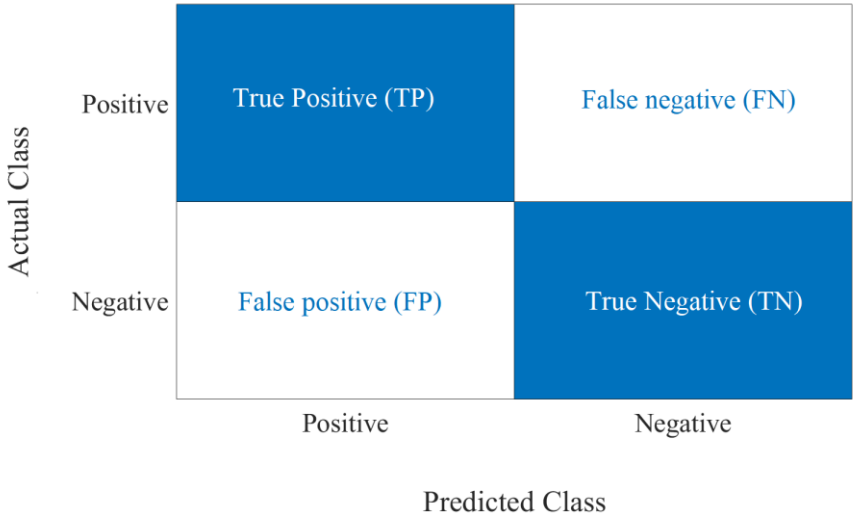

Figure 23: Confusion matrix

The accuracy of the classifier, which can be calculated from the confusion matrix, is a common metric used to quantify the performance of the classifier. The classification accuracy (CL-accuracy) is defined as the ratio of the number of correctly classified instances to the total number of instances in the dataset, expressed as:

$$CL\text{-}accuracy = \frac{correctly\ classified}{Total} = \frac{TP + TN}{TP + TN + FP + FN}\ . \tag{4}$$

While overall accuracy provides an estimate of the accuracy of the model, it does not account for imbalanced class distributions. To address this issue, Cohen's kappa [135] is a commonly used metric that provides a more objective evaluation of the performance of the model. Cohen's kappa compares the accuracy of the system to the accuracy of a random system and takes values from -1 to 1. If Cohen's kappa is negative, the overall accuracy of the model is lower than that of a random system. The formula for calculating Cohen's kappa is as follows:

$$\kappa = \frac{CL\text{-}accuracy - randomAccuracy}{1 - randomAccuracy}, \tag{5}$$

where the $randomAccuracy$ is defined as the sum of the product of the reference and result likelihood for each class. In terms of false positives etc., $randomAccuracy$ can be written as:

$$randomAccuracy = \frac{(TN + FP) \cdot (TN + FN) + (FN + TP) \cdot (FP + TP)}{Total \cdot Total} \quad (6)$$

In the two-class learner, the sensitivity and specificity of stroke classification was monitored. In this scenario, positive cases refer to patients diagnosed with ischemic stroke, while negative cases are comprised of patients with hemorrhagic stroke or who are healthy. The specificity is defined as:

$$Specificity = \frac{TN}{TN + FP}, \quad (7)$$

where true negatives (TN) refer to the cases that are correctly classified as negative, while false positives (FP) refer to cases that are incorrectly classified as positive. In the context of ischemic stroke classification, false positives refer to cases that are wrongly classified as ischemic stroke, but are actually hemorrhagic stroke or healthy patient. The sensitivity is defined as:

$$Senzitivity = \frac{TP}{TP + FN}, \quad (8)$$

where True Positives (TP) are the cases correctly classified as positive and False Negatives (FN) are the cases that are actual positive but classified as negative by the algorithm (see Figure 23). Our objective is to set the specificity such that there are no misclassifications of hemorrhagic stroke into the ischemic class, even if this comes at the cost of a lower sensitivity, i.e., a lower successful classification rate of ischemic patients. This approach is chosen based on the critical nature of administration of thrombotic therapy to ischemic patients. Misclassifying hemorrhagic stroke patients as ischemic could lead to the administration of thrombotic therapy to bleeding patients, which could be life-threatening. Therefore, it is crucial to set the specificity of the model such that hemorrhagic stroke patients are not misclassified as ischemic, even if it leads to a lower sensitivity and fewer successfully classified ischemic patients. The ability to track whether a hemorrhagic or healthy patient (classified as Other class) was not misclassified as ischemic is made possible by the information matrix of the test data (*TestDataInfo)*, which is compatible with the classification result in a backward manner.

The cross-validation error (CV-error) was calculated to evaluate the performance of the algorithms before classifying the training data. In k-fold cross-validation, the dataset is divided into k parts, with one part being used for testing and the remaining k-1 parts being used for training. The process is repeated so that each part is used for testing only once. In this work, k = 5 fold validation was utilized.

2.9 Scenario testing

This chapter is partially based on the author's article published in a journal with impact factor [116].

To systematically test the algorithms under different scenarios, training and testing datasets were created from the complete numerical simulation and experimental measurement datasets. The process of selecting the training and testing datasets was performed using in-house written functions in MATLAB. The information regarding the dataset utilized for each testing scenarios is presented in the summary tables.

2.9.1 2D numerical simulations

Data corresponding to patients with small ischemic and hemorrhagic stroke sizes show the smallest deviation from data for healthy subjects. It can be expected that they represent the worst case for classification and therefore may be the most relevant for determining support vectors. We trained the SVM algorithm with datasets including successively only 20, then 30, and finally, 40 mm iStrokes and hStrokes placed at 20 positions in 10 randomly scaled models (in total, 600 for each stroke type for testing). The SVM algorithm classified the remaining data. Dimensionality reduction using PCA was not used in this case. For simplification, only data for 1 GHz were used. The data used for training and testing algorithm in scenario S1 are described in Table 7.

Table 7. Description of the training and testing data parameters for testing scenario S1

	TrainData	**TestData**
DataSet (−)	2D_1	2D_1
Stroke type (−)	hStroke, iStroke, noStroke	hStroke, iStroke, noStroke
Stroke sizes (mm)	20 or 30 or 40	20, 25, 30, 35, 40
Stroke positions (−)	Fixed 20	Fixed 20

Head models (−)	10 scaled	10 scaled
Frequency points (−)	1	1
DataSet size† **(−)**	600	3000
DataSet dimensions ‡ **(−)**	110	110

† The single measured S-matrices, ‡ The number of S-parameters from S-matrix.

For a smaller number of frequency points, the algorithm works with a smaller amount of data. On the other hand, for a higher number of frequency points, we can reduce the dimensionality to only useful information. Classification results were compared for the SVM algorithm trained on data for a single frequency point (1 GHz), five frequency points (from 0.8 GHz, step 0.1 GHz, to 1.2 GHz), fifteen frequency points (from 0.8 GHz, 0.05 GHz step, up to 1.5 GHz) data and twenty-five frequency points (from 0.8 GHz, 0.05 GHz step, up to 2 GHz) data. We train the SVM algorithm for 20 mm iStroke and hStroke sizes located at 20 positions in 10 random scaled models. The SVM algorithm classified the remaining data. The data used for training and testing algorithm in scenario S2 are described in Table 8.

Table 8. Description of the training and testing data parameters for testing scenario S2.

	TrainData	**TestData**
DataSet (−)	2D_1	2D_1
Stroke type (−)	hStroke, iStroke, noStroke	hStroke, iStroke, noStroke
Stroke sizes (mm)	20	20, 25, 30, 35, 40
Stroke positions (−)	Fixed 20	Fixed 20
Head models (−)	10 scaled	10 scaled
Frequency points (−)	1 or 5 or 15 or 25	1
DataSet size† **(−)**	600	3000
DataSet dimensions‡ **(−)**	110 or 550 or 1650 or 2750	110 or 550 or 1650 or 2750

† The single measured S-matrices, ‡ The number of S-parameters from S-matrix.

For testing scenario S3 we trained the SVM algorithm using data on subjects with 20 mm iStroke and hStroke located at 20 positions in 10 randomly scaled head models. We used training data for a frequency of 1 GHz and 90 dimensions reduced by PCA. The SVM algorithm classified the data of subjects with random stroke sizes. The data used for training and testing algorithm in scenario S3 are described in Table 9.

Table 9. Description of the training and testing data parameters for testing scenario S3.

	TrainData	**TestData**
DataSet (−)	2D_1	2D_2
Stroke type (−)	hStroke, iStroke, noStroke	hStroke, iStroke, noStroke
Stroke sizes (mm)	20	20–40
Stroke positions (−)	Fixed 20	Fixed 20
Head models (−)	10 scaled	10 scaled
Frequency points (−)	1	1
DataSet size† **(−)**	600	600
DataSet dimensions‡ **(−)**	90	90

† The single measured S-matrices, ‡ The number of S-parameters from S-matrix.

For testing scenario S4 we trained the SVM algorithm using data for 20 mm iStroke and hStroke sizes located at 20, 83, and 456 positions in 10 randomly scaled head models. We used training data for a frequency of 1 GHz and 90 dimensions reduced by PCA. The SVM algorithm classified data for random stroke sizes and random stroke positions. The data used for training and testing algorithm in scenario S4 are described in Table 10.

Table 10. Description of the training and testing data parameters for testing scenario S4.

	TrainData	**TestData**
DataSet (−)	2D_1	2D_3
Stroke type (−)	hStroke, iStroke, noStroke	hStroke, iStroke, noStroke
Stroke sizes (mm)	20	20–40
Stroke positions (−)	Fixed 20 or 83 or 456	Random 20
Head models (−)	10 scaled	10 scaled
Frequency points (−)	1	1
DataSet size† **(−)**	600 or 2490 or 1368	600
DataSet dimensions‡ **(−)**	90	90

†The single measured S-matrices, ‡ The number of S-parameters from S-matrix.

For testing scenario S5 we trained the SVM algorithm using data for 20, 30 and 40 mm iStroke and hStroke sizes located at 20 positions in 10 randomly scaled head models. We used training data for a frequency of 1 GHz. Dimensionality reduction was performed by PCA to find the best result for each algorithm. The SVM algorithm classified data for random stroke sizes and random stroke positions. The data used for training and testing are described in Table 11.

Table 11. Description of the training and testing data parameters for testing scenario S5.

	TrainData	**TestData**
DataSet (−)	2D_1	2D_3
Stroke type (−)	hStroke, iStroke, noStroke	hStroke, iStroke, noStroke
Stroke sizes (mm)	20, 30, 40	20–40
Stroke positions (−)	Fixed 20	Random 20
Head models (−)	10 scaled	10 scaled
Frequency points (−)	1	1
DataSet size† **(−)**	600	600
DataSet dimensions‡ **(−)**	110	110

†The single measured S-matrices, ‡The number of S-parameters from S-matrix.

2.9.2 3D numerical simulation

For testing scenario S6 the SVM algorithm was trained using data for 20 mm iStroke and hStroke sizes located at 20 predefined positions for 3D numerical simulation. Based on previous results, we used training data for a frequency of 1 GHz and gradually increased the data dimension to find the dimension with the highest classification accuracy. The SVM algorithm classified data for 20, 30 and 40 mm iStroke and hStroke sizes located at 20 predefined positions. The data used for training and testing algorithm in scenario S6 are described in the Table 12.

Table 12: Description of the training and testing data parameters for testing scenario S6 – 3D numerical simulations.

	TrainData	**TestData**
DataSet (-)	3D_1	3D_1
Stroke type (-)	hStroke, iStroke, noStroke	hStroke, iStroke, noStroke
Stroke sizes (mm)	20	20, 30, 40
Stroke positions (-)	Fixed 7	Fixed 7
Head models (-)	10	10
Frequency points (-)	1	1
DatSet size[†] (-)	70+70+70	210+210+70
DataSet dimensions[‡] (-)	110	110

[†]The single measured S-matrices, [‡]The number of S-parameters from S-matrix.

For testing scenario S7, we utilized the training and testing datasets from test scenario S6, but the TrainData and TestData were formatted to include two formats. The first format was the original format of real and imaginary parts, while the second format involved modulus and phases. The dataset dimensionality was gradually increased using PCA, and the dimension with the highest classification accuracy was determined.

For testing scenario S8, we used the training and test datasets from test scenario S6 in the data format specified by test scenario S8. However, the TrainData and TestData were formatted to include only the transmission parameters of the S-matrix and compared to the original data format that contained both reflection and transmission parameters of the matrix. The dataset dimensionality was gradually increased using PCA, and the dimension with the highest classification accuracy was determined.

Around 85% of strokes are ischemic [3], therefore, the SVM algorithm should have a higher success rate than the statistical probability. For testing scenario S9 the SVM algorithm was trained using data for 20 mm iStroke and hStroke sizes located at 20 predefined positions for 3D numerical simulation. We used training data for a frequency of 1 GHz and gradually increased the data dimension to find the dimension with the highest classification accuracy. The SVM algorithm classified data for random stroke sizes and random stroke positions. The data used for training and testing are described in the Table 13.

Table 13: Description of the training and testing data parameters for testing scenario S9 – 3D numerical simulations.

	TrainData	**TestData**
DataSet (-)	3D_2	3D_3
Stroke type (-)	hStroke, iStroke, noStroke	hStroke, iStroke, noStroke
Stroke sizes (mm)	20	20 - 40
Stroke positions (-)	Fixed 20	Random 20
Head models (-)	10	10
Frequency points (-)	1	1
DatSet size[†] (-)	200+200+200	100+100+100
DataSet dimensions[‡] (-)	110	110

[†]The single measured S-matrices, [‡]The number of S-parameters from S-matrix.

Testing scenario H10 utilized the same data as test scenario S9 for training and testing the algorithm (see Table 13). In this case, the hStroke and noStroke scenarios were merged into a single class labeled 'Other' This step enabled the use of a two-class learner SVM algorithm. The dataset dimensionality was gradually increased using PCA, and the dimension with the highest classification accuracy was determined.

2.9.3 Measurements

For testing scenario S11 the SVM algorithm was trained using data for 20 mm iStroke and hStroke sizes located at 20 predefined positions for and experimental measurement with liquid head phantom and for realistic head phantom. Based on previous results, we used training data for a frequency of 1 GHz and gradually increased the data dimension to find the dimension with the highest classification accuracy. The SVM algorithm classified data for 20, 30 and 40 mm iStroke and hStroke sizes located at 20 predefined positions. The data used for training and testing algorithm in scenario S11 are described in the Table 14 and Table 15.

Table 14: Description of the training and testing data parameters for testing scenario S11 – experimental measurements with liquid phantom.

	TrainData	**TestData**
DataSet (-)	M_1	M_1
Stroke type (-)	hStroke, iStroke, noStroke	hStroke, iStroke, noStroke
Stroke sizes (mm)	20	20, 30, 40
Stroke positions (-)	Fixed 20	Fixed 20
Head phantoms (-)	1	1
Frequency points (-)	1	1
DatSet size[†] (-)	20+20+20	60 + 60 +20
DataSet dimensions[‡] (-)	110	110

[†]The single measured S-matrices, [‡]The number of S-parameters from S-matrix.

Table 15: Description of the training and testing data parameters for testing scenario S11 – experimental measurements with realistic phantom.

	TrainData	**TestData**
DataSet (-)	M_3	M_3
Stroke type (-)	hStroke, iStroke, noStroke	hStroke, iStroke, noStroke
Stroke sizes (mm)	20	20, 30, 40
Stroke positions (-)	Fixed 20	Fixed 20
Head phantoms (-)	1	1
Frequency points (-)	1	1
DatSet size[†] (-)	20+20+20	60 + 60 +20
DataSet dimensions[‡] (-)	110	110

[†]The single measured S-matrices, [‡]The number of S-parameters from S-matrix.

For testing scenario S12 the SVM algorithm was trained using data for 20, 30 and 40 mm iStroke and hStroke sizes located at 20 predefined positions for and experimental measurement with liquid head phantom and for realistic head phantom. We used training data for a frequency of 1 GHz and PCA reduced the data dimensions based on the results of the previous testing scenarios. The SVM algorithm classified data for random stroke sizes and random stroke positions. The data used for training and testing are described in the Table 16 and Table 17.

Table 16: Description of the training and testing data parameters for testing scenario S12 – experimental measurements with liquid phantom.

	TrainData	**TestData**
DataSet (-)	M_1	M_2
Stroke type (-)	hStroke, iStroke, noStroke	hStroke, iStroke, noStroke
Stroke sizes (mm)	20, 30, 40	20, 30, 40
Stroke positions (-)	Fixed 20	Random 20
Head phantoms (-)	1	1
Frequency points (-)	1	1
DatSet size[†] (-)	20+20+20	60 + 60 +20
DataSet dimensions[‡] (-)	110	110

[†]The single measured S-matrices, [‡]The number of S-parameters from S-matrix.

Table 17: Description of the training and testing data parameters for testing scenario S12 – experimental measurements with realistic phantom.

	TrainData	**TestData**
DataSet (-)	M_3	M_4
Stroke type (-)	hStroke, iStroke, noStroke	hStroke, iStroke, noStroke
Stroke sizes (mm)	20, 30, 40	20, 30, 40
Stroke positions (-)	Fixed 20	Random 20
Head phantoms (-)	1	1
Frequency points (-)	1	1
DatSet size[†] (-)	20+20+20	60 + 60 +20
DataSet dimensions[‡] (-)	110	110

[†]The single measured S-matrices, [‡]The number of S-parameters from S-matrix.

Testing scenario S13 utilized the same data as test scenario S12 for training and testing the algorithm (see Table 16 and Table 17). In this case, the hStroke and noStroke scenarios were merged into a single class labeled Other class. This step enabled the use of a two-class learner SVM algorithm. The dataset dimensionality was gradually increased using PCA, and the dimension with the highest classification accuracy was determined.

3. Results

In this study, we systematically tested the capabilities of SVM-based machine learning algorithms in detecting and classifying strokes. Large datasets from both 2D and 3D numerical simulations and experimental measurements were generated, and 13 scenarios were tested on these datasets. The datasets have been or will be made available to the scientific community for further algorithm development and testing. Additionally, ten 5-layer 2D and 3D numerical models of human head were created to generate datasets, which can be utilized in other applications, such as microwave hyperthermia treatment. Further, the computer-controlled stroke positioning system was developed to enable repeatable and reproducible microwave measurements, in conjunction with developed stroke phantoms and a 3D anatomically and dielectrically realistic phantom of an adult human head.

3.1 2D and 3D numerical models

The chapter is based on the author's article [116] published in an journal with an impact factor.

The geometry of one 2D numerical model is depicted in Figure 24. A total of 10 numerical models for different human head models were created. The 2D geometries of all 10 head models are shown in Appendix A.

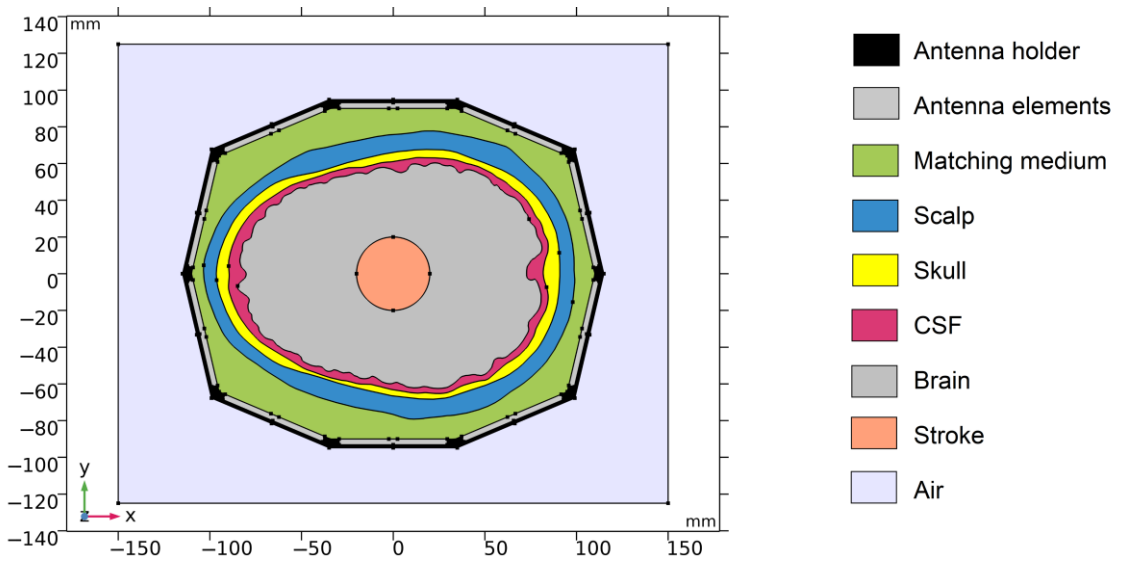

Figure 24. Geometry of the 2D numerical model. Antenna holder and antenna elements surrounding a realistic human head model. XY-plane corresponds to the cross-section at z = 100 mm of the laboratory prototype 3D numerical model (corresponds to the plane of the antenna elements).

The geometry of one 3D numerical model is depicted in Figure 25. A total of 10 numerical models for different human head models were created. The 3D geometries of all 10 head models are shown in Appendix B.

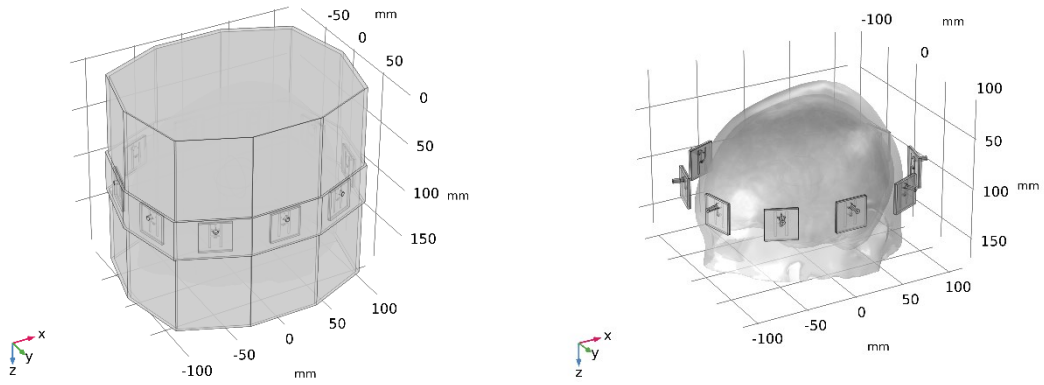

(a) (b)

Figure 25. The geometry of the 3D numerical model of the experimental microwave system. The model geometry with air region hidden (a), with container and matching liquid areas hidden (b).

3.2 Numerical models validation

The chapter is based on the author's article [116] published in a journal with impact factor.

Numerical model validation was done by direct comparison of measured S-parameters from laboratory prototype of the microwave imaging system and S-parameters from 2D and 3D numerical simulations (see Figure 26). The 3D numerical model of the microwave system yields a more accurate fit of the reflection and transmission parameters to experimental measurements than the simplified 2D numerical model.

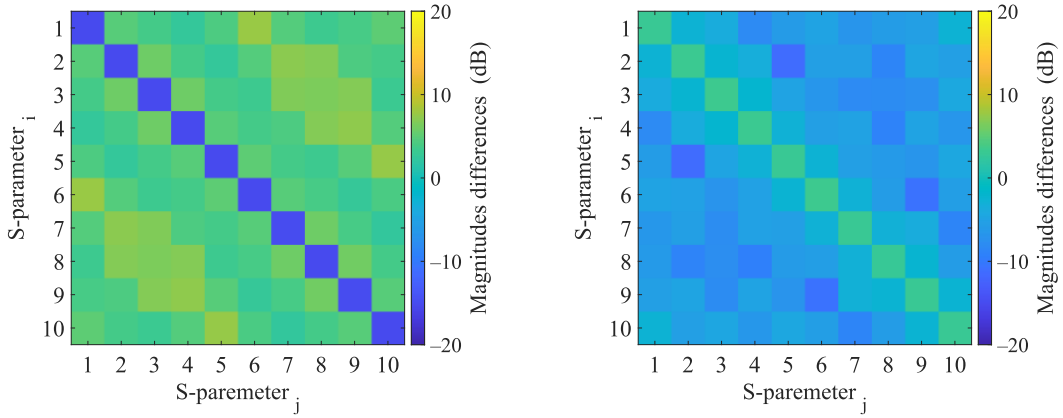

Figure 26. Magnitudes differences of 2D numerical model and 3D numerical model (a) and magnitudes differences of 3D numerical model and experimental measurement (b), calculated using formula (2).

The results of the analysis of changes in S-parameters resulting from the presence of a stroke are presented in Appendix C for both the 2D and 3D numerical models and the experimental system. No significant changes in the reflection coefficients were observed for magnitudes differences (in dB) when the stroke was inserted. However variations in the transmission coefficients were noted and were found to be distinct for ischemic and hemorrhagic strokes, making them useful for the intended purpose. The results indicate that changes in the transmission coefficients are more pronounced in the 2D model than in the 3D model. The experimental measurements of ischemic stroke correlate well with the 3D numerical simulation. However, the experimental measurements of hemorrhagic stroke show higher changes in the S-matrix compared to the 3D numerical simulation. Furthermore, for both the 2D and 3D numerical simulations and experimental measurements, changing the position of the stroke results in changes in the same S-parameters.

3.3 Head and stroke phantoms

The chapter is partly based on the author's article published in a journal with impact factor [126] and conference paper [125].

New molds for the production of phantoms were created using a 3D printer. These molds provide more precise control over the positioning of individual layers in the x, y, and z directions than molds presented in [126]. Figure 27 shows the individual components of the molds.

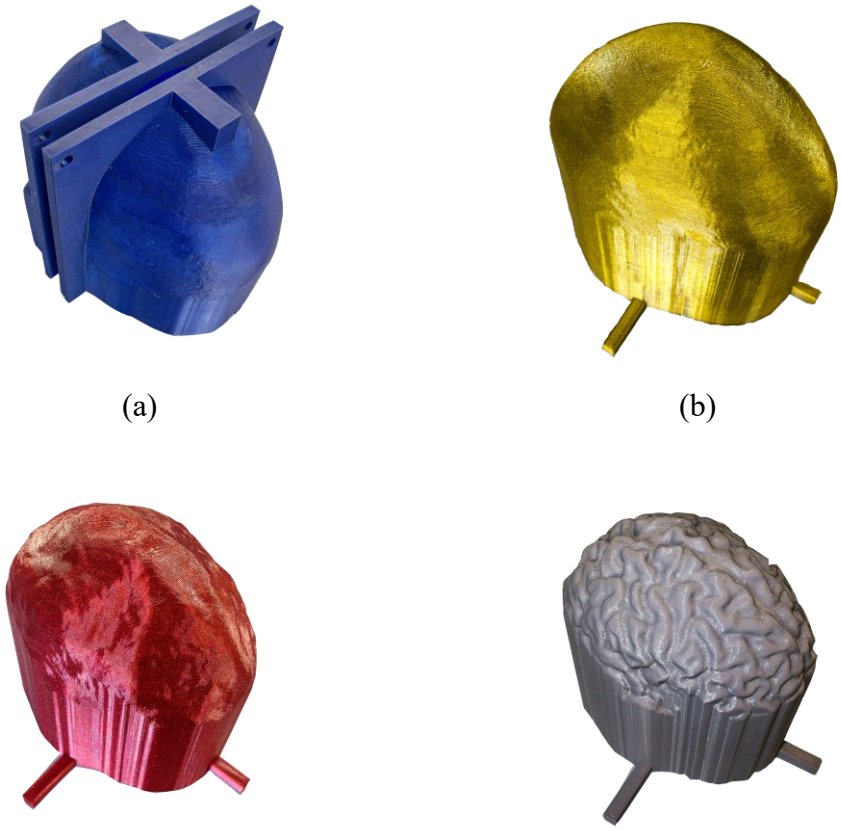

(a) (b)

(c) (d)

Figure 27. 3D printed molds for multilayer human head phantom fabrication. (a) scalp mold, (b) skull mold, (c) cerebrospinal fluid mold, and (d) brain mold.

Table 18: Head phantom and stroke phantoms materials weight percentages.

Tissue layer	Urethane rubber† (%)	Graphite powder (%)	Carbon Black Powder (%)	Acetone (%)
Scalp	66.0	22.7	2.3	9.0
Skull	88.0	10.0	2.0	0
CSF	44.0	36.0	0	20
Hemorrhagic stroke	61.5	22.0	3.5	13.0
Ischemic stroke	66.0	22.7	2.3	9.0
Liquid Brain	61.15 % deionized water + 38 % isopropanol + 0.85 % NaCl			

The 3D phantom produced in this study is anatomically and dielectrically realistic, as depicted in Figure 28. It was designed to mimic the human head, with anatomical features such as the scalp, skull, cerebrospinal fluid, and brain tissue. The ratios of the mixtures that make up the head phantom are listed in Table 18. The dielectric properties of the human head phantom and target dielectric properties from the IT'IS Foundation database [33] are listed in Table 19.

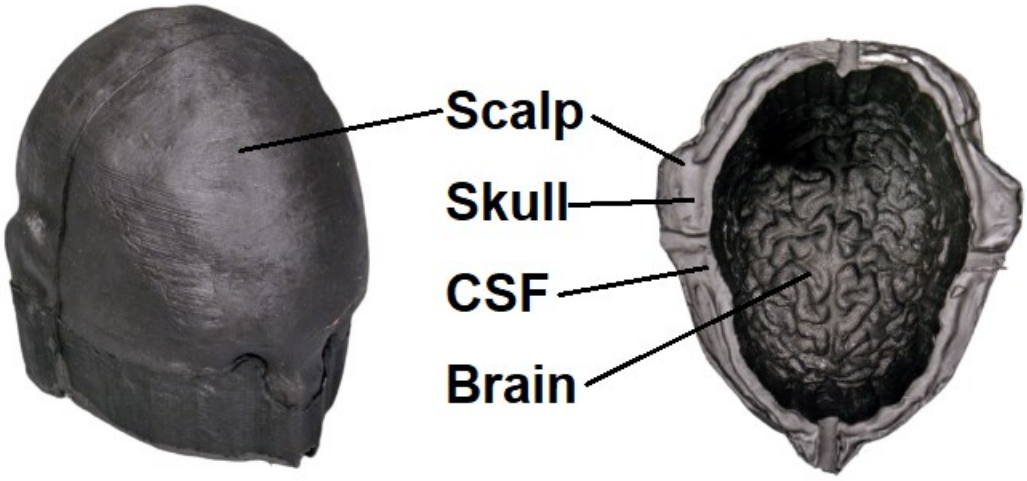

Figure 28. Photograph of the anatomically and dielectrically realistic 3D human head phantom: external solid layers corresponding to scalp, skull, and CSF and forming waterproof container, which is filled with a liquid brain phantom during the measurements. This concept allows the physical stroke model to be inserted at different positions.

Table 19. Dielectric properties at 1 GHz of the different tissue-equivalent layers of the human head phantom. The measured data are supplemented with extended uncertainty (k = 2).

Tissue layer	**ε_r (-) human**	**ε_r (-) measured**	**σ (S/m) human**	**σ (S/m) measured**
Scalp	35.68	31.58 ± 4.54	0.66	0.84 ± 0.20
Skull	12.34	12.29 ± 0.26	0.16	0.19 ± 0.01
CSF	68.44	79.99 ± 13.99	2.46	3.75 ± 0.41
Liquid brain	40.00	41.40 ± 0.71	1.00	1.04 ± 0.01

The human head phantom complements a computer-controlled stroke positioning system (see Figure 29) with stroke phantoms of size 20, 30, and 40 mm in diameter that mimic ischemic and hemorrhagic strokes (see Figure 30). The dielectric properties of the stroke phantoms and target dielectric properties from the database are listed in Table 20.

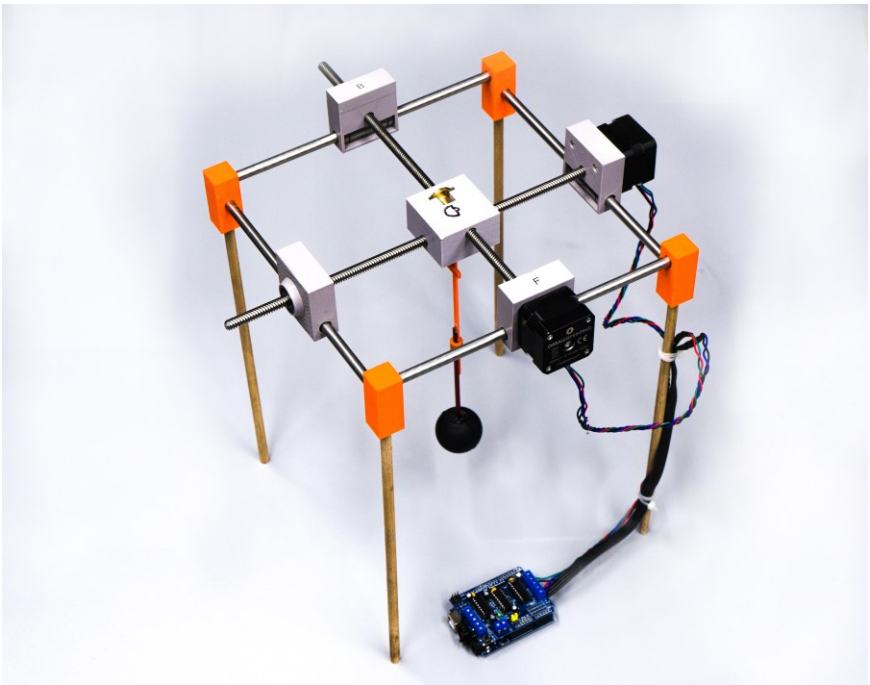

Figure 29. Computer-controlled stroke positioning system allowing sequential measurement of S-parameters for multiple stroke positions in a head phantom.

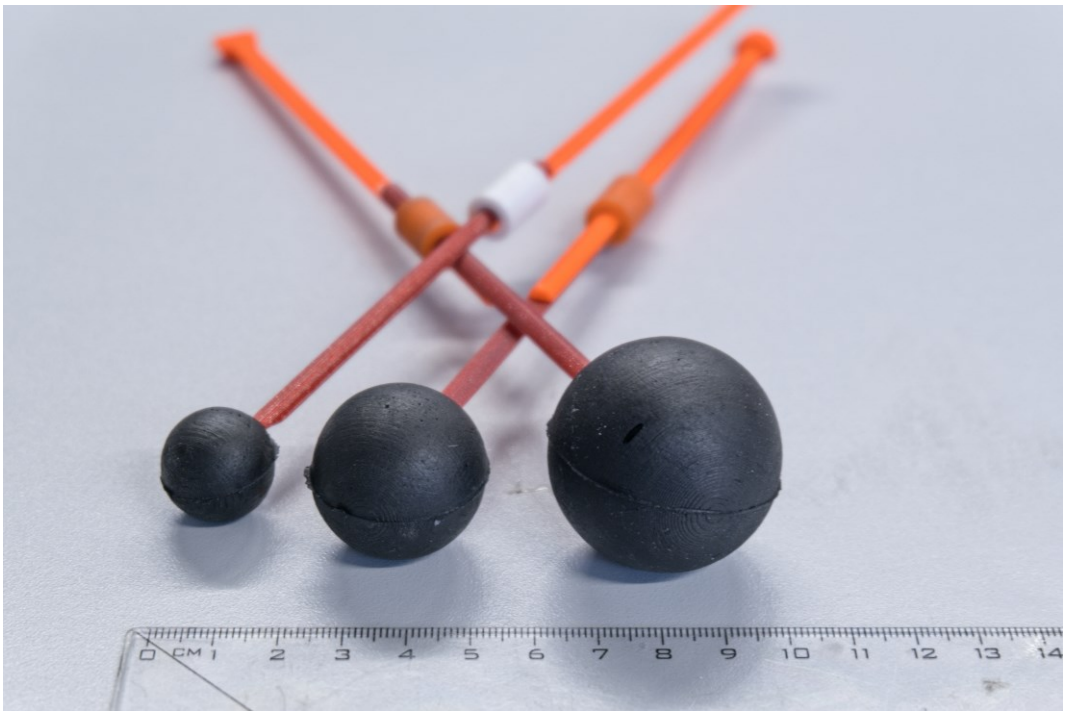

Figure 30: Stroke spherical phantoms with diameters 20, 30 and 40 mm.

Table 20: Dielectric properties of the stroke domain in the human head modes at a frequency of 1 GHz. Measured data are supplemented with extended uncertainty (k = 2).

Tissue layer	**ε_r (-) human**	**ε_r (-) measured**	**σ (S/m) human**	**σ (S/m) measured**
Ischemic stroke	34.00	31.72 ± 4.43	0.85	0.92 ± 0.07
Hemorrhagic stroke	61.07	52.73 ± 7.39	1.58	2.85 ± 0.58

3.4 Data variability and noise

Figure 31 compares the relative magnitude differences caused by the presence of stroke in the 3D numerical simulation dataset. To eliminate the variability caused by different head shapes, the data for one head model were compared. Boxplots were used to present the variability of the data for iStroke and hStroke. The data variability was characterized by the relative magnitude differences, calculated according to formula (3), between the S-matrices with and without strokes.

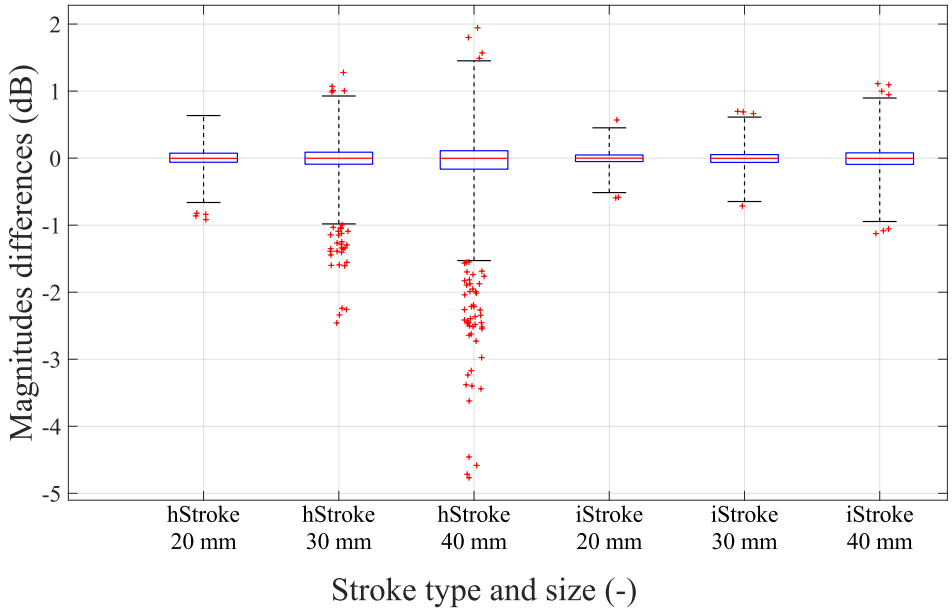

Figure 31. The relative magnitude differences caused by the presence of strokes with diameters of 20, 30, and 40 mm calculated using 3D numerical simulation dataset for a single head phantom. The bottom and top of each blue box represent the 25th and 75th percentiles of the sample, respectively. The red line in the middle of each box is the median. The black lines represent the data outside the box that lies in 5 times the box. The data marked with red stars are outlier values.

To determine the noise in the experimental measurements, the homogenous liquid head phantom without the stroke phantom was repeatedly measured for 7 hours. The S-matrices for the MW system were measured between stroke measurements, with three measurements taken at approximately one-hour intervals and a time interval of 10 minutes between measurements. Figure 32 shows the relative magnitude differences between the first antenna and all other antennas. The results indicate that the transmission parameters can for your experimental setup change by up to ±0.7 dB (f = 1 GHz, IF bandwidth = 10 Hz).

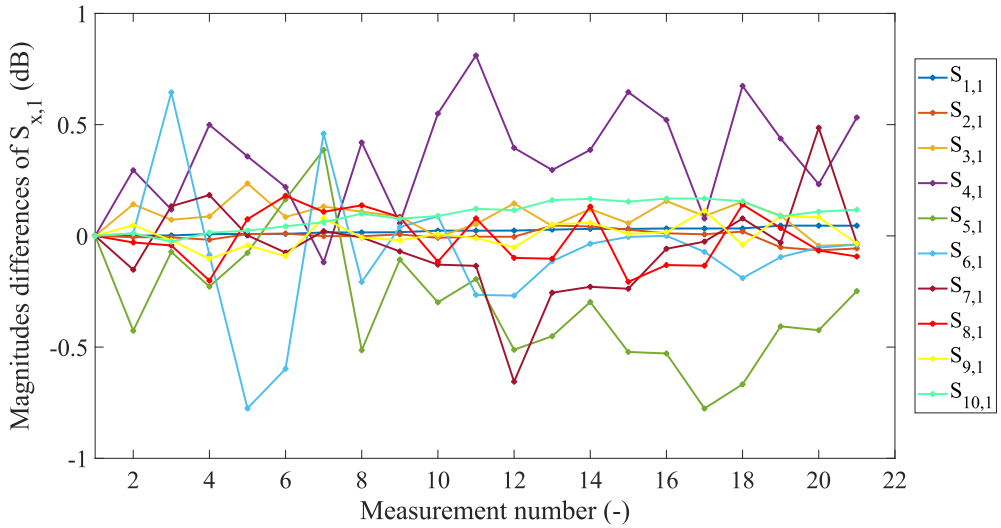

Figure 32. The relative magnitude differences of S-parameter in repeated experimental measurements of a homogeneous liquid head phantom without the stroke phantom.

3.5 Principal component analysis

During the PCA analysis, we examined the variances of the principal components in the 3D numerical simulation for two different data formats. The measurement data exhibited higher variance than the data from numerical simulations. Figure 33 displays the variances for all principal components.

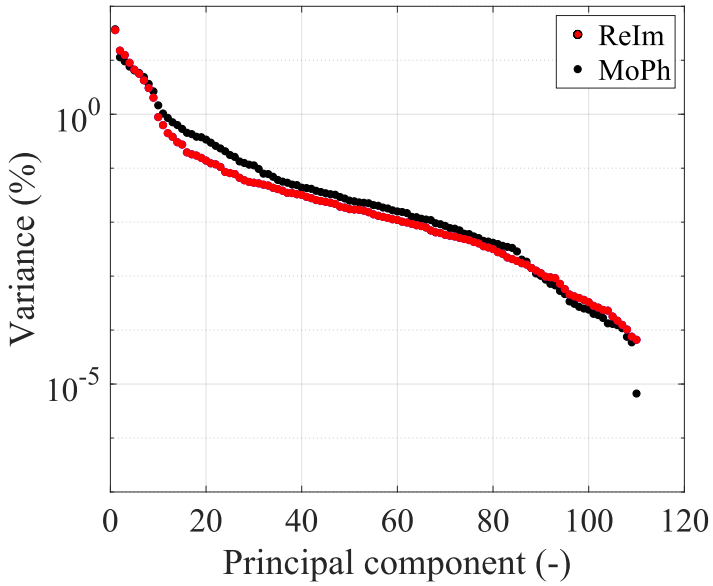

Figure 33. The variances of the principal components for 3D numerical simulation. Two different data formats were taken into account: real and imaginary part (ReIm) and module and phase (MoPh).

As part of the PCA analysis, we visualized the first three principal components of the 3D numerical simulation data in 3D space (see Figure 34). For the data represented in real and imaginary part format, the plotted points exhibited well-defined clusters that enabled better separation of iStroke, hStroke, and noStroke data compared to the data in the modulus and phase format, where the points appeared to be blended more into each other.

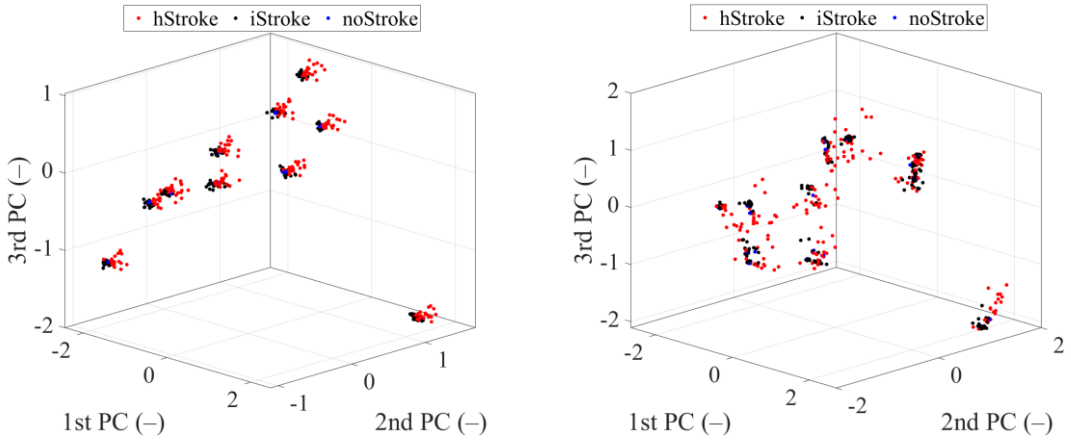

Figure 34. Visualization of the first three principal components (PCs) in three-dimensional space is presented for both the real and imaginary component data format (a), as well as for the module and phase data format (b) for 3D numerical data.

3.6 Scenario testing

This chapter is partially based on the author's article published in a journal with impact factor [116].

3.6.1 2D numerical simulations

SVMs were successively trained with data for different stroke sizes and then classified the remaining strokes (Training and testing data are described in Table 7). By training the algorithm with data corresponding to the smallest considered stroke sizes (with a diameter of 20 mm), the highest classification accuracy was achieved (see Table 21), even when classifying strokes up to the maximum considered diameter (40 mm).

Table 21. Effect of stroke sizes on classification accuracy – results for testing scenario S1.

Stroke Size (mm)	CV-Error (%)	CL-Accuracy (%)
20	11.8	95.7
30	7.0	85.3
40	5.5	65.5

Graphs of classification accuracy and cross-validation error for different values of dimensionality and different numbers of frequency points are in Appendix B. From Table 22, we conclude that for SVM training, it turns out to be most appropriate to use 1 or 5 frequency points, where the classification accuracy and cross-validation error were almost identical. For 15 and 25 frequency points the results are significantly worse and only after dimensionality reduction using PCA do the results reach similar classification accuracy as with a lower number of frequency points.

Table 22. The effect of number of frequency points and dimensionality reduction on the classification accuracy – results for testing scenario S2.

Frequency Points (−)	Frequencies (GHz)	Total Dimensions (−)	CL-Accuracy CV-Error (%)	Reduced Dimensions (−)	CL-Accuracy CV-Error (%)
1	1.00	110	94.6 14.9	90	96.9 10.4
5	0.80 1.00 1.20 1.40 1.50	550	77.0 17.3	80	96.8 10.2
15	0.80–1.50 step 0.05	1650	87.2 21.1	70	96.3 11.1
25	0.80–2.00 step 0.05	2750	33.3 28.6	150	92.2 8.4

The confusion matrix in Figure 35 shows that the classification between the iStroke and the hStroke class was accurate, only 6.5% of strokes were classified as the noStroke class, and 6.0% noStrokes were classified as the iStroke class.

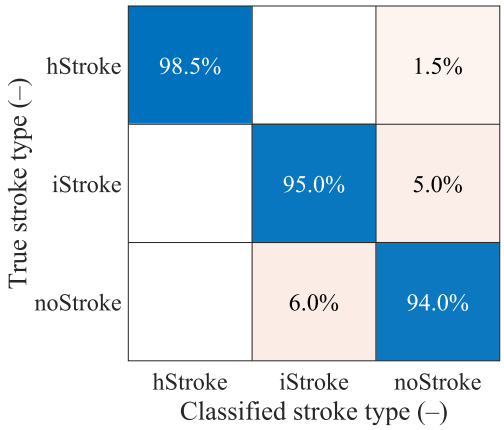

Figure 35. The confusion matrix for the classification of random ischemic and hemorrhagic stroke sizes.

From Table 23 we see that even for a larger amount of data, the algorithm cannot classify random data accurately and reach a maximum at around 70% classification accuracy. From the confusion matrixes in Figure 36, we can observe the correct and incorrect classification of iStroke, hStroke, and noStroke classes.

Table 23. The SVM algorithm classification of random stroke sizes and random stroke positions with different amounts of training data (different number of 20 mm stroke positions in the head).

Training Data Stroke Positions (–)	**Training Data Number of Models (–)**	**CV-Error (%)**	**CL-Accuracy (%)**	**Hyperparameters Optimalization Settings (–)**
20 hStroke 20 iStroke	10	11.3	64.3	Box Constraint = 912.92 Kernel = Gaussian Kernel Scale = 17.8
83 hStroke 83 iStroke	10	8.9	70.5	Box Constraint = 212.97 Kernel = Gaussian Kernel Scale = 11.41
456 hStroke 456 iStroke	1 randomly selected from 10 models	11.3	70.2	Box Constraint = 385.03 Kernel = Gaussian Kernel Scale = 19.74

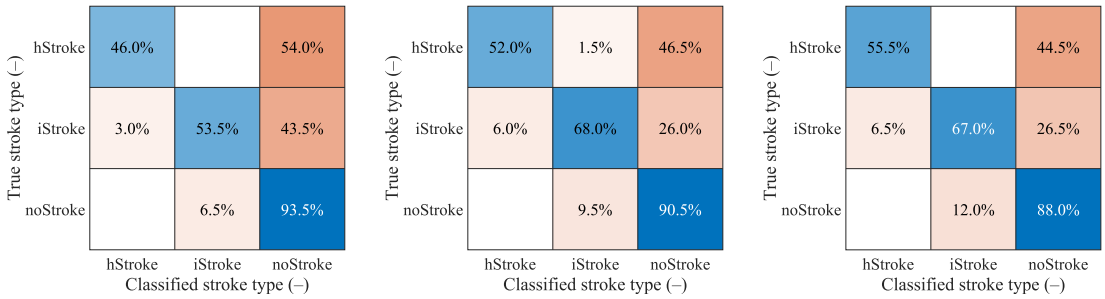

(a) (b) (c)

Figure 36. The confusion matrixes for classification of random stroke sizes and random stroke positions. In total, 200 samples for iStroke, 200 samples for hStroke and 200 samples for noStroke. SVM algorithm was trained for (a) 20 and (b) 83 ischemic and hemorrhagic strokes in 10 scaled models and (c) for 456 ischemic and hemorrhagic strokes in 1 randomly selected model from 10 scaled models.

The testing of six machine learning algorithms for detecting and classifying stroke types is presented in Table 24. We tested Support Vector Machine (SVM), Logistic Regression (LR), Discriminant Analysis (DA), k-Nearest Neighbors (kNN), Naive Bayes Classifier (NB), and Classification Tree (CTr) algorithms. The SVM algorithm demonstrated the best performance. Other algorithms have classification accuracy that was close to random estimation, indicated by their low kappa value. Negative kappa values were not presented.

Table 24. Results for classification of random stroke sizes and random stroke positions by different machine learning algorithms.

Algorithm (-)	**Reduced dimensions (-)**	**CL-error (%)**	**CL-accuracy (%)**	**Kappa (-)**
SVM	90	7.0	67.8	0.28
LR	90	-	55.7	0.01
DA	90	5.2	36.3	-
kNN	90	19.4	56.3	0.02
NB	40	-	38.7	-
CTr	50	25.7	43.8	-

3.6.2 3D numerical simulations

To verify the generalization ability of the SVM algorithm, we utilized data from 3D numerical simulations with a frequency of 1 GHz and gradually reduced the dimensions using PCA. The graph depicting the progress of dimensionality reduction (see Figure 37) indicates that 100% classification accuracy was achieved for 40 dimensions.

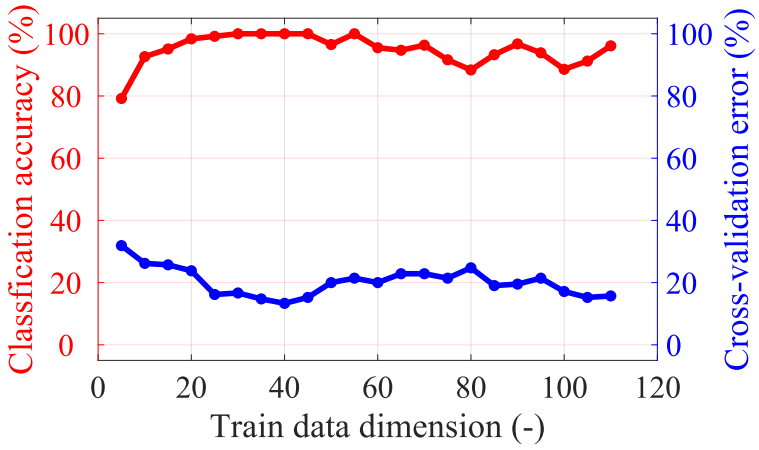

Figure 37. Dimensionality reduction graph for verifying the generalization ability of the SVM algorithm – testing scenario S6.

Table 25 shows that for the data in the real and imaginary format, the classification accuracy is already higher without dimensionality reduction then data in module and phase format. After reducing the dimensionality to 40, the SVM algorithm achieved 100% classification accuracy. For data in the module and phase format, the best result was obtained for a higher number of dimensions (75), but the algorithm achieved only 94.9% classification accuracy. A better classification result for the data in the real and imaginary format was also indicated by the variance of the principal components in Figure 34.

Table 25. Result for test scenario S7 - comparison of classification for real-imaginary part (ReIm) and module-phase (MoPh) format data.

Data form (-)	**Total dimensions (-)**	**CL-accuracy CV-error (%)**	**Reduced dimensions (-)**	**CL-accuracy CV-error (%)**
ReIm	110	96.1 15.7	40	100.0 13.3
MoPh	110	92.7 25.2	75	94.9 34.3

In test scenario S8, we evaluated the performance of the SVM algorithm for two different S-parameter data sets: the former includes both transmission and reflection coefficients (TrRe) with 110 dimensions, and the latter includes transmission coefficients (Tr) only with 90 dimensions. The comparison was performed also for reduced dimensionality using PCA. The SVM for TrRe data shows a higher success rate for both original and reduced dimensionality. Dimensionality 40 gives the best results for both datasets – TrRe and Tr. For TrRe the classification accuracy reached 100%, while for Tr the classification accuracy closely approached 100%. The big difference is in the cross-validation error, which is half the size of the original as well as the reduced size of TrRe (see Table 26).

Table 26. The result of test scenario S8 - comparison of SVM performance for datasets including transmission and reflection (TrRe) and transmission coefficients (Tr) only.

Data form (-)	**CL-accuracy CV-error (%)**	**Reduced dimensions (-)**	**CL-accuracy CV-error (%)**
TrRe (110 dimensions)	96.1 15.7	40	100.0 13.3
Tr (90 dimensions)	87.8 29.0	40	99.38 26.7

The classification results for test scenario 9 are shown in Table 27. We conclude that for randomly placed stroke models, the SVM algorithm is capable of classifying stroke types with 86.3% accuracy. From the confusion matrix presented in Figure 38, it is evident that misclassifications occur most frequently for the noStroke scenario. However, misclassifications in other classes were observed too. It is worth noting that 2% of hStroke were classified as iStroke scenario.

Table 27. Results for testing scenario S9 – classification classifying randomly sized strokes at random positions for 3D numerical simulations datasets.

Data form (-)	**Total dimensions (-)**	**Reduced dimensions (-)**	**CL-accuracy (%)**	**Kappa (-)**	**Hyperparameters Optimalization Settings (-)**
ReIm	110	20	86.3	0.69	Box Constraint = 267.6 Kernel = Gaussian Kernel Scale = 20.6

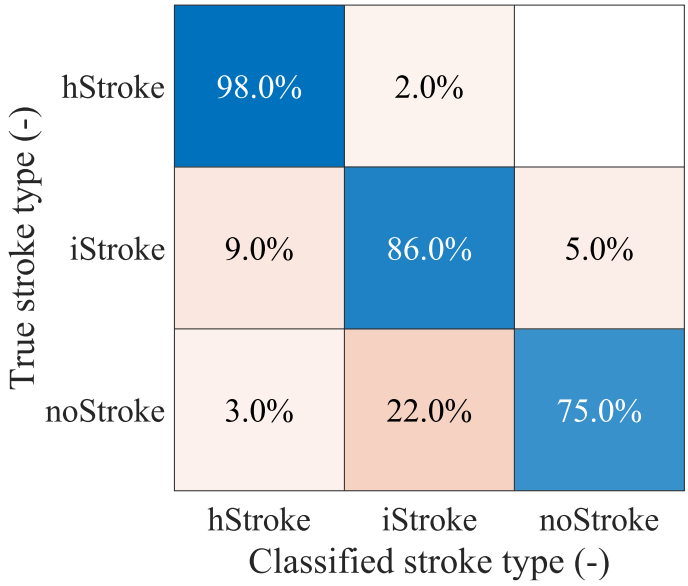

Figure 38: Confusion matrix for test scenario S9 – classification of randomly sized strokes at random positions, 3D numerical simulations datasets.

The SVM algorithm can distinguish between the two classes with an accuracy of 83.7% (see Table 28). Cohen's kappa reaches high values of 0.6. However, from confusion matrix in Figure 39 (a) we can see, that classifications of the class Other to ischemic occurs in 12 %. Misclassification analysis revealed that hStroke was being misclassified as iStroke, which is clinically unacceptable. In response, the cost of this misclassification was increased, resulting in the classification of the class Other as ischemic only occurring in 4% of cases, see Figure 39 (b). For this setting no hStroke misclassification occurred at all. However, this increase in specificity caused a gradual decrease in sensitivity to 68%. This indicates, that the SVM algorithm can reliably classify only about 68% of ischemic stroke patients.

Table 28. Results for test scenario S10 – classification of ischemic strokes, 3D numerical simulations datasets.

Data form (-)	Total dimensions (-)	Reduced dimensions (-)	CL-accuracy (%)	Kappa (-)	Sensitivity (%)	Specificity (%)
ReIm	110	20	83.7	0.63	75.0	88.0
ReIm	110	20	86.7	0.68	68.0	96.0

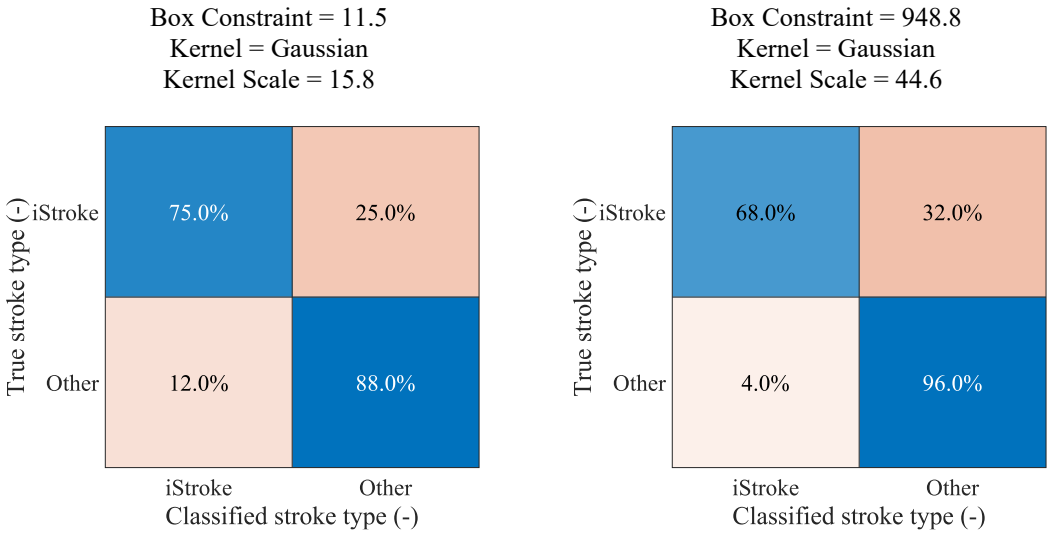

Figure 39: Confusion matrix for test scenario S10 – SVM algorithm without sensitivity limitation (a), with sensitivity set to 100% (b).

3.6.3 Measurements

To verify the generalization ability of the SVM algorithm, we employed experimental data obtained using measurement setup and homogeneous liquid and an anatomically and dielectrically realistic human head phantom at a frequency of 1 GHz. We gradually reduced the dimensions using PCA, as shown in Figure 40. For the homogeneous liquid head phantom data, the highest classification accuracy was 82 % for 60 dimensions. For the anatomically and dielectrically realistic human head phantom data, the highest classification accuracy was 71% for 100 dimensions.

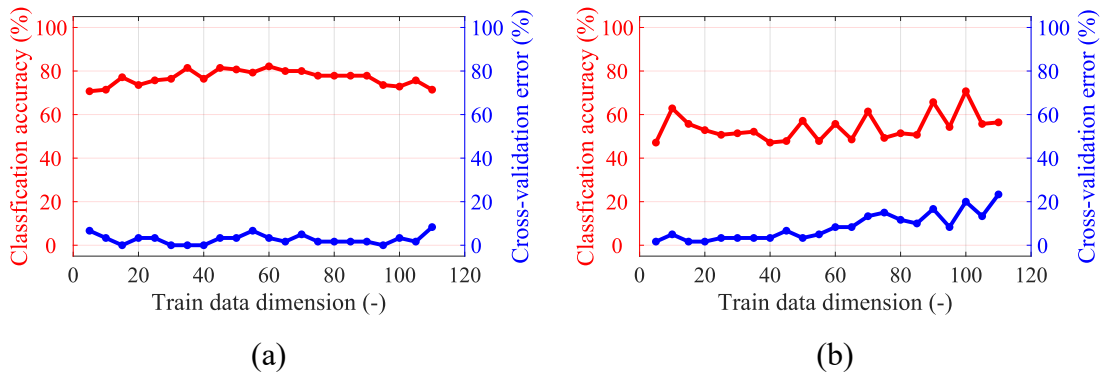

Figure 40. Dimensionality reduction graph for verifying the generalization ability of the SVM algorithm – testing scenario S11. (a) homogenous liquid head phantom and (b) realistic head phantom.

The results of test scenario 12 are in Table 29. It can be concluded that the SVM algorithm is capable of classifying stroke types on experimental data with a 98.1% classification accuracy for the liquid head phantom and 83.1% for the realistic head phantom when strokes of randomly varying sizes are placed at random positions in the brain. However, from the confusion matrix in Figure 41, it can be observed that for both the liquid phantom and the realistic phantom, there are misclassifications of the hStroke to iStroke scenario, which is not clinically acceptable.

Table 29. Results for test scenario S12 – classification of randomly sized strokes at random positions for measurements with homogeneous liquid head phantom and dielectrically and anatomically realistic head phantom.

Phantom Type (-)	**Data form (-)**	**Total dimensions (-)**	**Reduced dimensions (-)**	**CL-accuracy (%)**	**Kappa (-)**	**Hyperparameters Optimalization Settings (-)**
Liquid head	ReIm	110	20	98.1	0.95	Box Constraint = 36.0 Kernel = Gaussian Kernel Scale = 4.9
Realistic Head	ReIm	110	20	83.3	0.62	Box Constraint = 981.5 Kernel = Gaussian Kernel Scale = 7.1

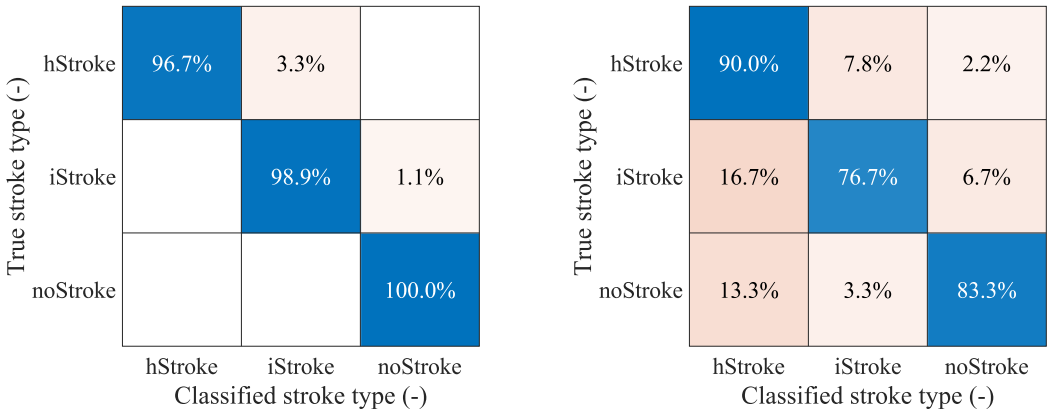

Figure 41: Confusion matrix for testing scenario S12 – classification classifying randomly sized strokes at random positions for measurements homogeneous liquid head phantom (a) and dielectrically and anatomically realistic head phantom (b).

The SVM algorithm demonstrates an ability to distinguish the presence of an ischemic stroke (class iStroke) from healthy individuals or those with bleeding (class Other) with an accuracy exceeding 94 %, as evidenced by Table 30. The Cohen's kappa value is high, exceeding 0.8. However, the confusion matrices in Figure 42 (a, c) show that there are misclassifications of the class Other as ischemic for both the liquid head phantom and the realistic head phantom. After misclassification analysis, it was revealed that hStroke was being misclassified as iStroke, which is clinically unacceptable. In response, the cost of this misclassification was increased, resulting in the classification of the class Other as ischemic only occurring in 0% of cases for the liquid phantom (see Figure 42(b) and the classification of the class Other as ischemic for the realistic head phantom only occurring in 0.8% (see Figure 42(d)), but fortunately without the presence of hStroke misclassification. In both the realistic head phantom and the liquid head phantom, this increase in specificity resulted in an increase in sensitivity.

Table 30. Results for test scenario S13 –classification of ischemic strokes for measurement with homogeneous liquid head phantom and dielectrically and anatomically realistic head phantom.

Phantom Type (-)	**Data form (-)**	**Total dimensions (-)**	**Reduced dimensions (-)**	**CL-accuracy (%)**	**Kappa (-)**	**Sensitivity (%)**	**Specificity (%)**
Liquid head	ReIm	110	20	94.3	0.88	94.4	94.2
Liquid head	ReIm	110	20	99.5	0.99	98.9	100
Realistic head	ReIm	110	20	80.0	0.59	72.2	85.6
Realistic head	ReIm	110	20	91.4	0.82	81.1	99.2

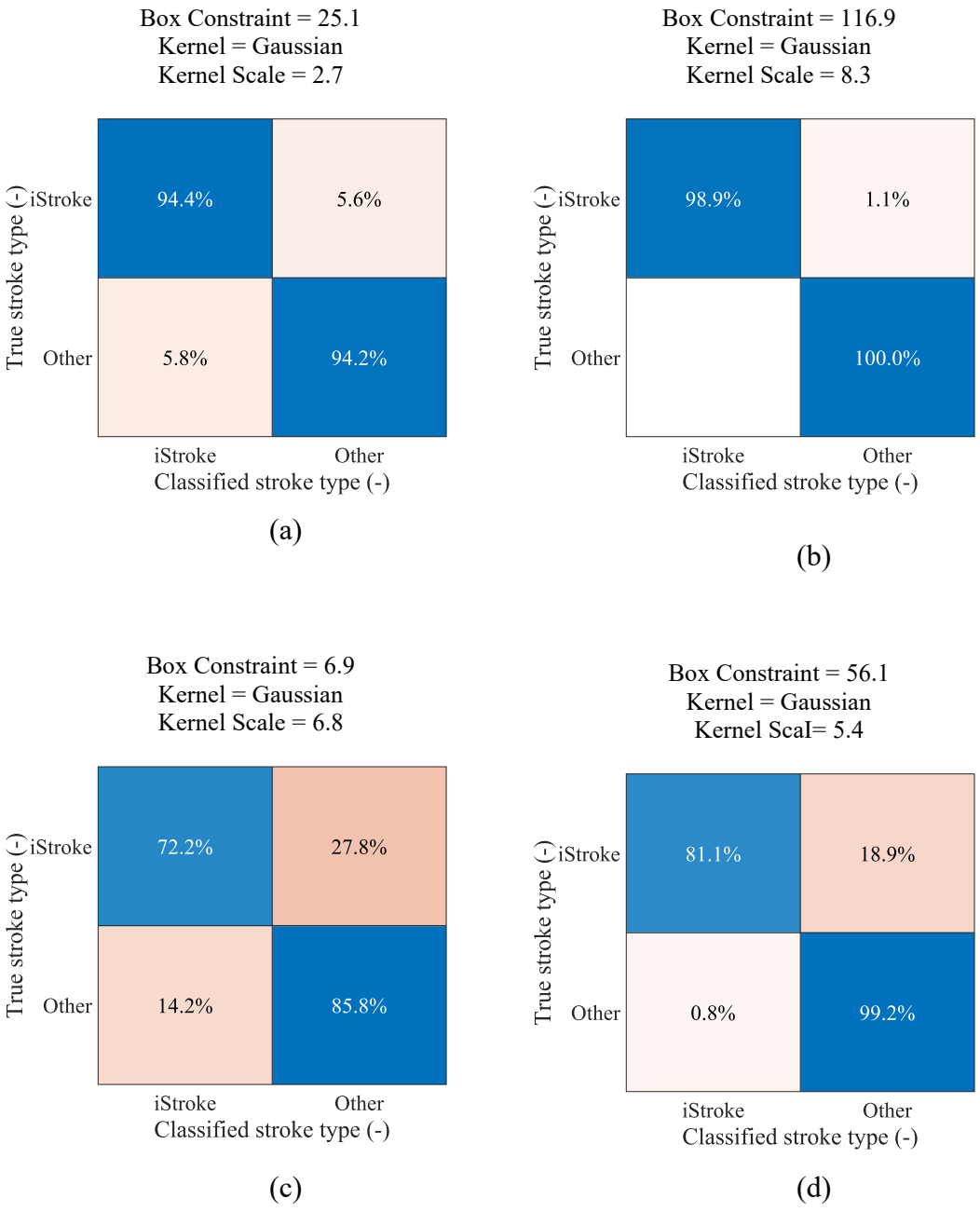

Figure 42: Confusion matrixes for test scenario S13 – (a) and (b) the SVM algorithm for the liquid head phantom, with and without an increase in misclassification cost, (c) and (d) the SVM algorithm for a realistic head phantom, with and without an increase in misclassification cost.

4. Discussion

The main result of this work is the adaptation of the SVM algorithm for stroke classification using the most suitable data from the microwave antenna array surrounding a adult human head. Our findings indicate that the adapted SVM algorithm is not able to accurately classify the type of stroke, including ischemic and hemorrhagic strokes, or patients without stroke in cases where the data exhibits a higher degree of variability that is closer to natural scenarios. Misclassifications occur when classifying into three classes, which could potentially endanger the patient's life in the case of incorrect initiation of treatment based on the algorithm's result. However, the algorithm demonstrates high accuracy in classifying ischemic strokes and is capable of safely recommending thrombotic therapy initiation in approximately 70 % of patients with this condition. The SVM algorithm was tested on datasets from a 10-port microwave system for 2D and 3D numerical simulations and measurements.

4.1 2D and 3D numerical models

The chapter is based on the author's article published in a journal with impact factor [116] and [117].

The numerical 5-layer models of 10 different human heads were created in both 3D and 2D. The 2D models geometry is cross-section of the 3D model geometry in the brain. In previous studies [95], [103] only a single head model was used and data variability was increased by geometry scaling. The created 2D and 3D models can be used to refine stroke diagnosis algorithms and develop novel monitoring and therapeutic systems for the head region. For example, the models can be used to investigate hyperthermia treatment of head tumors as in [117].

4.2 Numerical models validation

The chapter is based on the author's article published in a journal with impact factor [116].

Numerical models of the antenna array for an existing experimental microwave system with 10 antennas were created in 2D and 3D variants. In general, the 2D numerical model does not consider the propagation of EM waves in the 3rd dimension. In this work, a global optimization method was used to find the size of the boundary condition of the

antenna port in 2D, which ensure a good match between the measured and 2D simulated transmission coefficients. Therefore, the magnitudes of the transmission parameters obtained from experimental measurements and 2D numerical simulations are in good agreement, as shown in Figure 26 (a). However, the agreement in the reflection coefficients for the 2D numerical simulations is comparatively weaker. This issue does not exist in 3D numerical model, and Figure 26 (b) demonstrates good agreement between both the reflection and transmission coefficients from the 3D numerical simulations and measurements. The calculated S-parameters are symmetric with respect to the main diagonal, whereas the S-parameters obtained experimentally exhibit slight asymmetry. These differences could be attributed to noise or temperature fluctuations and should be taken into consideration when detecting a stroke. The noise level that was observed in the experimental data was added in the form of white gaussian noise of the same level to the calculated S-parameters.

Changes in S-parameter values induced by the presence of ischemic and hemorrhagic stroke were studied using 2D and 3D numerical simulations and measurements. The reflection coefficients did not change upon insertion of the stroke, but changes in the transmission coefficients were observed, even in the worst-case scenario with the stroke located in the middle of the brain. The changes in transmission coefficients were different for ischemic and hemorrhagic stroke, which is a prerequisite for using machine learning algorithms for stroke classification. In addition, both the 2D and 3D numerical simulations, as well as the measurements, revealed changes in the transmission parameters for the stroke location (-20, 30). The results indicate that the changes in the transmission coefficients are more pronounced in the 2D model than in the 3D model. This can be attributed to the way the waves propagate in the 2D numerical simulations, which do not account for wave propagation below and above the stroke. The measurements of ischemic stroke correlate well with the 3D numerical simulation. However, the measurements of hemorrhagic stroke exhibit higher changes in the S-matrix compared to the 3D numerical simulation. This could be due to the higher conductivity of the hemorrhagic stroke model discussed in the following chapter.

4.3 Head and stroke phantoms

The chapter is based on the author's article published in a journal with impact factor [126] and conference paper [125].

A realistic adult human head phantom was developed, including the scalp, skull, cerebrospinal fluid, and brain tissue layer complementary with ischemic and hemorrhagic stroke phantoms. In contrast to the previously described approach [8], this phantom is a 3D representation of the human head anatomy. The use of updated molds allowed for more precise control over the xyz-positioning of the individual layers. The dielectric properties of individual tissues have a relative error of up to 30%, except for tissues with high dielectric properties such as cerebrospinal fluid and hemorrhagic stroke, where the relative error is up to 80%. Producing phantoms with high dielectric parameters using polyurethane and conductive powders can be challenging due to the high stiffness of the mixture when larger quantities of powder are used. This can result in inhomogeneities of the phantom throughout its volume [8]. The head phantom enables changing of stroke type, size and location, making it a suitable tool for obtaining large datasets, unlike the previously presented solutions [11], [136], [137].

The computer-controlled stroke positioning system developed in this study enables control of the position of the stroke phantom only in the x and y directions. To change the position of the phantom along the z-axis, a plastic rod of variable length is used to hold the phantom. One limitation of this approach is that the microwave system and phantom must be placed upside-down to fill the brain phantom with liquid. This approach was used, for example, in [56], [138]. The motion of the stepper motors and the stroke model can cause vibrations and waves on the surface of the liquid phantom, which may affect the measurement. To mitigate this, a 10-second pause was added after the motion was completed before taking measurements. No step loss was observed during the measurements, and the stroke model always returned to the initial position. However, we recommend calibrating the phantom before each measurement and after replacing the stroke model. Once the position change is complete, the motors are turned off to avoid any potential current flow that could affect the measurement. However, caution must be exercised when replacing the phantom to avoid moving the middle part of the system with the stroke holder.

4.4 Training and testing datasets

Numerical simulations and experimental measurements were utilized to obtain training and testing datasets for the SVM algorithm. 2D numerical simulations allow for extensive multi-frequency simulations in a short period. In total, three datasets were generated from 2D numerical simulations. 2D datasets reflect the highest data variability, resulting from the variation in type, size, and position of stroke and the use of 10 scaled head phantoms. Based on the results of the 2D numerical simulations, we created three 3D numerical datasets that accurately approximates the real measurements, thanks to the quality of the model and the incorporation of the noise from the measurements. Nevertheless, we performed measurements to validate the results of the obtained numerical simulations.

These datasets can be utilized to investigate the performance and limits of the classification algorithms, optimize their setting and evaluate their potential for the given application. The datasets have been, in the case of 2D simulations, or will be, in the case of 3D simulations, shared with the community to test their developed algorithms. In this study, we utilized the datasets to test specific scenarios.

4.5 Data variability and noise

In Figure 31 we demonstrated changes in relative magnitude differences for presence of iStroke and hStroke. As expected, the presence of hStroke caused a higher data variability than the presence of iStroke. This is because hemorrhage has greater differences in dielectric parameters than ischemia [37], [42]. Moreover, as expected, strokes with a smaller size induce less variability in the data compared to strokes with larger size. This finding enabled us to formulate testing scenario S1.

The noise level in the measurements was determined experimentally using a simplified liquid phantom and is represented in Figure 32 as relative magnitude differences changes of ±0.75 dB, corresponding to an 85 dB noise level. The authors of study [95] used noise information from the vector analyzer datasheet. In contrast, our measurements did not use absorbers and shielding around the microwave system, providing a more realistic assessment of the noise conditions than if we had relied solely on the noise information provided in the vector analyzer datasheet. The noise level had a greater impact on the transmission of the opposite antennas. . However, repeated

calibration resulted in much larger changes in reflection and transmission parameters, possibly due to bending of the cables connecting the switch matrix to the antenna automatic calibration unit ZN-Z153 Rohde & Schwarz.

For our experimental setup the relative magnitude differences caused by small ischemic strokes (size 20 mm in diameter) are smaller than the noise level, as indicated by the 25th and 75th percentile of box plot (see Figure 31). Variability in reflection and transmission parameters that exceed the 85dB noise level may contribute to the observed variability. This provides a basis for stroke detection and classification. Physical limit of the state-of-the-art microwave measurement hardware is 140 dB.

4.6 Principal component analysis

Principal component analysis was employed for dimensionality reduction and analysis of variance of data in real and imaginary components format versus data in module and phase format. Most papers dealing with stroke classification (see section 1.4) do not explicitly mention the data format used, we can expect use of real and imaginary parts. As shown in Figure 33, the variance graph for the individual principal components is higher for the module and phase format compared to the real and imaginary components format. This suggests that the use of module and phase data may increase the variance of the data, which has the potential to improve the performance of the classifier. However, the variance difference between individual principal components was not as significant for the experimental data, which may be attributed to the lower variability of the data.

Furthermore, we plotted the first three principal components, i.e. the components with the highest variance to obtain the arrangement of data in 3D space, as shown in Figure 34. For the data represented in the format of the real and imaginary parts of S - parameters, the plotted points exhibited well-defined clusters that enabled better separation of iStroke, hStroke, and noStroke data compared to the data in the modulus and phase format, where the points appeared to be more blended together. These results suggest that the use of data in the real and imaginary part format may be more suitable for the classification algorithm.

4.7 Scenario testing

The chapter is partially based on the author's article published in a journal with impact factor [116].

Thirteen testing scenarios were proposed to systematically test the performance of the machine learning algorithms using datasets obtained from both 2D and 3D numerical simulations, as well as measurements.

4.7.1 2D numerical simulation

S1: From Table 21 we can conclude that when training the algorithm only on the data of subjects with the smallest strokes (diameter 20 mm), the SVM algorithm achieved the highest classification accuracy of subjects with larger strokes up to a diameter of 40 mm. On the other hand, the cross-validation error increased from 5.5% to 11.8%. We assume that data of subjects with larger strokes contain higher variability; therefore, it is easier to classify them, and the algorithm achieves a smaller cross-validation error when training for larger strokes. Useful information for creating a support vector is provided by small-stroke subjects; however, they are more difficult to divide, which is why the Cross-validation error is higher than for larger strokes.

S2: SVM trained on data containing one and five frequency points showed almost identical classification accuracy and cross-validation error. They also outperformed an SVM trained with data containing a larger number of frequency points, even though the performance of the latter was enhanced by dimensionality reduction using PCA. This means that for this particular application, it would be sufficient to use a narrowband imaging system.

S3: The confusion matrices for the classification of ischemic and hemorrhagic strokes of random sizes are shown in Figure 35. The classification between ischemic and hemorrhagic stroke was accurate and only 6.5% of strokes were classified as non-stroke scenario and 6.0% of no strokes were classified as ischemic stroke. Pre-hospital MW detection and classification of cerebrovascular events have the following specifics. Ischemic strokes need to be detected because they can be treated immediately with thrombolytic therapy. A situation where a hemorrhagic stroke is classified as ischemic is completely unacceptable. Thrombolytic therapy in case of hemorrhagic stroke causes

hematoma enlargement and increases the risk of mortality [5]. It is, therefore, possible to consider only a 2-class classification into ischemic cerebrovascular events and the rest. In testing scenario S3, unacceptable misclassification was observed only when we classified random stroke sizes at random positions. When we increased the number of positions misclassification was eliminated.

S4: We tested if the SVM algorithm for stroke classification trained on data of the subjects with small strokes can accurately classify random size and random position strokes. From Table 23 we can conclude that only 20 iStroke and hStroke positions were not enough and the SVM algorithm only achieved a 63.5% classification accuracy. For 83 and 456 iStroke and hStroke positions SVM algorithm achieved classification accuracy of 70% and 71%, respectively. Furthermore, we observed that the box constraint, which was determined by the optimization of the hyper-parameters, reached high values. High box constraint values suggest good separation and fewer misclassifications for the training data. However, this may result in reduced robustness when applied to unknown data, such as random stroke size and position. For this data the SVM algorithm was unable to accurately classify strokes and achieves only 70% classification accuracy. We also checked which samples were misclassified, but no pattern was discovered. From the confusion matrixes in Figure 36 we concluded that most of the inaccurate classifications belonged to the category without stroke, and these stroke patients will be taken to the hospital anyway. The biggest problem in the treatment of stroke patients is the classification of hemorrhagic strokes into the ischemic category. The use thrombotic therapy in hemorrhagic stroke causes hematoma enlargement and increases the risk of mortality [5]. For this situation, there were no misclassifications for the 456 iStroke and hStroke positions used for SVM algorithm training.

S5: In our study, we focused on evaluating the effectiveness of the SVM algorithm for stroke classification, as it is the most used algorithm for this application. However, we also tested the performance of other machine learning algorithms, except deep neural networks that require a large amount of training data. As shown in Table 24, the SVM algorithm achieved the highest classification accuracy, while the kNN algorithm and logistic regression performed better than probability estimation, with Cohen's kappa values exceeding 0. On the other hand, the discriminant analysis, nearest neighbors, and

classification trees algorithms achieved classification accuracies lower than a statistical estimate would predict.

4.7.2 3D numerical simulation

S6: We confirmed that the SVM algorithm could be trained using data for strokes of 20 mm in diameter and then successfully classify larger strokes. This generalization capability was previously demonstrated in 2D numerical datasets, and our study verifies it for 3D numerical dataset too. The SVM algorithm achieved 100% accuracy in stroke classification using a dataset of approximately 25 to 45 dimensions, with the lowest cross-validation error observed at 40 dimensions, as shown in Figure 37.

S7: The classification accuracy was studied for two different data formats. We found (see Table 25) that the real and imaginary part format provided the highest classification accuracy compared to the module and phase format despite the fact that the module and phase data showed a slightly higher variance of principal components compared to the real and imaginary parts (as shown in Figure 33). On the other hand, our classification result corresponds to the distribution of the first three principal components. As demonstrated in Figure 34, the plotted points of the data represented in the real and imaginary part format exhibited well-defined clusters, which allowed for better separation of iStroke, hStroke, and noStroke data, whereas the points in the modulus and phase format appeared more blended together. Therefore, our findings suggest that the choice of data representation has significant impact on the accuracy of stroke classification, and we recommend using the data in the original format of the real and imaginary components.

S8: In the figures included in Appendix C, we have demonstrated that the presence of pathology inside the head did not significantly affect the reflection parameters in the data. Building on this, we conducted a test whether using only transmission parameters would result in the same classification accuracy as using both transmission and reflection parameters together. The results, shown in Table 26, indicate a slight decrease in classification accuracy when using transmission parameters only for training and classification. This suggests that further reduction of the S-matrix beyond the 55 independent elements for 10 antennas may not be recommended. However, our study has shown that dimensionality reduction using PCA can improve classification accuracy and

we recommend its use for future testing. Further exploration of feature extraction techniques may also be beneficial in enhancing classification performance.

S9: We tested whether the classification accuracy for strokes of random size and position exceeded 85%, a threshold chosen based on the assertion in [3], which states that 85% of strokes are ischemic. We tested that the SVM algorithm would outperform statistical probability in identifying the stroke type. The early initiation of thrombotic therapy is critical for treating ischemic strokes, as it helps dissolve clots and alleviate the disease consequences [13]. The SVM algorithm achieved a classification accuracy of 86%. The Cohen's kappa value, which measures agreement beyond chance, reached a value of 0.69, indicating that the algorithm achieved higher accuracy than random estimation. A kappa value as low as 0.41 may be considered acceptable in medical studies [139]. A high value of Box Constraint indicates that the algorithm created a small margin. Together with a higher value of Kernel Scale, it indicates good separation of training data but less general separation margin. The confusion matrix in Figure 38 revealed that 2% of hemorrhagic strokes were classified incorrectly as ischemic strokes, which is an unacceptable clinical outcome [5]. Thrombotic therapy in hemorrhagic strokes may lead to hematoma enlargement and increase the risk of mortality [21]. Based on these findings, we propose the use of a 2-class SVM classifier, where we assume that classification between ischemic stroke (iStroke) and hemorrhagic stroke (hStroke) scenarios will be easier.

S10: This work has shown that the SVM algorithm is capable of identifying the presence of ischemic stroke, achieving an accuracy of 83.7% (as presented in Table 28). Cohen's kappa also confirmed that the results were not due to random chance. However, it is concerning that 12% of misclassifications from the Other class to ischemic stroke included hemorrhagic stroke patients, which is a clinically unacceptable outcome [5]. To address this issue, we increased the cost of misclassifications. The updated algorithm achieved only 4 % of misclassifications without misclassifying patients with hemorrhagic stroke, as determined by analyzing the information matrix for the test data and comparing it with the classification results. However, this increase in specificity resulted in a gradual decline in sensitivity to 68%, meaning that we can only reliably administer thrombotic

therapy to around 68% of people with ischemic stroke, which amounts to approximately 6 million individuals per year [2].

4.7.3 Measurements

S11: Figure 40 shows that the generalization capability was not confirmed for experimental data. The inability to generalize for experimental data is likely related to the lower number of training data available for experimental measurements. In numerical simulations, a total of 10 different head models were used, leading to a tenfold increase in the dataset size for training and testing. To further test the SVM algorithm's performance, we trained it on 20 mm, 30 mm, and 40 mm strokes located in 20 positions.

S12: Figure 41 shows that, for the classification of strokes at random positions, the SVM algorithm achieved an accuracy rate above the 85 percent threshold only for the liquid phantom. However, for the realistic phantom, the success rate was only 83 percent, which is lower but expected result due to the higher complexity of the more realistic phantom. As in the 3D numerical simulations, clinically unacceptable misclassifications occurred where hStroke was classified as iStroke. The results of the 3D simulations with added measurement noise suggest that the classification accuracy for measurements is unlikely to improve. Therefore, we recommend using a 2-class SVM algorithm to reliably differentiate iStroke from other types and safely initiate treatment, as was done in the 3D numerical simulations.

S13: The SVM algorithm demonstrated the ability to identify the presence of ischemic stroke with an accuracy of approximately 94% for the liquid phantom and 80% for the realistic phantom (see Table 30). This represents a higher classification accuracy than observed with the 3D numerical data, which may be due to the lower complexity of the experimental measurement data (only one phantom was used). However, as observed in the 3D numerical simulations, the algorithm misclassified some cases from the Other class as iStroke class. After analyzing these misclassifications, it was revealed that these misclassifications also came from hStroke, which is clinically unacceptable. To address this issue, the cost of misclassifications was increased, resulting in an updated algorithm with no clinically unacceptable misclassifications. Misclassifications in the Other class were determined by analyzing the information matrix for the test data and comparing it with the classification results. There were only 0.8 % misclassifications from the noStroke

to iStroke class for the realistic head phantom (see Figure 42). The algorithm demonstrated a sensitivity of over 80 % for both the measurement of the liquid head phantom and the realistic head phantom, which is a notable finding. This high sensitivity could allow for the safe initiation of thrombotic therapy for ischemic patients.

4.8 Comparison stroke classification results with published studies

The results are partially comparable to [101], where a study of the feasibility of subdural hematoma classification by the SVD-based algorithm was performed on synthetic data from 2D numerical simulations. The authors achieved 82–96% classification success rate, considering only a two-class classification of healthy subjects and subjects with subdural hematomas. The study did not consider cases of ischemic stroke. Subdural hematoma is distinct from intracerebral hemorrhage, which is the most common type of hemorrhage in stroke patients. Intracerebral hemorrhage is located within the brain tissue and is usually of spherical shape and is generally characterized by a smaller volume than subdural hematoma; therefore, subdural hematoma may be classified with higher accuracy. The 2D numerical model is a significant simplification; therefore, a 3D numerical model was presented in [103]. Again, a two-class classification is performed. In our study, the results of classification into three classes are presented.

In [95], an alternative and efficient method was introduced to create the training dataset, based on the distorted Born approximation, to obtain a linear scattering operator from the dielectric contrast space to the scattering parameters' one. A dataset containing 10,000 samples was created in a relatively short time and with low computational effort. On the other hand, a single 3D CAD model of a human head was used and scaled to obtain a total of 10 head models. In our study, a higher data variability was considered because each numerical simulation involved randomly scaling one of 10 different head models.

The algorithms were tested in [95] on a large amount of data obtained from the linear dispersion operator. An evaluation of the suitability of different datasets for training was not conducted. In our study, we tested the effect of using multi-frequency data on classification accuracy, but the results show and agree with the statement in [95] that single-frequency data is sufficient for this application.

Classification using the SVM algorithm with a different data processing approach was performed in [82]. Data were obtained for 10 head models without scaling and only for ellipsoidal strokes of 10 mm^3 to 35 mm^3. A total of 100 stroke head models were created. A two-class classification was performed between iStroke and hStroke classes. The noStroke class was excluded. Inverse FFT was used to convert these signals to time series signals. Data variability was increased by adding noise, which also significantly reduced the classification success rate from 94% to 77%. In [108], dimensionality reductions by PCA led to classification success rate increase to 99%. The increase in the classification success using PCA also confirms our results, even though it was a different data processing approach.

4.9 Further plans

Training data for machine learning algorithms should ideally be obtained from measurements performed in subjects with acute strokes. However, these patients are in a life-threatening situation. In future, we plan to expand the number of training data for 3D numerical simulations. As 3D simulations can be computationally demanding, we plan to use a linear operator for efficient data generating [107]. This approach could also be useful in clinical settings, where it could facilitate obtaining the training data, thereby accelerating the deployment of the system into clinical practice.

Machine learning algorithms do not provide the position or size of the stroke in the human head; therefore, in the future, we propose to combine the SVM algorithm with the TSVD Born approximation to obtain an image of the observed area. Both algorithms can be used on the same device. This would enable the potential for in-bedside monitoring of stroke treatment using a microwave system designed for pre-hospital diagnosis.

In this work we used a single antenna ring placed in axial plane, which might be a limitation in this study. PCA significantly reduce the dimension of the data, therefore we plan to investigate whether all 10 antennas are necessary for accurate stroke detection. Further we plan to investigate suitable antenna placement in a spherical arrangement around the head [95]. We are currently developing a system with 24 antennas [57], which will allow us to test the classification algorithm using a different number of antennas and identify on the most appropriate number of antennas.

The goal of our research will be clinical testing in patients. This will involve tests in ambulances while patients are being transported to a hospital, ideally on an international scale. The clinical testing phase is crucial in our research and will help to validate the efficacy and accuracy of the microwave system in a clinical setting.

5. Conclusion

This work systematically investigated the potential of SVM for microwave detection and classification of stroke. For this purpose, using validated 2D and 3D numerical models and an experimental setup, large datasets (S-parameters) were generated for training and testing algorithms with different levels of data variability. Both the numerical models and the experimental setup consisted of a microwave antenna array surrounding an anatomically and dielectrically realistic human head model with adjustable geometry with and without a stroke model. The variability of the data was increased by including different degrees of freedom, regarding stroke size, position, head model type and size, and frequency points with the addition of random white noise. The results demonstrate the ability of SVM algorithm to detect the presence of a stroke and classify it into either ischemic or hemorrhagic subtypes.

In this work, it was confirmed that PCA dimensionality reduction significantly improved the classification results, s single-frequency data (1 GHz) will provide the same information as multi-frequency data for this application, which simplifies measurement hardware. The results showed higher classification success for datasets containing both transmission and reflection coefficients, compared to datasets with transmission coefficients only and also if the datasets are given in real and imaginary part, compared to module and phase.

Furthermore, it was shown, that the datasets of subjects with smaller strokes appears to be the most suitable for training accurate SVM predictors with high generalization capabilities for stroke-trained position placement. Overall, the study indicates that in the case of natural variability of data, accurate detection and classification of stroke will be challenging.

Nevertheless, our SVM algorithm demonstrated an ability to accurately classify ischemic strokes and suggest safe initiation of thrombotic therapy in approximately 70 % of ischemic stroke patients. This finding holds significant clinical implications, as it could reduce the adverse consequences of strokes and improve the lives of many stroke patients. Further research is needed to improve the sensitivity of the algorithm and increase its clinical usefulness.

REFERENCES

[1] M. Persson *et al.*, "Microwave-Based Stroke Diagnosis Making Global Prehospital Thrombolytic Treatment Possible," *IEEE Transactions on Biomedical Engineering*, vol. 61, no. 11, pp. 2806–2817, Nov. 2014, doi: 10.1109/TBME.2014.2330554.

[2] "WHO | The world health report 2002 - Reducing Risks, Promoting Healthy Life," *WHO*. http://www.who.int/whr/2002/en/ (accessed Mar. 31, 2018).

[3] "Ischaemic stroke guide," *Stroke Association*, Jan. 13, 2015. https://www.stroke.org.uk/resources/ischaemic-stroke-guide (accessed Jan. 22, 2023).

[4] T. D. Musuka, S. B. Wilton, M. Traboulsi, and M. D. Hill, "Diagnosis and management of acute ischemic stroke: speed is critical," *CMAJ*, vol. 187, no. 12, pp. 887–893, Sep. 2015, doi: 10.1503/cmaj.140355.

[5] I. J. McGurgan, W. C. Ziai, D. J. Werring, R. A.-S. Salman, and A. R. Parry-Jones, "Acute intracerebral haemorrhage: diagnosis and management," *Practical Neurology*, vol. 21, no. 2, pp. 128–136, Apr. 2021, doi: 10.1136/practneurol-2020-002763.

[6] A. Fhager, S. Candefjord, M. Elam, and M. Persson, "Microwave Diagnostics Ahead: Saving Time and the Lives of Trauma and Stroke Patients," *IEEE Microwave Magazine*, vol. 19, no. 3, pp. 78–90, May 2018, doi: 10.1109/MMM.2018.2801646.

[7] M. Salucci, M. Arrebola, T. Shan, and M. Li, "Artificial Intelligence: New Frontiers in Real-Time Inverse Scattering and Electromagnetic Imaging," *IEEE Transactions on Antennas and Propagation*, vol. 70, no. 8, pp. 6349–6364, Aug. 2022, doi: 10.1109/TAP.2022.3177556.

[8] R. Raghupathi, "Cell death mechanisms following traumatic brain injury," *Brain Pathol*, vol. 14, no. 2, pp. 215–222, Apr. 2004, doi: 10.1111/j.1750-3639.2004.tb00056.x.

[9] "Stroke Statistics | Internet Stroke Center." http://www.strokecenter.org/patients/about-stroke/stroke-statistics/ (accessed Mar. 31, 2018).

[10] “Neurosciences - What is Stroke,” *UTMBHealthCOM*, May 28, 2021. https://www.utmbhealth.com/services/neurology/procedures-conditions/stroke/what-is-stroke (accessed Feb. 20, 2023).

[11] B. Mohammed, A. Abbosh, B. Henin, and P. Sharpe, “Head phantom for testing microwave systems for head imaging,” in *2012 Cairo International Biomedical Engineering Conference (CIBEC)*, Dec. 2012, pp. 191–193. doi: 10.1109/CIBEC.2012.6473320.

[12] S. Y. Semenov and D. R. Corfield, “Microwave Tomography for Brain Imaging: Feasibility Assessment for Stroke Detection,” *International Journal of Antennas and Propagation*, 2008. https://www.hindawi.com/journals/ijap/2008/254830/ (accessed Oct. 23, 2017).

[13] W. J. Powers *et al.*, “2018 Guidelines for the Early Management of Patients With Acute Ischemic Stroke: A Guideline for Healthcare Professionals From the American Heart Association/American Stroke Association,” *Stroke*, vol. 49, no. 3, pp. e46–e110, 2018, doi: 10.1161/STR.0000000000000158.

[14] J. Kim *et al.*, “Global Stroke Statistics 2019,” *International Journal of Stroke*, p. 1747493020909545, Mar. 2020, doi: 10.1177/1747493020909545.

[15] Saver Jeffrey L., “Time Is Brain—Quantified,” *Stroke*, vol. 37, no. 1, pp. 263–266, Jan. 2006, doi: 10.1161/01.STR.0000196957.55928.ab.

[16] J. L. Saver *et al.*, “The ‘Golden Hour’ and Acute Brain Ischemia,” *Stroke*, vol. 41, no. 7, pp. 1431–1439, Jul. 2010, doi: 10.1161/STROKEAHA.110.583815.

[17] H. P. Adams *et al.*, “Guidelines for Thrombolytic Therapy for Acute Stroke: a Supplement to the Guidelines for the Management of Patients with Acute Ischemic Stroke. A statement for healthcare professionals from a Special Writing Group of the Stroke Council, American Heart Association,” *Stroke*, vol. 27, no. 9, pp. 1711–1718, Sep. 1996.

[18] C. Laredo *et al.*, “Prognostic Significance of Infarct Size and Location: The Case of Insular Stroke,” *Sci Rep*, vol. 8, p. 9498, Jun. 2018, doi: 10.1038/s41598-018-27883-3.

[19] A. Bruno, N. Shah, A. E. Akinwuntan, B. Close, and J. A. Switzer, “Stroke size correlates with functional outcome on the simplified modified Rankin Scale

questionnaire," *J Stroke Cerebrovasc Dis*, vol. 22, no. 6, pp. 781–783, Aug. 2013, doi: 10.1016/j.jstrokecerebrovasdis.2012.03.011.

[20] C.-L. Chen, F.-T. Tang, H.-C. Chen, C.-Y. Chung, and M.-K. Wong, "Brain lesion size and location: Effects on motor recovery and functional outcome in stroke patients," *Archives of Physical Medicine and Rehabilitation*, vol. 81, no. 4, pp. 447–452, Apr. 2000, doi: 10.1053/mr.2000.3837.

[21] F. N. Shelton and M. J. Reding, "Effect of lesion location on upper limb motor recovery after stroke," *Stroke*, vol. 32, no. 1, pp. 107–112, Jan. 2001, doi: 10.1161/01.str.32.1.107.

[22] S. E. Findlater *et al.*, "Lesion locations associated with persistent proprioceptive impairment in the upper limbs after stroke," *NeuroImage: Clinical*, vol. 20, pp. 955–971, Jan. 2018, doi: 10.1016/j.nicl.2018.10.003.

[23] E. Millerot-Serrurot *et al.*, "Effect of early decrease in the lesion size on late brain tissue loss, synaptophysin expression and functionality after a focal brain lesion in rats," *Neurochemistry International*, vol. 50, no. 2, pp. 328–335, Jan. 2007, doi: 10.1016/j.neuint.2006.08.016.

[24] C. Lin, N. Chatterjee, J. Lee, R. Harvey, and S. Prabhakaran, "Predictive value of the combination of lesion location and volume of ischemic infarction with rehabilitation outcomes," *Neuroradiology*, vol. 61, no. 10, pp. 1131–1136, Oct. 2019, doi: 10.1007/s00234-019-02234-9.

[25] Portegies Marileen L.P., Selwaness Mariana, Hofman Albert, Koudstaal Peter J., Vernooij Meike W., and Ikram M. Arfan, "Left-Sided Strokes Are More Often Recognized Than Right-Sided Strokes," *Stroke*, vol. 46, no. 1, pp. 252–254, Jan. 2015, doi: 10.1161/STROKEAHA.114.007385.

[26] T. Brott *et al.*, "Measurements of acute cerebral infarction: lesion size by computed tomography," *Stroke*, vol. 20, no. 7, pp. 871–875, Jul. 1989, doi: 10.1161/01.str.20.7.871.

[27] A. J. Yoo *et al.*, "Combining acute diffusion-weighted imaging and mean transmit time lesion volumes with National Institutes of Health Stroke Scale Score improves the prediction of acute stroke outcome," *Stroke*, vol. 41, no. 8, pp. 1728–1735, Aug. 2010, doi: 10.1161/STROKEAHA.110.582874.

[28] D. Šaňák *et al.*, "Impact of diffusion-weighted MRI-measured initial cerebral infarction volume on clinical outcome in acute stroke patients with middle cerebral artery occlusion treated by thrombolysis," *Neuroradiology*, vol. 48, no. 9, pp. 632–639, Sep. 2006, doi: 10.1007/s00234-006-0105-0.

[29] A. J. Yoo, L. A. Verduzco, P. W. Schaefer, J. A. Hirsch, J. D. Rabinov, and R. G. González, "MRI-Based Selection for Intra-Arterial Stroke Therapy," *Stroke*, vol. 40, no. 6, pp. 2046–2054, Jun. 2009, doi: 10.1161/STROKEAHA.108.541656.

[30] Saunders Dawn E., Clifton Andrew G., and Brown Martin M., "Measurement of Infarct Size Using MRI Predicts Prognosis in Middle Cerebral Artery Infarction," *Stroke*, vol. 26, no. 12, pp. 2272–2276, Dec. 1995, doi: 10.1161/01.STR.26.12.2272.

[31] B. Cheng, C. Knaack, N. D. Forkert, R. Schnabel, C. Gerloff, and G. Thomalla, "Stroke subtype classification by geometrical descriptors of lesion shape," *PLoS One*, vol. 12, no. 12, Dec. 2017, doi: 10.1371/journal.pone.0185063.

[32] Steiner I, Gomori J M, and Melamed E, "The prognostic value of the CT scan in conservatively treated patients with intracerebral hematoma.," *Stroke*, vol. 15, no. 2, pp. 279–282, Mar. 1984, doi: 10.1161/01.STR.15.2.279.

[33] Kothari Rashmi U. *et al.*, "The ABCs of Measuring Intracerebral Hemorrhage Volumes," *Stroke*, vol. 27, no. 8, pp. 1304–1305, Aug. 1996, doi: 10.1161/01.STR.27.8.1304.

[34] Jian-Zhong Bao, Shin-Tsu Lu, and W. D. Hurt, "Complex dielectric measurements and analysis of brain tissues in the radio and microwave frequencies," *IEEE Transactions on Microwave Theory and Techniques*, vol. 45, no. 10, pp. 1730–1741, Oct. 1997, doi: 10.1109/22.641720.

[35] G. Schmid, G. Neubauer, and P. R. Mazal, "Dielectric properties of human brain tissue measured less than 10 h postmortem at frequencies from 800 to 2450 MHz," *Bioelectromagnetics*, vol. 24, no. 6, pp. 423–430, Sep. 2003, doi: 10.1002/bem.10123.

[36] A. Peyman, S. J. Holden, S. Watts, R. Perrott, and C. Gabriel, "Dielectric properties of porcine cerebrospinal tissues at microwave frequencies:in vivo,in vitroand systematic variation with age," *Phys. Med. Biol.*, vol. 52, no. 8, pp. 2229–2245, Apr. 2007, doi: 10.1088/0031-9155/52/8/013.

[37] P. A. Hasgall *et al.*, "IT'IS Database for thermal and electromagnetic parameters of biological tissues. Version 4.0," May 2018, doi: 10.13099/VIP21000-04-0.

[38] S. Gabriel, R. W. Lau, and C. Gabriel, "The dielectric properties of biological tissues: III. Parametric models for the dielectric spectrum of tissues," *Phys. Med. Biol.*, vol. 41, no. 11, p. 2271, 1996, doi: 10.1088/0031-9155/41/11/003.

[39] C. Gabriel, S. Gabriel, and E. Corthout, "The dielectric properties of biological tissues: I. Literature survey," *Phys. Med. Biol.*, vol. 41, no. 11, p. 2231, Nov. 1996, doi: 10.1088/0031-9155/41/11/001.

[40] S. Gabriel, R. W. Lau, and C. Gabriel, "The dielectric properties of biological tissues: II. Measurements in the frequency range 10 Hz to 20 GHz," *Phys. Med. Biol.*, vol. 41, no. 11, p. 2251, Nov. 1996, doi: 10.1088/0031-9155/41/11/002.

[41] C. Gabriel, *Compilation of the dielectric properties of body tissues at RF and microwave frequencies*. King's College London, 1996.

[42] S. Semenov, T. Huynh, T. Williams, B. Nicholson, and A. Vasilenko, "Dielectric properties of brain tissue at 1 GHz in acute ischemic stroke: Experimental study on swine," *Bioelectromagnetics*, vol. 38, no. 2, pp. 158–163, Feb. 2017, doi: 10.1002/bem.22024.

[43] J. C. Lin, "Microwave Properties of Fresh Mammalian Brain Tissues at Body Temperature," *IEEE Transactions on Biomedical Engineering*, vol. BME-22, no. 1, pp. 74–76, Jan. 1975, doi: 10.1109/TBME.1975.324546.

[44] A. D. Gean and N. J. Fischbein, "Head trauma," *Neuroimaging Clin N Am*, vol. 20, no. 4, pp. 527–556, Nov. 2010, doi: 10.1016/j.nic.2010.08.001.

[45] J. Leon-Carrion, J. M. Dominguez-Roldan, U. Leon-Dominguez, and F. Murillo-Cabezas, "The Infrascanner, a handheld device for screening in situ for the presence of brain haematomas," *Brain Inj*, vol. 24, no. 10, pp. 1193–1201, 2010, doi: 10.3109/02699052.2010.506636.

[46] C. S. Robertson *et al.*, "Clinical evaluation of a portable near-infrared device for detection of traumatic intracranial hematomas," *J Neurotrauma*, vol. 27, no. 9, pp. 1597–1604, Sep. 2010, doi: 10.1089/neu.2010.1340.

[47] T. Oh, O. Gilad, A. Ghosh, M. Schuettler, and D. S. Holder, "A novel method for recording neuronal depolarization with recording at 125–825 Hz: implications for imaging fast neural activity in the brain with electrical impedance tomography,"

Med Biol Eng Comput, vol. 49, no. 5, pp. 593–604, May 2011, doi: 10.1007/s11517-011-0761-z.

[48] A. Randazzo *et al.*, "An Electrical Impedance Tomography System for Brain Stroke Imaging based on a Lebesgue-Space Inversion Procedure," *IEEE Journal of Electromagnetics, RF and Microwaves in Medicine and Biology*, vol. 5, no. 1, pp. 54–61, Mar. 2021, doi: 10.1109/JERM.2020.2994816.

[49] P. K. Manwaring, K. L. Moodie, A. Hartov, K. H. Manwaring, and R. J. Halter, "Intracranial electrical impedance tomography: a method of continuous monitoring in an animal model of head trauma," *Anesth Analg*, vol. 117, no. 4, pp. 866–875, Oct. 2013, doi: 10.1213/ANE.0b013e318290c7b7.

[50] B. D. Lindsey, E. D. Light, S. W. Smith, H. A. Nicoletto, E. R. Bennett, and D. T. Laskowitz, "Dual matrix arrays integrated into scanner for increased SNR of ultrasound brain helmet," in *2010 IEEE International Ultrasonics Symposium*, Oct. 2010, pp. 1100–1103. doi: 10.1109/ULTSYM.2010.5935451.

[51] B. D. Lindsey, E. D. Light, H. A. Nicoletto, E. R. Bennett, D. T. Laskowitz, and S. W. Smith, "The ultrasound brain helmet: new transducers and volume registration for in vivo simultaneous multi-transducer 3-D transcranial imaging," *IEEE Transactions on Ultrasonics, Ferroelectrics, and Frequency Control*, vol. 58, no. 6, pp. 1189–1202, Jun. 2011, doi: 10.1109/TUFFC.2011.1929.

[52] J. Vrba, České vysoké učení technické v Praze, and Elektrotechnická fakulta, *Lékařské aplikace mikrovlnné techniky*. Praha: Vydavatelství ČVUT, 2003.

[53] A. T. Mobashsher, A. M. Abbosh, and Y. Wang, "Microwave System to Detect Traumatic Brain Injuries Using Compact Unidirectional Antenna and Wideband Transceiver With Verification on Realistic Head Phantom," *IEEE Transactions on Microwave Theory and Techniques*, vol. 62, no. 9, pp. 1826–1836, Sep. 2014, doi: 10.1109/TMTT.2014.2342669.

[54] "Medfield Diagnostics | Safer diagnostics through microwave technology." http://www.medfielddiagnostics.com/en/ (accessed Jun. 13, 2017).

[55] "Emtensor." http://emtensor.com/ (accessed Jun. 13, 2017).

[56] J. A. Tobon Vasquez *et al.*, "A Prototype Microwave System for 3D Brain Stroke Imaging," *Sensors*, vol. 20, no. 9, Art. no. 9, Jan. 2020, doi: 10.3390/s20092607.

[57] J. Tesarik, L. F. Diaz Rondon, and O. Fiser, “Prototype of Simplified Microwave Imaging System for Brain Stroke Follow Up,” in *World Congress on Medical Physics and Biomedical Engineering 2018*, 2019, pp. 771–774.

[58] I. Merunka, A. Massa, D. Vrba, O. Fiser, M. Salucci, and J. Vrba, “Microwave Tomography System for Methodical Testing of Human Brain Stroke Detection Approaches,” *International Journal of Antennas and Propagation*, 2019. https://www.hindawi.com/journals/ijap/2019/4074862/abs/ (accessed Apr. 08, 2019).

[59] M. Salucci, A. Gelmini, J. Vrba, I. Merunka, G. Oliveri, and P. Rocca, “Instantaneous brain stroke classification and localization from real scattering data,” *Microwave and Optical Technology Letters*, vol. 0, no. 0, doi: 10.1002/mop.31639.

[60] M. Salucci, A. Polo, and J. Vrba, “Multi-Step Learning-by-Examples Strategy for Real-Time Brain Stroke Microwave Scattering Data Inversion,” *Electronics*, vol. 10, no. 1, Art. no. 1, Jan. 2021, doi: 10.3390/electronics10010095.

[61] D. Ireland, K. Bialkowski, and A. Abbosh, “Microwave imaging for brain stroke detection using Born iterative method,” *Antennas Propagation IET Microwaves*, vol. 7, no. 11, pp. 909–915, Aug. 2013, doi: 10.1049/iet-map.2013.0054.

[62] L. Guo, M. Khosravi-Farsani, A. Stancombe, K. Bialkowski, and A. Abbosh, “Adaptive Clustering Distorted Born Iterative Method for Microwave Brain Tomography With Stroke Detection and Classification,” *IEEE Trans Biomed Eng*, vol. 69, no. 4, pp. 1512–1523, Apr. 2022, doi: 10.1109/TBME.2021.3122113.

[63] D. O. Rodriguez-Duarte, J. A. Tobon Vasquez, S. De Luque Arias, R. Scapaticci, L. Crocco, and F. Vipiana, “A Portable Microwave Scanner for Brain Stroke Monitoring: Design, Implementation and Experimental Validation,” in *2022 16th European Conference on Antennas and Propagation (EuCAP)*, Mar. 2022, pp. 1–5. doi: 10.23919/EuCAP53622.2022.9769048.

[64] P.-H. Tournier *et al.*, “Microwave tomographic imaging of cerebrovascular accidents by using high-performance computing,” *Parallel Computing*, vol. 85, pp. 88–97, Jul. 2019, doi: 10.1016/j.parco.2019.02.004.

[65] M. Bjelogrlic, M. Volery, B. Fuchs, J.-P. Thiran, J. R. Mosig, and M. Mattes, “Stratified spherical model for microwave imaging of the brain: Analysis and

experimental validation of transmitted power," *Microwave and Optical Technology Letters*, vol. 60, no. 4, pp. 1042–1048, 2018, doi: 10.1002/mop.31101.

[66] R. Scapaticci, L. Di Donato, I. Catapano, and L. Crocco, "A feasibility study on Microwave Imaging for brain stroke monitoring," *Progress In Electromagnetics Research B*, vol. 40, Jan. 2012, doi: 10.2528/PIERB12022006.

[67] S. Semenov, B. Seiser, E. Stoegmann, and E. Auff, "Electromagnetic tomography for brain imaging: From virtual to human brain," in *2014 IEEE Conference on Antenna Measurements Applications (CAMA)*, Nov. 2014, pp. 1–4. doi: 10.1109/CAMA.2014.7003417.

[68] S. Semenov *et al.*, "Electromagnetic tomography for brain imaging: Initial assessment for stroke detection," in *2015 IEEE Biomedical Circuits and Systems Conference (BioCAS)*, Oct. 2015, pp. 1–4. doi: 10.1109/BioCAS.2015.7348385.

[69] S. Semenov, M. Hopfer, R. Planas, A. Hamidipour, and T. Henriksson, "Electromagnetic tomography for brain imaging: 3D reconstruction of stroke in a human head phantom," *2016 IEEE Conference on Antenna Measurements and Applications, CAMA 2016*, pp. 1–4, 2017, doi: 10.1109/CAMA.2016.7815752.

[70] M. Hopfer, R. Planas, A. Hamidipour, T. Henriksson, and S. Semenov, "Electromagnetic tomography for detection, differentiation, and monitoring of brain stroke: A virtual data and human head phantom study," *IEEE Antennas and Propagation Magazine*, vol. 59, no. 5, pp. 86–97, 2017, doi: 10.1109/MAP.2017.2732225.

[71] T. Henriksson *et al.*, "Human Brain Imaging by Electromagnetic Tomography: a mobile brain scanner for clinical settings," in *2022 16th European Conference on Antennas and Propagation (EuCAP)*, Mar. 2022, pp. 1–5. doi: 10.23919/EuCAP53622.2022.9769049.

[72] A. Fedeli, V. Schenone, A. Randazzo, M. Pastorino, T. Henriksson, and S. Semenov, "Nonlinear S-Parameters Inversion for Stroke Imaging," *IEEE Transactions on Microwave Theory and Techniques*, vol. 69, no. 3, pp. 1760–1771, Mar. 2021, doi: 10.1109/TMTT.2020.3040483.

[73] A. T. Mobashsher, A. Mahmoud, and A. M. Abbosh, "Portable Wideband Microwave Imaging System for Intracranial Hemorrhage Detection Using Improved

Back-projection Algorithm with Model of Effective Head Permittivity," *Scientific Reports*, vol. 6, no. 1, Art. no. 1, Feb. 2016, doi: 10.1038/srep20459.

[74] A. T. Mobashsher, K. S. Bialkowski, A. M. Abbosh, and S. Crozier, "Design and Experimental Evaluation of a Non-Invasive Microwave Head Imaging System for Intracranial Haemorrhage Detection," *PLoS ONE*, vol. 11, no. 4, p. e0152351, 2016, doi: 10.1371/journal.pone.0152351.

[75] A. Abbosh, "Microwave systems for head imaging: Challenges and recent developments," in *2013 IEEE MTT-S International Microwave Workshop Series on RF and Wireless Technologies for Biomedical and Healthcare Applications (IMWS-BIO)*, Dec. 2013, pp. 1–3. doi: 10.1109/IMWS-BIO.2013.6756184.

[76] A. Zamani, A. M. Abbosh, and A. T. Mobashsher, "Fast Frequency-Based Multistatic Microwave Imaging Algorithm With Application to Brain Injury Detection," *IEEE Transactions on Microwave Theory and Techniques*, vol. 64, no. 2, pp. 653–662, Feb. 2016, doi: 10.1109/TMTT.2015.2513398.

[77] A. T. Mobashsher and A. M. Abbosh, "On-site Rapid Diagnosis of Intracranial Hematoma using Portable Multi-slice Microwave Imaging System," *Scientific Reports*, vol. 6, no. 1, Art. no. 1, Nov. 2016, doi: 10.1038/srep37620.

[78] A. T. Mobashsher and A. M. Abbosh, "Three-Dimensional Human Head Phantom With Realistic Electrical Properties and Anatomy," *IEEE Antennas and Wireless Propagation Letters*, vol. 13, pp. 1401–1404, 2014, doi: 10.1109/LAWP.2014.2340409.

[79] A. T. Mobashsher, "Wideband microwave imaging system for brain injury diagnosis," Jun. 2016, doi: 10.14264/uql.2016.280.

[80] D. Cook *et al.*, "Case Report: Preliminary Images From an Electromagnetic Portable Brain Scanner for Diagnosis and Monitoring of Acute Stroke," *Front Neurol*, vol. 12, p. 765412, 2021, doi: 10.3389/fneur.2021.765412.

[81] A. S. M. Alqadami, A. Zamani, A. Trakic, and A. Abbosh, "Flexible Electromagnetic Cap for Three-Dimensional Electromagnetic Head Imaging," *IEEE Transactions on Biomedical Engineering*, vol. 68, no. 9, pp. 2880–2891, Sep. 2021, doi: 10.1109/TBME.2021.3084313.

[82] G. Zhu, A. Bialkowski, L. Guo, B. Mohammed, and A. Abbosh, "Stroke Classification in Simulated Electromagnetic Imaging Using Graph Approaches,"

IEEE Journal of Electromagnetics, RF and Microwaves in Medicine and Biology, vol. 5, no. 1, pp. 46–53, Mar. 2021, doi: 10.1109/JERM.2020.2995329.

[83] L. Guo and A. Abbosh, "Stroke localization and classification using microwave tomography with k-means clustering and support vector machine," *Bioelectromagnetics*, vol. 39, no. 4, pp. 312–324, May 2018, doi: 10.1002/bem.22118.

[84] I. Bisio *et al.*, "Variable-Exponent Lebesgue-Space Inversion for Brain Stroke Microwave Imaging," *IEEE Transactions on Microwave Theory and Techniques*, vol. 68, no. 5, pp. 1882–1895, May 2020, doi: 10.1109/TMTT.2019.2963870.

[85] I. Bisio, A. Fedeli, C. Garibotto, F. Lavagetto, M. Pastorino, and A. Randazzo, "Two Ways for Early Detection of a Stroke Through a Wearable Smart Helmet: Signal Processing vs. Electromagnetism," *IEEE Wireless Communications*, vol. 28, no. 3, pp. 22–27, Jun. 2021, doi: 10.1109/MWC.001.2000401.

[86] A. Fhager, T. McKelvey, and M. Persson, "Stroke detection using a broadband microwave antenna system," in *Proceedings of the Fourth European Conference on Antennas and Propagation*, Apr. 2010, pp. 1–3.

[87] A. Fhager and M. Persson, "A microwave measurement system for stroke detection," in *2011 Loughborough Antennas Propagation Conference*, Nov. 2011, pp. 1–2. doi: 10.1109/LAPC.2011.6114001.

[88] J. Ljungqvist, S. Candefjord, M. Persson, L. Jönsson, T. Skoglund, and M. Elam, "Clinical Evaluation of a Microwave-Based Device for Detection of Traumatic Intracranial Hemorrhage," *J Neurotrauma*, vol. 34, no. 13, pp. 2176–2182, Jul. 2017, doi: 10.1089/neu.2016.4869.

[89] "Stroke Finder | Chalmers." https://www.chalmers.se/en/Projects/Pages/Strokefinder.aspx (accessed Apr. 01, 2018).

[90] J. A. Tobon Vasquez *et al.*, "Design and Experimental Assessment of a 2D Microwave Imaging System for Brain Stroke Monitoring," *International Journal of Antennas and Propagation*, vol. 2019, p. e8065036, May 2019, doi: 10.1155/2019/8065036.

[91] R. Scapaticci, J. Tobon, G. Bellizzi, F. Vipiana, and L. Crocco, "Design and Numerical Characterization of a Low-Complexity Microwave Device for Brain

Stroke Monitoring," *IEEE Transactions on Antennas and Propagation*, vol. 66, no. 12, pp. 7328–7338, Dec. 2018, doi: 10.1109/TAP.2018.2871266.

[92] D. O. Rodriguez-Duarte, J. A. T. Vasquez, R. Scapaticci, L. Crocco, and F. Vipiana, "Brick Shaped Antenna Module for Microwave Brain Imaging Systems," *IEEE Antennas and Wireless Propagation Letters*, pp. 1–1, 2020, doi: 10.1109/LAWP.2020.3022161.

[93] D. O. Rodriguez-Duarte *et al.*, "Experimental Validation of a Microwave System for Brain Stroke 3-D Imaging," *Diagnostics*, vol. 11, no. 7, Art. no. 7, Jul. 2021, doi: 10.3390/diagnostics11071232.

[94] D. O. Rodriguez-Duarte, J. A. T. Vasquez, R. Scapaticci, L. Crocco, and F. Vipiana, "Assessing a Microwave Imaging System for Brain Stroke Monitoring via High Fidelity Numerical Modelling," *IEEE Journal of Electromagnetics, RF and Microwaves in Medicine and Biology*, vol. 5, no. 3, pp. 238–245, Sep. 2021, doi: 10.1109/JERM.2020.3049071.

[95] V. Mariano, J. A. Tobon Vasquez, M. R. Casu, and F. Vipiana, "Brain Stroke Classification via Machine Learning Algorithms Trained with a Linearized Scattering Operator," *Diagnostics*, vol. 13, no. 1, Art. no. 1, Jan. 2023, doi: 10.3390/diagnostics13010023.

[96] Md. A. Hakim, Md. Z. Hasan, Md. M. Alam, Md. M. Hasan, and M. N. Huda, "An Efficient Modified Bagging Method for Early Prediction of Brain Stroke," in *2019 International Conference on Computer, Communication, Chemical, Materials and Electronic Engineering (IC4ME2)*, Jul. 2019, pp. 1–4. doi: 10.1109/IC4ME247184.2019.9036700.

[97] B. Akter, A. Rajbongshi, S. Sazzad, R. Shakil, J. Biswas, and U. Sara, "A Machine Learning Approach to Detect the Brain Stroke Disease," in *2022 4th International Conference on Smart Systems and Inventive Technology (ICSSIT)*, Jan. 2022, pp. 897–901. doi: 10.1109/ICSSIT53264.2022.9716345.

[98] T. Badriyah, N. Sakinah, I. Syarif, and D. R. Syarif, "Machine Learning Algorithm for Stroke Disease Classification," in *2020 International Conference on Electrical, Communication, and Computer Engineering (ICECCE)*, Jun. 2020, pp. 1–5. doi: 10.1109/ICECCE49384.2020.9179307.

[99] A. R. Bagasta, Z. Rustam, J. Pandelaki, and W. A. Nugroho, “Comparison of Cubic SVM with Gaussian SVM: Classification of Infarction for detecting Ischemic Stroke,” *IOP Conf. Ser.: Mater. Sci. Eng.*, vol. 546, no. 5, p. 052016, Jun. 2019, doi: 10.1088/1757-899X/546/5/052016.

[100] M. S. Sirsat, E. Fermé, and J. Câmara, “Machine Learning for Brain Stroke: A Review,” *Journal of Stroke and Cerebrovascular Diseases*, vol. 29, no. 10, p. 105162, Oct. 2020, doi: 10.1016/j.jstrokecerebrovasdis.2020.105162.

[101] S. Candefjord *et al.*, “Microwave technology for detecting traumatic intracranial bleedings: tests on phantom of subdural hematoma and numerical simulations,” *Med Biol Eng Comput*, vol. 55, no. 8, pp. 1177–1188, Aug. 2017, doi: 10.1007/s11517-016-1578-6.

[102] S. Candefjord, J. Winges, Y. Yu, T. Rylander, and T. McKelvey, “Microwave technology for localization of traumatic intracranial bleedings-a numerical simulation study,” *Conf Proc IEEE Eng Med Biol Soc*, vol. 2013, pp. 1948–1951, 2013, doi: 10.1109/EMBC.2013.6609909.

[103] A. Fhager, S. Candefjord, M. Elam, and M. Persson, “3D Simulations of Intracerebral Hemorrhage Detection Using Broadband Microwave Technology,” *Sensors*, vol. 19, no. 16, Art. no. 16, Jan. 2019, doi: 10.3390/s19163482.

[104] “The Measure of Man and Woman: Human Factors in Design, Revised Edition | Wiley,” *Wiley.com*. https://www.wiley.com/en-us/The+Measure+of+Man+and+Woman%3A+Human+Factors+in+Design%2C+Revised+Edition-p-9780471099550 (accessed Jan. 04, 2023).

[105] V. Mariano, J. A. T. Vasquez, M. R. Casu, and F. Vipiana, “Model-Based Data Generation for Support Vector Machine Stroke Classification,” in *2021 IEEE International Symposium on Antennas and Propagation and USNC-URSI Radio Science Meeting (APS/URSI)*, Dec. 2021, pp. 1685–1686. doi: 10.1109/APS/URSI47566.2021.9704125.

[106] V. Mariano, M. R. Casu, and F. Vipiana, “Simulation-based Machine Learning Training for Brain Anomalies Localization at Microwaves,” in *2022 16th European Conference on Antennas and Propagation (EuCAP)*, Mar. 2022, pp. 1–3. doi: 10.23919/EuCAP53622.2022.9769504.

[107] V. Mariano, J. A. Tobon Vasquez, M. R. Casu, and F. Vipiana, “Efficient Data Generation for Stroke Classification via Multilayer Perceptron,” in *2022 IEEE International Symposium on Antennas and Propagation and USNC-URSI Radio Science Meeting (AP-S/URSI)*, Jul. 2022, pp. 890–891. doi: 10.1109/AP-S/USNC-URSI47032.2022.9886434.

[108] J. Li, G. Zhu, and M. Xi, “Automating Stroke Subtype Classification from Electromagnetic Signals Using Principal Component Methods,” 2021.

[109] X. Lin, Y. Chen, Z. Gong, and H. Zhang, “Brain Stroke Classification using a Microwave Transmission Line Approach,” in *2020 IEEE Asia-Pacific Microwave Conference (APMC)*, Dec. 2020, pp. 1092–1094. doi: 10.1109/APMC47863.2020.9331463.

[110] J. Xu *et al.*, “Noninvasive and portable stroke type discrimination and progress monitoring based on a multichannel microwave transmitting–receiving system,” *Sci Rep*, vol. 10, no. 1, Art. no. 1, Dec. 2020, doi: 10.1038/s41598-020-78647-x.

[111] G. Li *et al.*, “Early assessment of acute ischemic stroke in rabbits based on multi-parameter near-field coupling sensing,” *BioMedical Engineering OnLine*, vol. 21, no. 1, p. 20, Mar. 2022, doi: 10.1186/s12938-022-00991-y.

[112] L. Ying, L. Guanghong, G. Qingxin, Z. De, L. Mingqiang, and L. Xiaolin, “Wideband Microwave System for Brain Diagnosis,” in *2019 4th International Conference on Communication and Information Systems (ICCIS)*, Dec. 2019, pp. 104–107. doi: 10.1109/ICCIS49662.2019.00025.

[113] M. Salucci, J. Vrba, I. Merunka, and A. Massa, “Real-time brain stroke detection through a learning-by-examples technique—An experimental assessment,” *Microwave and Optical Technology Letters*, vol. 59, no. 11, pp. 2796–2799, 2017, doi: 10.1002/mop.30821.

[114] T. Pokorny and J. Tesarik, “Microwave Stroke Detection and Classification Using Different Methods from MATLAB’s Classification Learner Toolbox,” in *2019 European Microwave Conference in Central Europe (EuMCE)*, May 2019, pp. 500–503.

[115] “COMSOL Multiphysics®.” COMSOL AB, Stockholm, Sweden. [Online]. Available: www.comsol.com

[116] T. Pokorny *et al.*, “On the Role of Training Data for SVM-Based Microwave Brain Stroke Detection and Classification,” *Sensors*, vol. 23, no. 4, Art. no. 4, Jan. 2023, doi: 10.3390/s23042031.

[117] J. Redr *et al.*, “Microwave Hyperthermia of Brain Tumors: A 2D Assessment Parametric Numerical Study,” *Sensors*, vol. 22, no. 16, Art. no. 16, Jan. 2022, doi: 10.3390/s22166115.

[118] J. Tesarik, T. Pokorny, and J. Vrba, “Dielectric sensitivity of different antennas types for microwave-based head imaging: numerical study and experimental verification,” *International Journal of Microwave and Wireless Technologies*, pp. 1–14, undefined/ed, doi: 10.1017/S1759078720000835.

[119] R. L. H. Erik G. Lee, “Population Head Model Repository V1.0.” IT’IS Foundation, 2016. doi: 10.13099/VIP-PHM-V1.0.

[120] “Materialize 3-Matic.” Leuven, Belgium. [Online]. Available: www.materialise.com

[121] T. Said and V. V. Varadan, “Variation of Cole-Cole model parameters with the complex permittivity of biological tissues,” in *Microwave Symposium Digest, 2009. MTT ’09. IEEE MTT-S International*, Jun. 2009, pp. 1445–1448. doi: 10.1109/MWSYM.2009.5165979.

[122] “IEEE Recommended Practice for Determining the Peak Spatial-Average Specific Absorption Rate (SAR) in the Human Head from Wireless Communications Devices: Measurement Techniques,” *IEEE Std 1528-2013 (Revision of IEEE Std 1528-2003)*, pp. 1–246, Sep. 2013, doi: 10.1109/IEEESTD.2013.6589093.

[123] C.-S. Park and B.-S. Jeong, “Reconstruction of a high contrast and large object by using the hybrid algorithm combining a Levenberg-Marquardt algorithm and a genetic algorithm,” *IEEE Transactions on Magnetics*, vol. 35, no. 3, pp. 1582–1585, May 1999, doi: 10.1109/20.767278.

[124] G. Oliveri, P. Rocca, and A. Massa, “SVM for Electromagnetics: State-of-art, potentialities, and trends,” in *Proceedings of the 2012 IEEE International Symposium on Antennas and Propagation*, Jul. 2012, pp. 1–2. doi: 10.1109/APS.2012.6348759.

[125] J. Tesarik, T. Pokorny, and L. Holek, “Samples of Dry Head Tissues Phantoms for Brain Stroke Classification,” in *World Congress on Medical Physics and Biomedical Engineering 2018*, 2019, pp. 775–778.

[126] T. Pokorny, D. Vrba, J. Tesarik, D. B. Rodrigues, and J. Vrba, “Anatomically and Dielectrically Realistic 2.5D 5-Layer Reconfigurable Head Phantom for Testing Microwave Stroke Detection and Classification,” *International Journal of Antennas and Propagation*, 2019. https://www.hindawi.com/journals/ijap/2019/5459391/ (accessed Nov. 25, 2019).

[127] T. Pokorny and J. Tesarik, “3D Printed Multi-layer Molds of Human Head Tissue Phantoms for Microwave Stroke Detection,” in *2019 PhotonIcs Electromagnetics Research Symposium - Spring (PIERS-Spring)*, Jun. 2019, pp. 1424–1427. doi: 10.1109/PIERS-Spring46901.2019.9017648.

[128] “Legacy MATLAB and Simulink Support for Arduino.” https://uk.mathworks.com/matlabcentral/fileexchange/32374-legacy-matlab-and-simulink-support-for-arduino (accessed Aug. 23, 2021).

[129] T. Hastie, R. Tibshirani, and J. H. Friedman, *The Elements of Statistical Learning: Data Mining, Inference, and Prediction*. Springer Science & Business Media, 2001.

[130] J. Shlens, “A Tutorial on Principal Component Analysis.” arXiv, Apr. 03, 2014. doi: 10.48550/arXiv.1404.1100.

[131] V. Vapnik, *The Nature of Statistical Learning Theory*, 2nd ed. New York: Springer-Verlag, 2000. doi: 10.1007/978-1-4757-3264-1.

[132] N. Cristianini and J. Shawe-Taylor, *An Introduction to Support Vector Machines and Other Kernel-based Learning Methods by Nello Cristianini*. 2000. doi: 10.1017/CBO9780511801389.

[133] J. Snoek, H. Larochelle, and R. P. Adams, “Practical Bayesian Optimization of Machine Learning Algorithms,” *arXiv:1206.2944 [cs, stat]*, Aug. 2012, Accessed: Jan. 10, 2021. [Online]. Available: http://arxiv.org/abs/1206.2944

[134] J. Snoek *et al.*, “Scalable Bayesian Optimization Using Deep Neural Networks,” *arXiv:1502.05700 [stat]*, Jul. 2015, Accessed: Jan. 10, 2021. [Online]. Available: http://arxiv.org/abs/1502.05700

[135] J. R. Landis and G. G. Koch, “The Measurement of Observer Agreement for Categorical Data,” *Biometrics*, vol. 33, no. 1, pp. 159–174, 1977, doi: 10.2307/2529310.

[136] B. McDermott *et al.*, “Anatomically and dielectrically realistic microwave head phantom with circulation and reconfigurable lesions,” *Progress In Electromagnetics Research B*, vol. 78, pp. 47–60, Jan. 2017, doi: 10.2528/PIERB17071805.

[137] B. Mohammed *et al.*, “Stable and Lifelong Head Phantoms Using Polymer Composition Mimicking Materials to Test Electromagnetic Medical Imaging Systems,” *IEEE Journal of Electromagnetics, RF and Microwaves in Medicine and Biology*, vol. 5, no. 4, pp. 322–328, Dec. 2021, doi: 10.1109/JERM.2021.3051311.

[138] S. Abedi, N. Joachimowicz, N. Phillips, and H. Roussel, “A Simulation-Based Methodology of Developing 3D Printed Anthropomorphic Phantoms for Microwave Imaging Systems,” *Diagnostics*, vol. 11, no. 2, Art. no. 2, Feb. 2021, doi: 10.3390/diagnostics11020376.

[139] M. L. McHugh, “Interrater reliability: the kappa statistic,” *Biochem Med (Zagreb)*, vol. 22, no. 3, pp. 276–282, Oct. 2012.

Appendix A

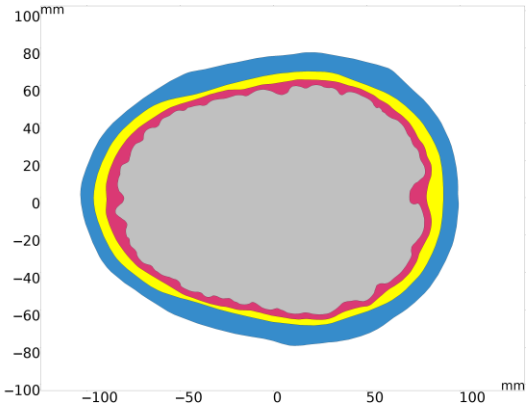

Phantom 1

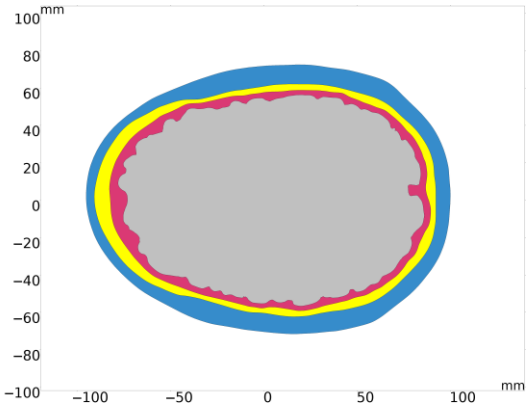

Phantom 2

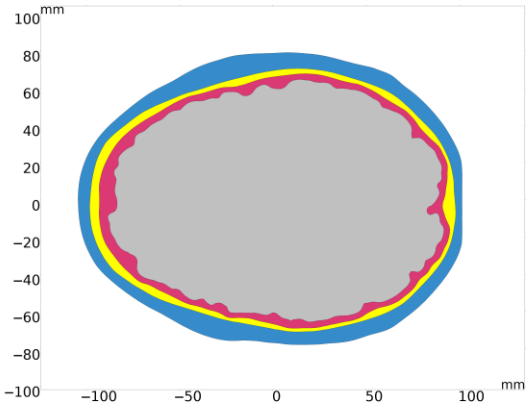

Phantom 3

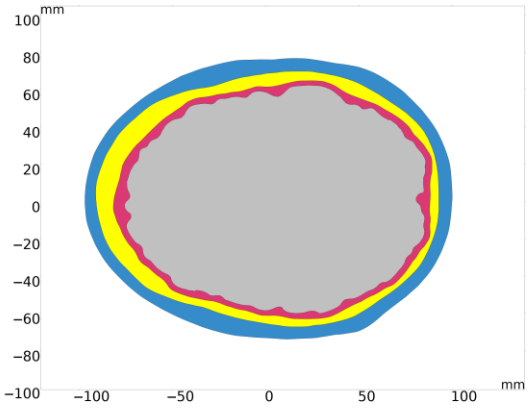

Phantom 4

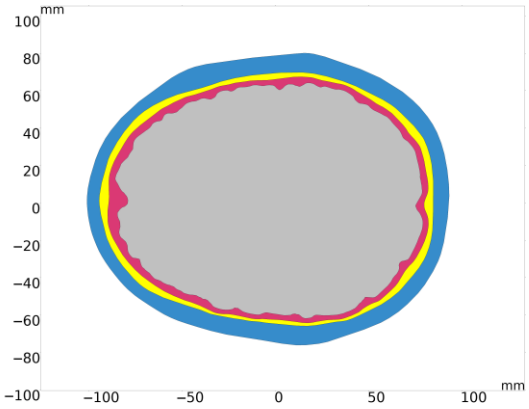

Phantom 5

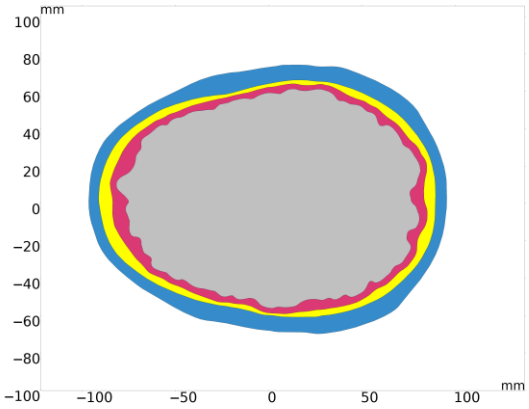

Phantom 6

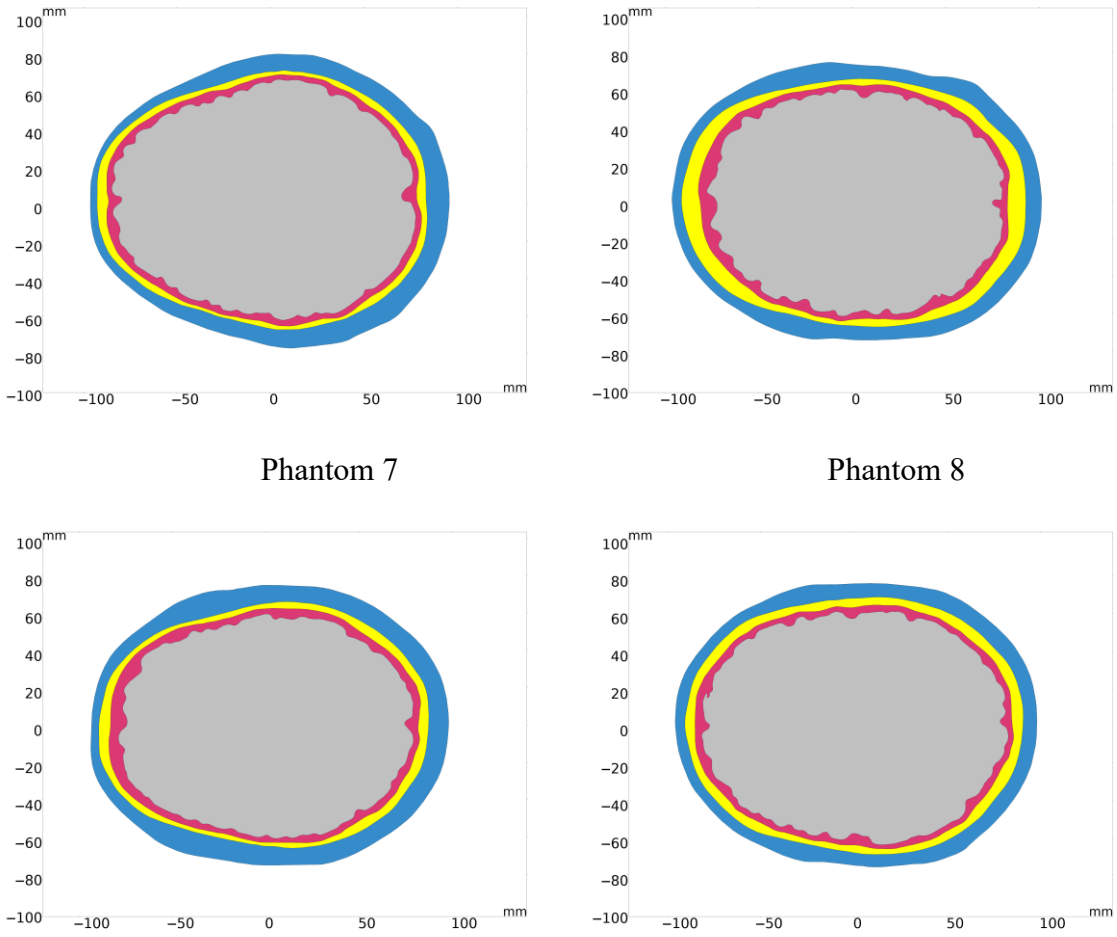

Figure 43. Ten different 2D models of human heads based on real subjects, created by cutting through the brain part of the head. Models include layers of the scalp, skull, cerebrospinal fluid (CSF), and brain.

Appendix B

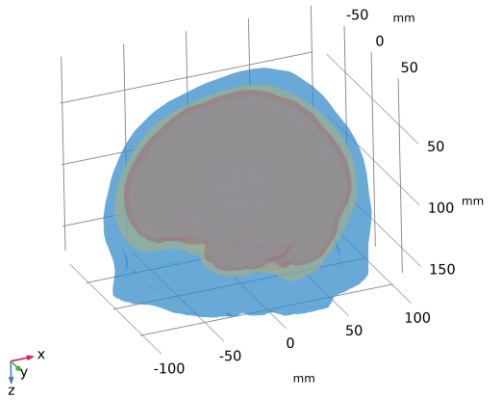

Phantom 1

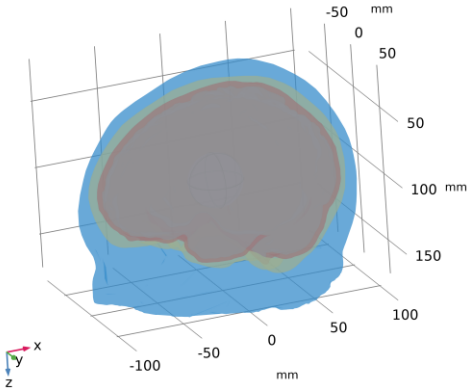

Phantom 2

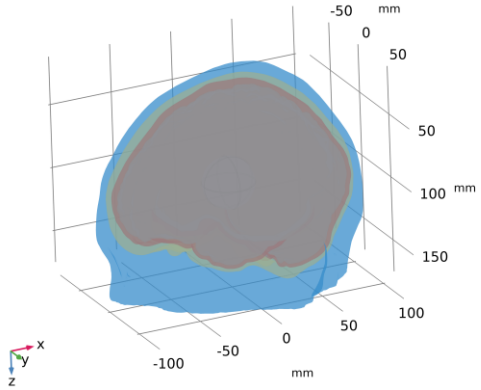

Phantom 3

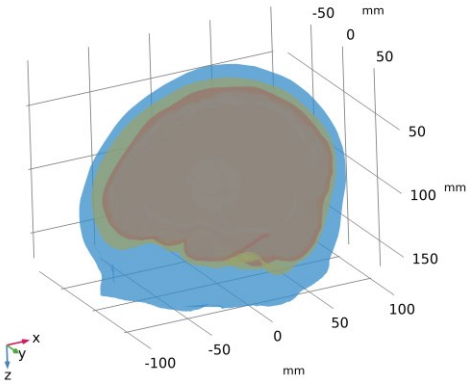

Phantom 4

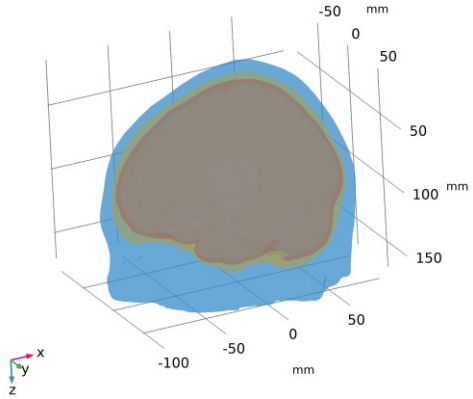

Phantom 5

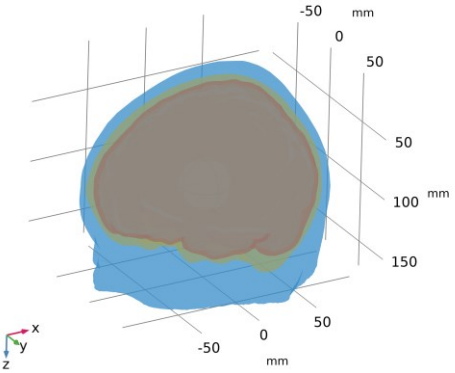

Phantom 6

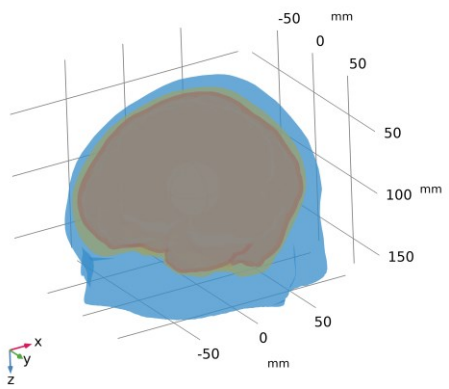

Phantom 7

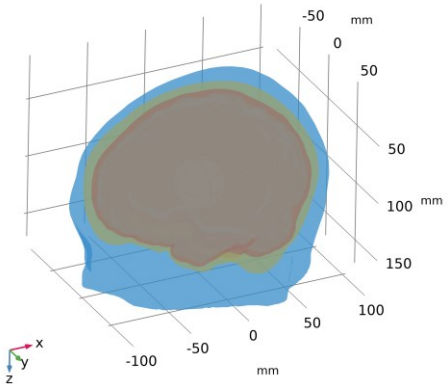

Phantom 8

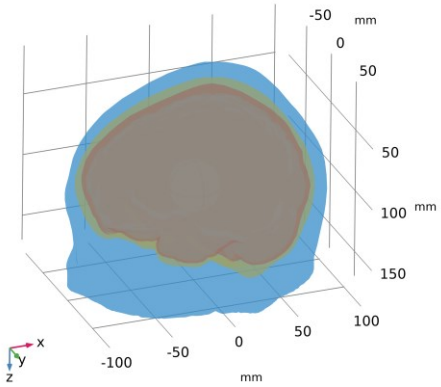

Phantom 9

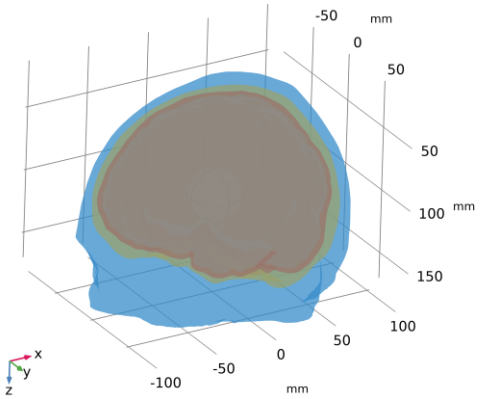

Phantom 10

Figure 44. Ten different 3D models of human heads based on real subjects. Models include layers of the scalp, skull, cerebrospinal fluid (CSF), and brain.

Appendix C

This appendix presents the S-parameter changes induced by the virtual presence of ischemic and hemorrhagic strokes calculated using 2D and 3D numerical models and experimental measurements. These changes were calculated by subtracting the S-parameters for the case when the inner part of the antenna system was filled only with the matching medium ($\varepsilon_r = 40$, $\sigma = 1$ S/m) from the S-parameters for the case where the stroke model was added virtually.

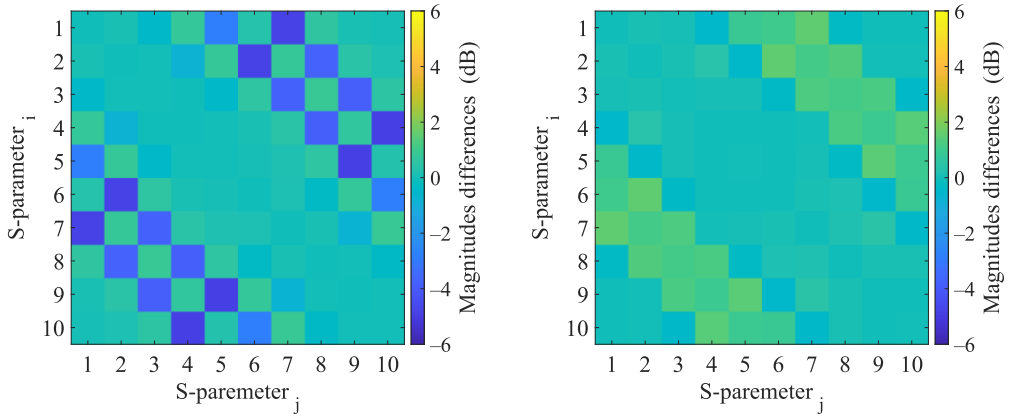

(a) (b)

Figure 45. 2D numerical simulations. Magnitudes difference of 2D numerical model induced by the virtual presence of a 40 mm radius (a) hemorrhagic and (b) ischemic stroke located at position (0, 0).

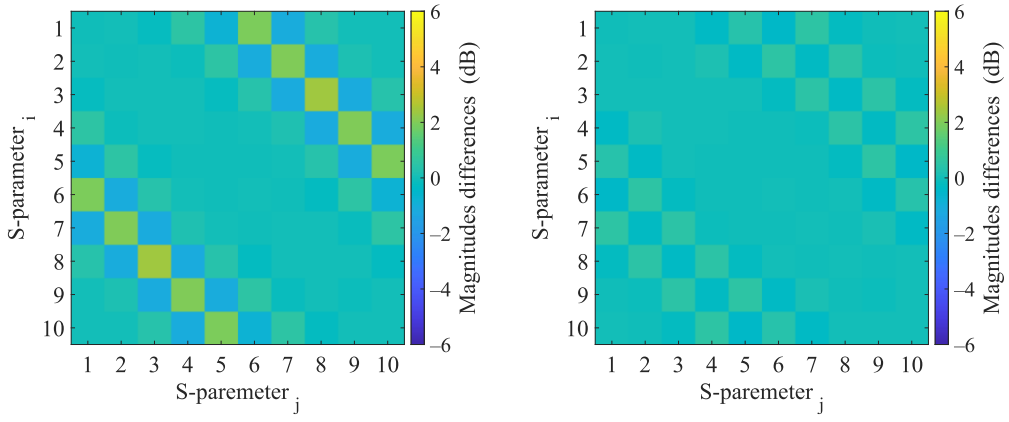

(a) (b)

Figure 46. 3D numerical simulations. Magnitudes difference of 3D numerical model induced by the virtual presence of a 40 mm radius (a) hemorrhagic and (b) ischemic stroke located at position (0, 0).

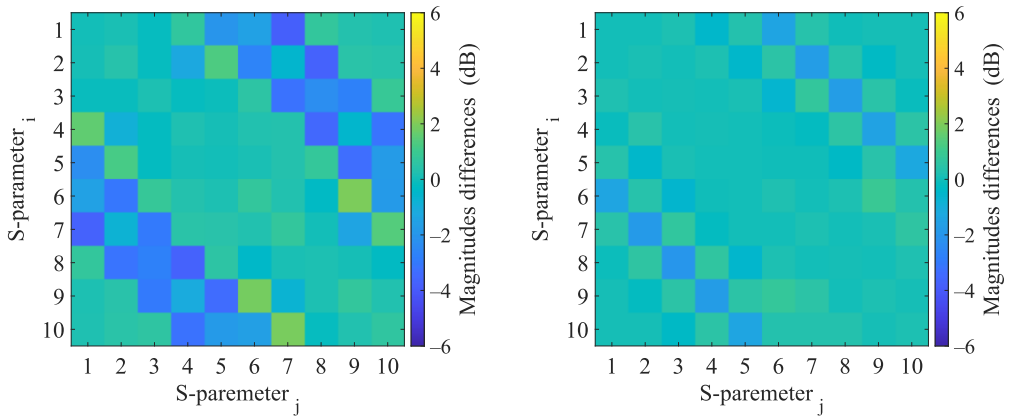

(a) (b)

Figure 47. Experimental measurements with liquid phantom. Magnitudes difference of experimental microwave system induced by the presence of a 40 mm radius (a) hemorrhagic and (b) ischemic stroke phantom located at position (0, 0).

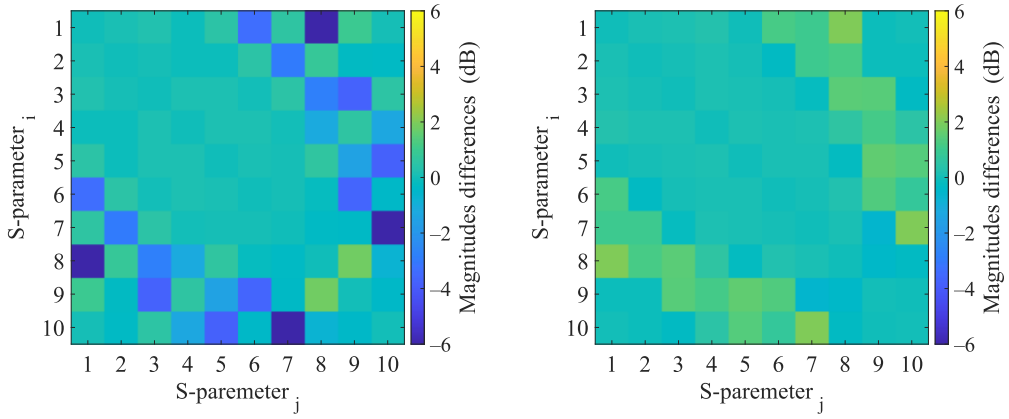

(a) (b)

Figure 48. 2D numerical simulations. Magnitudes difference of 2D numerical model induced by the virtual presence of a 40 mm radius (a) hemorrhagic and (b) ischemic stroke located at position (−20, 30).

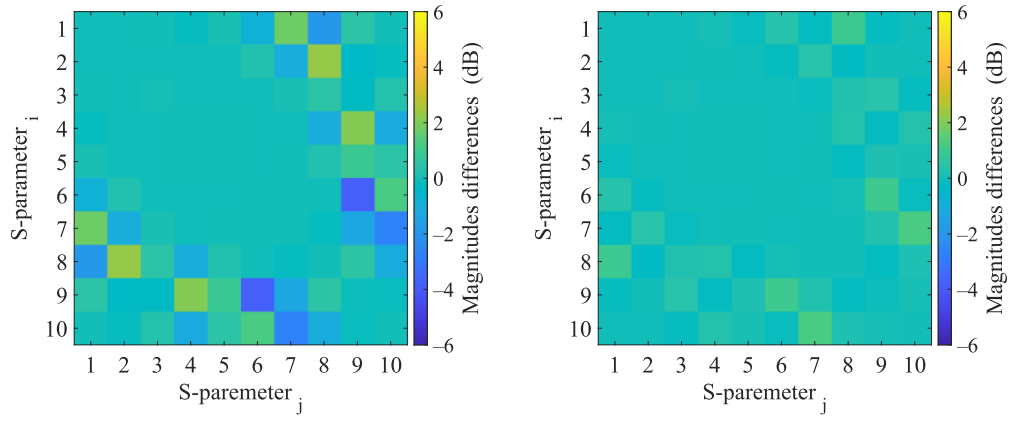

(a) (b)

Figure 49. 3D numerical simulations. Calculated differences in S-parameters induced by the virtual presence of a 40 mm radius (a) hemorrhagic and (b) ischemic stroke located at position (−20, 30).

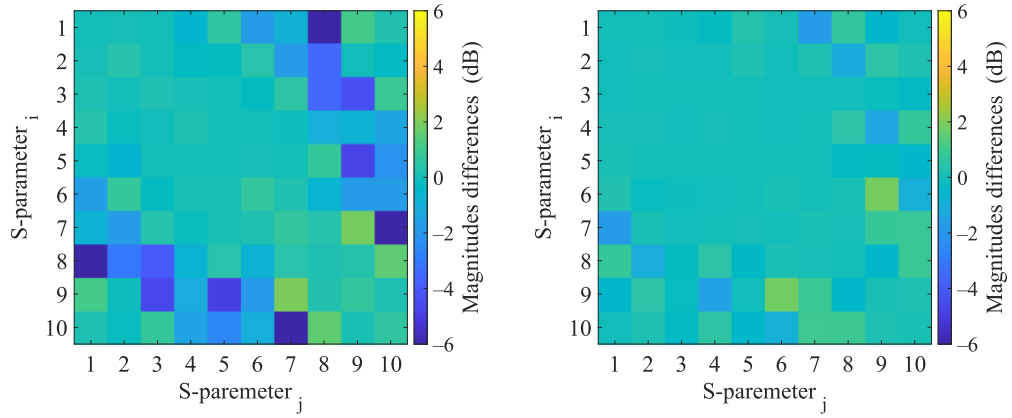

(a) (b)

Figure 50. Experimental measurements with liquid phantom. Magnitudes difference of experimental microwave system induced by the presence of a 40 mm radius (a) hemorrhagic and (b) ischemic stroke phantom located at position (−20, 30).

Appendix D

Graphs of classification accuracy and cross-validation error for different dimensionality reductions for different numbers of frequency points.

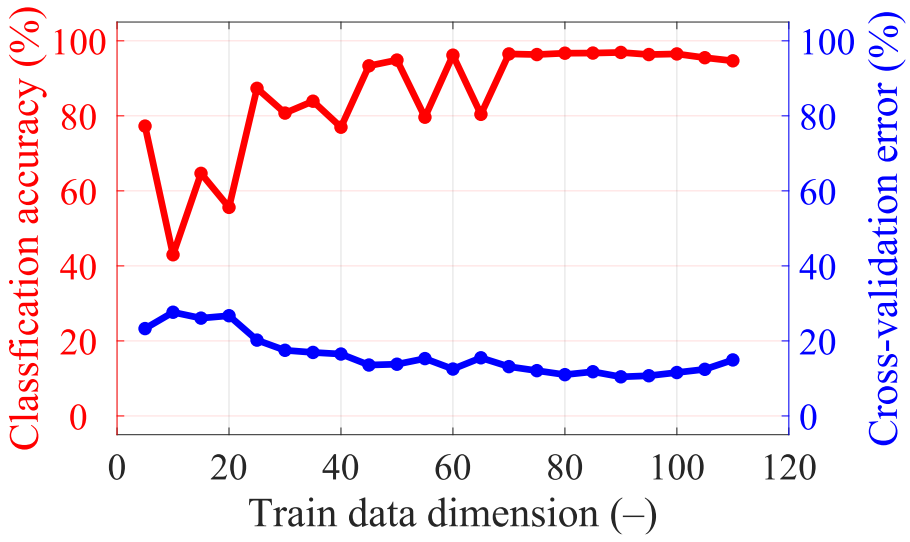

Figure 51. Classification accuracy and cross-validation error for different dimensionality reductions in data for a single frequency point (1 GHz).

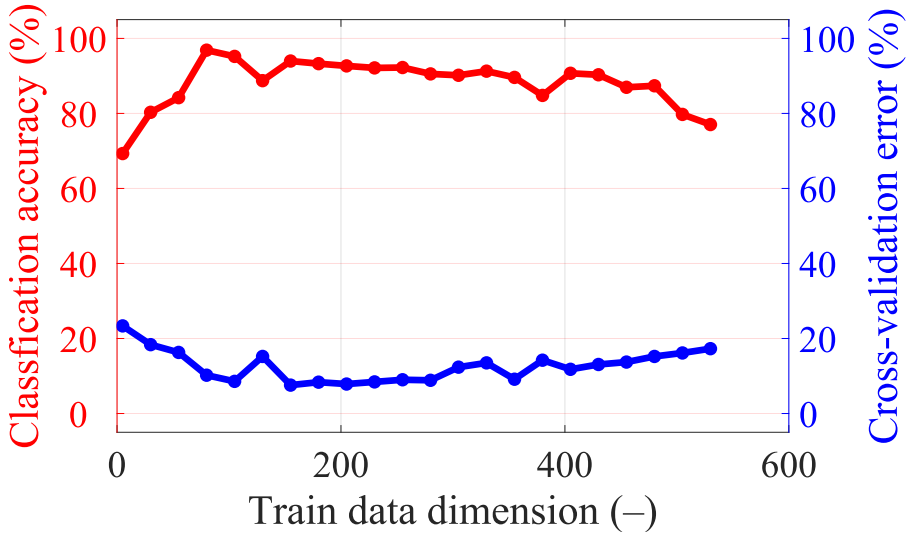

Figure 52. Classification accuracy and cross-validation error for different dimensionality reductions in the data for five frequency points (from 0.8 GHz, step 0.1 GHz, to 1.2 GHz).

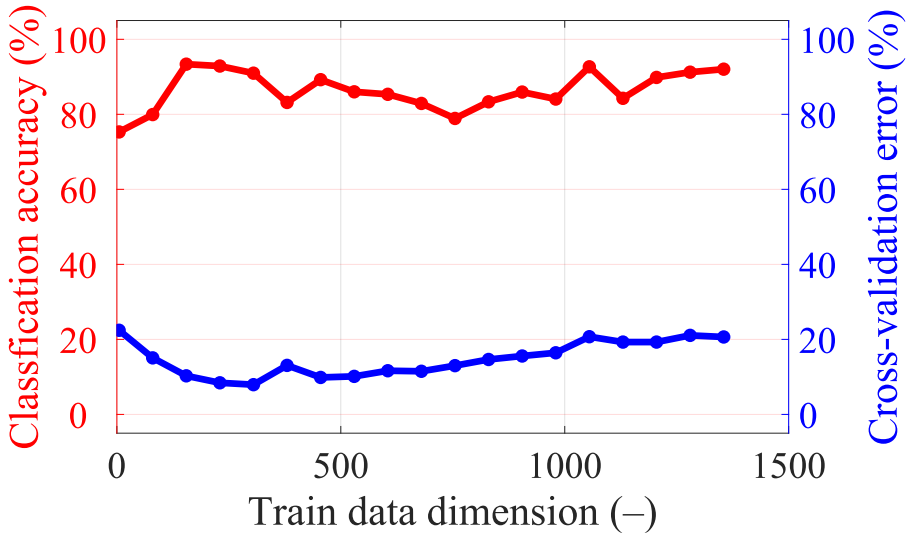

Figure 53. Classification accuracy and cross-validation error for different dimensionality reductions in data for 15 frequency points (from 0.8 GHz, step 0.05 GHz, to 1.5 GHz).

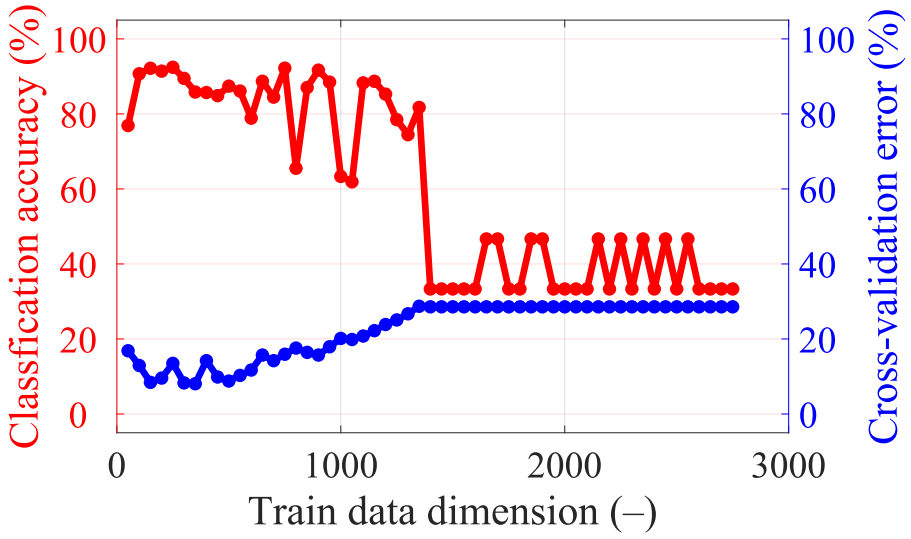

Figure 54. Classification accuracy and cross-validation error for different dimensionality reductions in the data for 25 frequency points (from 0.8 GHz, step 0.05 GHz, to 2 GHz).

Appendix E

Table 31. Description of the dataset structure to store simulation and measurement data

Parameter	Description	Units
No	Number of the simulation or measurement scenario	(-)
StrokeType	Stroke phantom type number: hemorrhagic (1), ischemic (-1), no stroke (0)	(-)
StrokeSizeD	Diameter of stroke	(mm)
StrokePositionXYZ	X,Y, and Z coordinates of the location of a stroke in head	(mm)
PhantomType	Number of head phantom used: 310, 311…319	(-)
ScalePhantomXYZ	Phantom scaling in XYZ axes- Scalp, Scull, CSF and Brain was scaled.	(-)
Freq	Simulation / measurement frerquency	(Hz)
S_mat_ReIm	S-matrix in real and imaginary format	(-)
Modul	S-matrix in module format	(dB)
Phase	S-matrix in phase format	(°)
LineReIm	The real (Re) and imaginary (Im) values were formatted into one line - format to be utilized in the LBE algorithms. Only the independent elements of the S-matrix were employed. The S-matrix is sorted in the following order: 1 : 11 is Re $S_{1,1}$, Re $S_{2,2}$ …..Re $S_{10,10}$ 11 : 20 is Im $S_{1,1}$, Im $S_{2,2}$ … Im $S_{10,10}$ 21 : 65 is Re $S_{2,1}$, Re $S_{3,1}$, Re $S_{3,2}$, Re $S_{4,1}$ … Re $S_{4,3}$, Re $S_{5,1}$ … Re $S_{5,4}$, Re $S_{6,1}$ …… Re $S_{10,9}$; 66 : 110 is Im $S_{2,1}$, Im $S_{3,1}$, Im $S_{3,2}$, Im $S_{4,1}$ … Im $S_{4,3}$, Im $S_{5,1}$ … Im $S_{5,4}$, Im $S_{6,1}$ …… Im $S_{10,9}$;	(-)
LineModulPhase	The module (Mo) and phase (Ph) values were formatted into one line - format to be utilized in the LBE algorithms. Only the independent elements of the S-matrix were employed. The S-matrix is sorted in the following order: 1 : 11 is Mo $S_{1,1}$, Mo $S_{2,2}$ …..Mo $S_{10,10}$; 11 : 20 is Ph $S_{1,1}$, Ph $S_{2,2}$ … Ph $S_{10,10}$ 21 : 65 is Mo $S_{2,1}$, Mo $S_{3,1}$, Mo $S_{3,2}$, Mo $S_{4,1}$ … Mo $S_{4,3}$, Mo $S_{5,1}$ … Mo $S_{5,4}$, Mo $S_{6,1}$ …… Mo $S_{10,9}$; 66 : 110 is Ph $S_{2,1}$, Ph $S_{3,1}$, Ph $S_{3,2}$, Ph $S_{4,1}$ … Ph $S_{4,3}$, Ph $S_{5,1}$ … Ph $S_{5,4}$, Ph $S_{6,1}$ …… Ph $S_{10,9}$;	(-)°